FRACTURE AND ADHESION IN SOFT MATERIALS SUBJECTED TO LARGE DEFORMATION

A Dissertation

Presented to the Faculty of the Graduate School

of Cornell University

In Partial Fulfillment of the Requirements for the Degree of

Doctor of Philosophy

by

Rong Long

January 2011

FRACTURE AND ADHESION IN SOFT MATERIALS SUBJECTED TO LARGE DEFORMATION

Rong Long, Ph. D.

Cornell University 2011

This dissertation studies large deformation elasticity with an aim to understand fracture and adhesion in soft polymeric materials. First, motivated by recent experiments using thin elastic membranes to measure interfacial adhesion, we propose a theory to describe the adhesive contact between an inflated hyperelastic membrane and a rigid substrate based on large deformation elasticity. A key result is the exact expression for the energy release rate in terms of local variables at the contact edge, which links adhesion to the contact angle. In addition, our theory allows two types of friction conditions between the membrane and the substrate: frictionless and no-slip contact. Numerical simulations for a neo-Hookean membrane are carried out to study the relation between applied pressure and contact area.

The second part of this dissertation focuses on solving the asymptotic stress and deformation fields near the tip of a Mode I traction free plane stress crack in incompressible hyperelastic solids. We develop a method using hodograph transform to obtain the dominant singularity of the near tip deformation field. This method is particularly useful for severely strain hardening materials and is used to find out the crack tip stress and deformation fields for two types of soft materials: generalized neo-Hookean solids and an exponentially hardening solid. Our asymptotic solutions are verified using finite element simulations. The limitations of a previous result for the generalized neo-Hookean solids are resolved by our solution.

Finally, we study the large deformation of an isolated penny-shaped crack in an infinite block of incompressible hyperelastic solid. The crack is subjected to remote tensile true stresses that are parallel (S) and normal (T) to the undeformed crack faces. We use finite element method to determine the energy release rates for different triaxiality ratios S/T. Our results shows that the energy release rate increases rapidly with S/T at finite strains, while for small deformations, it is independent of S/T. For the special case of pure hydrostatic tension ($S/T=1$), the energy release rate approaches infinity for the neo-Hookean solid at a *finite* tension. We also show that strain hardening significantly reduces the energy release rate for the same remote loading.

BIOGRAPHICAL SKETCH

Rong Long was born in Xiajiang County of Jiangxi Province, P. R. China, on January 10, 1986. After completing high school in his hometown, he entered University of Science and Technology of China in August 2002 and graduated with a B.S. degree in Theoretical and Applied Mechanics in June 2006. He then enrolled in the graduate field of Theoretical and Applied Mechanics at Cornell University in August 2006, and defended his Ph.D. dissertation on September 28, 2010. He married Yeyun Zhou on October 4, 2009.

To my parents and my wife for their support and love

ACKNOWLEDGMENTS

First of all, I would like to express my sincerest thanks to my advisor, Professor Chung-Yuen Hui, for his support and guidance during my dissertation work. His enthusiasm, curiosity to discover, intelligence and great knowledge make him the best advisor that I could ever have. He taught me a lot of academic skills during my study, from writing research papers to thinking critically and independently. On top of that, he is also a mentor and a true friend to me. I enjoyed and will always remember the time spent with him talking about research, having tasty food he cooked and fishing in cold winter mornings.

I would also like to thank Professor S. Leigh Phoenix and Professor Michael Thompson for serving in my special committee. They made many helpful suggestions and recommended courses which turned out to be very useful in my research.

I am fortunate enough to have worked with many brilliant scientists. Among them are Professor Anand Jagota at Lehigh University, Professor Kenneth R. Shull at Northwestern University, Professor Costantino Creton at ESPCI Paris in France, and Professor Metin Sitti at Carnegie Mellon University. Most of my research topics are motivated by the interesting experiments carried out in their research groups. I am also indebted to them for their insightful suggestions that greatly improved the quality of this dissertation.

Thanks are also due to my fellow group members, Lulin Shen, Venkat Krishnan, Jingzhou Liu, Jing Ning, Nicole Nadermann and Congrui Jin. We have shared many pleasant and fruitful discussions, usually during the weekly group meetings. In particular, I am thankful to Dr. Venkat Krishnan who has used his expertise in finite element simulation to help me overcome many technical difficulties during my research.

I wish to take this opportunity to offer my deepest gratitude to my dear family. My parents, Wenjun Long and Yanxia He, have been constantly supportive along the way. My beloved wife, Yeyun Zhou, always has faith in me, which gives me great confidence and helped me go through many difficult times. Without her company, my life would not have been so joyful.

Finally, I would like to acknowledge several sources of financial supports during my four years at Cornell. I am grateful to the Department of Theoretical and Applied Mechanics at Cornell University for providing me a fellowship during my first year of study and a teaching assistantship for one year. The supports from Department of Energy and National Science Foundation are also acknowledged.

TABLE OF CONTENTS

LIST OF FIGURES

LIST OF ABBREVIATIONS

FEM . . . . . Finite Element Method

GK . . . . . Geubelle and Knauss

GNH . . . . . Generalized neo-Hookean

JKR . . . . . Johnson-Kendall-Roberts

LEFM . . . . . Linear Elastic Fracture Mechanics

ODE . . . . . Ordinary Differential Equation

PDE . . . . . Partial Differential Equation

VCEM . . . . . Virtual Crack Extension Method

WKB . . . . . Wentzel-Kramers-Brillouin

PREFACE

Three chapters in this dissertation (Chapter 2-4) were originally prepared as individual research papers. Editorial modifications were made in these chapters so that a consistent style is maintained throughout the thesis. However, same mathematical notations may have different meanings in different chapters. As a result, the readers should be aware that symbols referring to physical quantities only apply within each chapter.

CHAPTER 1

INTRODUCTION

Nucleation and growth of defects in soft polymeric materials have been extensively studied for a long time, due to the great technological importance of this subject in rubber and adhesion industry. For example, the durability of rubber products relies on the material's ability to resist crack growth. Another example is the pressure sensitive adhesives, whose adhesion strength depends on the cavity nucleation and evolution process in the adhesive layer made of soft polymers [1].

The interest in fracture of soft materials has been renewed by recent efforts to develop tough gels, which have many potential biomedical applications (e.g. artificial cartilage). Development of such tough gels was pioneered by Gong *et al.* [2]. They created a hydrogel with two independent polymer networks: a highly crosslinked primary network and a loosely crosslinked secondary network. This double network gel can achieve a fracture toughness up to $10^3 J/m^2$ [3], over a hundred times larger than ordinary single network gel. The extremely high fracture toughness of a double network gel is attributed to the large energy dissipation during the formation of multiple damage zones in the primary network upon loading [4]. These damage zones are held together by the secondary network so that the gel maintains its structural integrity at the macroscopic scale. This toughening mechanism has inspired many researchers to design improved gel systems that can overcome some of the limitations in the double network gel. For example, since the primary network is covalently cross-linked, the damage in the primary network is not recoverable. In other words, the double-network gel cannot recover from overloads and thus is not fatigue resistant. Henderson *et al.* [5] recently created gels that are both fracture and fatigue resistant by introducing additional ionic cross-links to a physically cross-linked polymer network.

To study the fracture behavior of soft elastomers and gels, the deformation and stresses in these materials during crack growth need to be quantitatively described. Classical fracture mechanics theory is based on the infinitesimal deformation assumption and has been successfully applied to traditional engineering materials such as metal, ceramics and polymer glass. Soft materials are different from these traditional engineering materials in that they can undergo large deformation for a given stress due to their low modulus (KPa-MPa). In contrast, the modulus of steel is about 200GPa, several orders of magnitude larger than elastomers or gels. Therefore, fracture of soft materials has to be studied in the framework of large deformation theory. This dissertation presents theoretical works on three problems relevant to the fracture and adhesion of soft materials.

The first problem (Chapter 2) is motivated by an experimental technique to measure adhesion using a thin membrane attached to the end of a tube [6]. When inflated under pressure, the membrane can make contact with a rigid substrate underneath it. By measuring the applied pressure during contact, it is possible to extract the adhesion energy between the membrane and the substrate. This method has much higher sensitivity to surface adhesion than the traditional JKR test [7] where bulk material is used, and therefore, is suitable for measurements of the strength of weak bonds. For example, the membrane contact technique can be used to measure ionic cross-linking strength between two diblock polymer brushes coated on the membrane and substrate. These measurements provide useful information for designing tough and fatigue resistant hydrogels [5]. Despite the advantages in measurement sensitivity, data analysis of the membrane contact test is difficult because of nonlinearities from material behavior, large deformation and adhesive contact conditions. These complications are all incorporated in a theory for adhesive membrane contact presented in this chapter.

The second problem (Chapter 3) focuses on the asymptotic stress and deformation

field around the tip of a plane stress crack in an elastomer sheet under symmetric tensile loads. The plane stress condition is a good approximation for most gel or elastomer fracture specimens consisting of thin sheets [8-10]. The asymptotic stress field can provide boundary conditions for the separation process near the crack tip. Unlike linear elastic theory, the crack tip field is sensitive to the constitutive material model. Also, the governing equations are highly nonlinear and are very difficult to solve analytically and even numerically. Guebelle and Knauss determined the crack tip stress and deformation fields for a plane stress crack in generalized neo-Hookean materials [11]. However, their solution breaks down for moderate to large n, where n is a measure of the degree of strain hardening of the material. In this chapter, we develop a method that applies to a wider class of material models. The limitations of the results by Guebelle and Knauss for generalized neo-Hookean materials are also resolved.

The last problem (Chapter 4) is on cavitation in soft elastomers or gels. When loaded in tension in a confined geometry, soft elastic materials are subjected to large hydrostatic tension and often fail by nucleation and growth of cavities. Current theory assumes that the cavity growth can be described by a reversible elastic deformation process [12,13]. A classical result often used to interpret the cavitation experiments is that a spherical void in an infinite neo-Hookean material media will expand without bound when the applied hydrostatic tensile stress exceeds $5E/6$ [14], where E is the Young's modulus of the neo-Hookean material in the small strain regime. However, another theory, supported by a recent experiment [15], suggests that cavity growth is an irreversible fracture process, accompanied by bond breaking and creation of new cavity surface. In this theory, cavity growth is determined by energetics, i.e., a cavity starts to grow when its energy release rate exceeds a critical value. In this chapter, we model a single cavity by a circular crack in an infinite block of incompressible hyperelastic solid. This crack is subjected to remote tensile true stresses that are parallel (S) and normal (T)

to the undeformed crack surfaces. The focus of our study is to determine how the triaxiality ratio *S/T* affects the energy release rate, which represents the driving force for crack growth. Linear elastic fracture mechanics predicts that the energy release rate is independent of *S/T*. However, our result shows a strong dependence of the energy release rate on *S/T* and thus demonstrates that linear elastic fracture mechanics theory is not capable of accurately describing the failure of soft materials.

REFERENCES

[1] Creton C., 2003, *MRS Bulletin*, **28**, 434-439.

[2] Gong J.P., Katsuyama Y., Kurokawa T., Osada Y., 2003, *Adv. Mater.*, **15**, 1155-1158.

[3] Tanaka Y., Kuwabara R., Na Y.H., Kurokawa T., Gong J.P., Osada Y., 2005, *J. Phys. Chem. B*, **109**, 11559-11562.

[4] Brown H.R., 2007, *Macromolecules*, **40**, 3815-3818.

[5] Henderson K.J., Zhou T.C., Otim K.J., Shull K.R., 2010, *Macromolecules*, 43, 6193-6201.

[6] Flory A.L., Brass D.A., Shull K.R., 2007, *J. Polym. Sci., Part B: Polym. Phys*, **45**, 3361-3374.

[7] Johnson K.L., Kendall K., Roberts A.D., 1971, *Proc. R. Soc. London Ser. A*, **324**, 301-313.

[8] Baumberger T., Caroli C., Martina D., 2006, *Nat. Mater.*, **5**, 552-555.

[9] Baumberger T., Caroli C., Martina D., 2006, *Euro. Phys. J. E*, **21**, 81-89.

[10] Seitz M.E., Martina D., Baumberger T., Krishnan V.R., Hui C.Y., Shull K.R., 2009, *Soft matter*, **5**, 447-45.

[11] Geubelle P.H., Knauss W.G., 1994, *J. Elasticity*, **35**, 61-98.

[12] Gent A.N., Lindley P.B., 1958, *Proc. R. Soc. London, Ser. A*, **249**, 195-205.

[13] Ball. J.M., 1982, *Phil. Trans. R. Soc. A*, 1982, **306**, 557-611.

[14] Green A.E., Zerna W., 1954, *Theoretical Elasticity* 1954, Clarendon Press, Oxford.

[15] Cristiano A., Marcellan A., Long R., Hui C.Y., Stolk J., Creton C., 2010, *J. Polym. Sci., Part B: Polym. Phys*, **48**, 1409-1422.

CHAPTER 2

LARGE DEFORMATION ADHESIVE CONTACT MECHANICS OF CIRCULAR MEMBRANES WITH A FLAT RIGID SUBSTRATE[1]

2.1 Introduction

A very successful technique to measure the adhesive interaction between a soft and a hard solid is the Johnson-Kendall-Roberts (JKR) test [1]. In this test, a soft hemisphere is brought into contact with a flat surface by the application of a compressive force. Since the contact area increases with adhesion for the same applied force, a measurement of the contact area versus force can be used to deduce the work of adhesion of the surfaces in contact. Maugis and Barquins [2] placed these results in fracture mechanics terms, and showed that the test could be used to extract the energy release rate, G, which for a given system generally depends on the velocity at which the perimeter of the contact area is either advancing or receding. The relationship between force and contact radius in these experiments is determined by a balance involving the elastic deformation energy of the material and the adhesion energy between the two surfaces. Systems with an increased mechanical compliance, and hence a decreased deformation energy, can provide an enhanced sensitivity to adhesive interactions. This fact has been one of the driving forces for the development of sensitive adhesion tests utilizing thin membranes [3-8].

A typical experimental geometry for a membrane adhesion experiment, taken from the work of Flory *et al.* [8], is illustrated schematically in Figure 2.1. First, a circular membrane is attached to a circular tube of radius R which is suspended at a fixed distance of δ_d above a flat stiff substrate. The tube is pressurized, producing a uniform excess pressure P on the membrane (e.g. P is the difference between the pressure in the

[1] Long R., Shull K.R., Hui C.Y., 2010, *J. Mech. Phys. Solids*, **58**, 1225-1242.

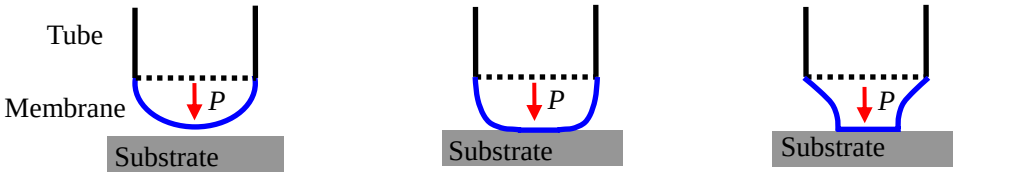

(a) Stage 1: Inflation
$0<P<P_c$

(b) Stage 2: Inflation & Contact
$P>P_c$

(c) Stage 3: Deflation
Reducing P.

Figure 2.1 A schematic showing 3 stages of the membrane contact experiments [8]. Stage 1: free inflation of the membrane when the uniformly applied pressure P is less than P_c; Stage 2: the membrane is in contact with the substrate once $P>P_c$; Stage 3: reducing the pressure P to peel the membrane off the substrate. Note that P can be negative in this stage.

tube and the air pressure outside). At a critical pressure P_c, the deformed membrane makes contact with the substrate. As the pressure increases past P_c, the contact area increases. The contact pressures can be quite low (tens or hundreds of Pascals in the experiments [8]), and are also uniform within the contact zone where the membrane has no curvature. Both of these features are advantageous when measuring adhesive interactions with very soft materials, including many samples of biological relevance (living tissue, cell sheets, *etc*.). When a target contact area is achieved, the pressure is reduced until the membrane is completely detached from the substrate. By measuring the contact area as a function of the pressure as well as the local contact angle, it is possible to deduce the adhesion energy.

To interpret experimental data accurately, it is necessary to model the mechanics of adhesive contact. This problem is difficult because of complications from three sources. First, due to large displacements and strains, we must distinguish the deformed membrane from its undeformed configuration, which brings in geometric nonlinearity. The second difficulty is due to nonlinear material behavior of the membrane. The third is the contact condition, which depends on the adhesion and friction between the two surfaces. Previous models for membrane contact mechanics avoided these difficulties by using linear membrane, linear plate or von-Karman plate theory [3-7, 9]. An approximate model that takes into account of large deformation was proposed by Flory *et al.* [8], but this model is limited in several respects. For example, the membrane was assumed to be in a state of a *uniform equi-biaxial tension*, even though this condition is only satisfied at the center of the contact zone. In addition, frictionless contact was assumed, even though the no slip boundary condition is likely a better description of the contact process. Feng and Yang studied the contact between a pressurized spherical balloon and a rigid substrate using large deformation membrane theory [10]. However, they did not consider adhesion and friction during contact. In this chapter, we use the

theory of finite strain hyperelastic membranes which allows us to bypass these difficulties. It should be noted that, membrane theory neglects bending deformation. As discussed in the last section of this chapter, this simplification is justified for the experimental situations that we are modeling.

The plan of this chapter is as follows. The governing equations for the deformation of a hyperelastic membrane under applied pressure are summarized in section 2.2. The determination of contact area requires additional boundary conditions which depend on adhesion and friction. An adhesion model based on an energy balance equation is shown in section 2.3. We also derive an exact expression of the energy release rate in this section. The formulation in section 2.3 allows us to derive the necessary boundary conditions for the contact problem. The boundary conditions and numerical methods to solve the contact problem are presented in section 2.4, where both frictionless and no-slip contact conditions are considered. Generalizations of our method to account for fluid pressure and surface tension are given in section 2.5. We apply our method to a neo-Hookean membrane and present the numerical results in section 2.6. Further discussions on the membrane model and energy release rate are given in section 2.7.

2.2 Governing Equations of Axisymmetric Hyperelastic Membrane

A cross section of the inflated axisymmetric membrane is shown in Figure 2.2. The undeformed membrane occupies the interior of a circle lying on the plane $z = 0$ with radius *R*. The membrane is clamped along the edges at $r = R$ and a uniform pressure *P* is applied on its upper surface. The vertical distance between the flat membrane and the substrate is δ_d. We use a cylindrical coordinate system (r, ϕ, z) to describe the deformed material points on the membrane (see Figure 2.2). Since the deformation is axisymmetric, we can restrict our attention to any cross-section of the membrane, e.g. $\phi = 0$. The independent variable in our formulation is ρ $(0 \le \rho \le R)$, the material

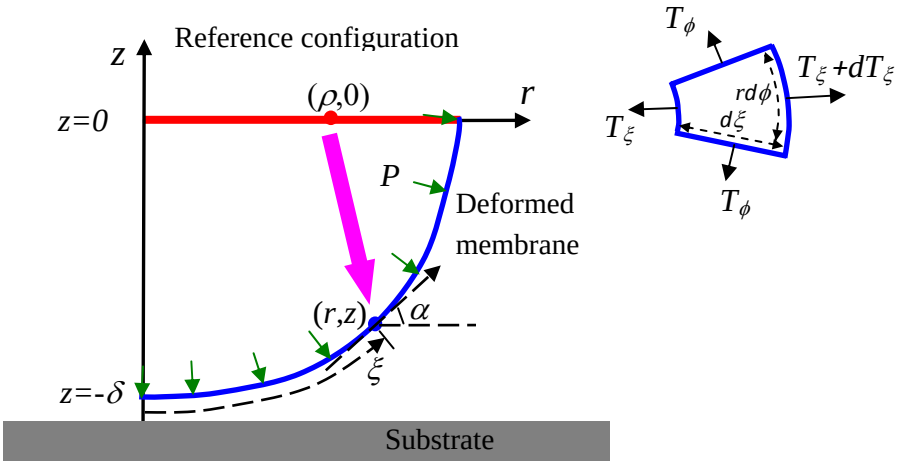

Figure 2.2 Geometry of a cross-section (e.g. $\phi = 0$) of the circular membrane before and after deformation. In this figure, the applied pressure P is not large enough to cause contact. ξ is the arc length of the cross-section curve of the deformed membrane ($\xi = 0$ at $r = 0$). The inset shows the line tensions T_ξ and T_ϕ acting on a deformed membrane element.

coordinate of a point on the membrane in the undeformed reference configuration. A material point originally located at $(r = \rho, z = 0)$ is displaced to the point $(r = r(\rho), z = z(\rho))$ shown in Figure 2.2. Let ξ denote the arc length of the cross-section curve of the deformed membrane (ξ is defined to be zero at $r = 0$, see Figure 2.2). α is the angle made by the tangent of the cross-section curve at (*r, z*) with the *r* axis. The two principal stretches are

$$\lambda_\xi = d\xi / d\rho, \tag{2.1}$$

$$\lambda_\phi = r / \rho . \tag{2.2}$$

Note that λ_ξ is the longitudinal stretch, i.e., along the cross-section curve in the *r*-*z* plane (see Figure 2.2), and λ_ϕ is the latitudinal stretch, i.e., along the direction normal to the *r*-*z* plane.

The equations governing the large deformation of free standing membrane under pressure *P* are [11]

$$\frac{d\lambda_\xi}{d\rho} = \frac{\lambda_\xi \left(T_\phi - T_\xi\right)\cos\alpha - \lambda_\phi \left(\partial T_\xi / \partial \lambda_\phi\right)\left(\lambda_\xi \cos\alpha - \lambda_\phi\right)}{\rho\lambda_\phi \left(\partial T_\xi / \partial \lambda_\xi\right)}, \tag{2.3}$$

$$\frac{d\alpha}{d\rho} = \frac{P\rho\lambda_\phi\lambda_\xi - \lambda_\xi T_\phi \sin\alpha}{\rho\lambda_\phi T_\xi}, \tag{2.4}$$

$$\frac{d\lambda_\phi}{d\rho} = \frac{\lambda_\xi \cos\alpha - \lambda_\phi}{\rho}, \tag{2.5}$$

$$\frac{dz}{d\rho} = \lambda_\xi \sin\alpha , \tag{2.6}$$

where (2.3), (2.4) are equilibrium equations and (2.5), (2.6) are geometric relations. T_ξ and T_ϕ are the longitudinal and latitudinal line tensions in the deformed configuration, respectively (see Figure 2.2 inset). The line tensions have units of force/length and are functions of the principal stretch ratios λ_ξ and λ_ϕ.

The specific relation between the line tensions and the stretch ratios depends on the

constitutive properties captured in the strain energy density function, *W*, of the material that makes up the membrane, which in general can be written as a function of λ_ξ and λ_ϕ. For example, *W* for an incompressible isotropic hyperelastic material depends on the two invariants

$$I_1 = \lambda_\xi^2 + \lambda_\phi^2 + 1/\left(\lambda_\xi \lambda_\phi\right)^2, \quad I_2 = \left(\lambda_\xi \lambda_\phi\right)^2 + 1/\lambda_\xi^2 + 1/\lambda_\phi^2 \tag{2.7}$$

The line tensions are related to *W* by [11, 12]

$$T_\xi = \frac{h_0}{\lambda_\phi}\frac{\partial W}{\partial \lambda_\xi} \tag{2.8}$$

$$T_\phi = \frac{h_0}{\lambda_\xi}\frac{\partial W}{\partial \lambda_\phi}, \tag{2.9}$$

where h_0 is the thickness of the undeformed membrane. An example of the strain energy density is the neo-Hookean model:

$$W = \frac{E}{6}\left(\lambda_\xi^2 + \lambda_\phi^2 + 1/\left(\lambda_\xi \lambda_\phi\right)^2 - 3\right). \tag{2.10}$$

Note that the material is assumed to be incompressible, so that the extension ratio in the thickness direction is equal to $1/\lambda_\xi\lambda_\phi$.

In the literature of nonlinear membranes [11], the line tensions in the reference configuration N_ξ, N_ϕ are often used instead of T_ξ, T_ϕ (line tensions in the deformed configuration). These different line tensions are related to one another by the appropriate extension ratios:

$$N_\xi = \lambda_\phi T_\xi, \tag{2.11}$$

$$N_\phi = \lambda_\xi T_\phi. \tag{2.12}$$

The respective line tensions N_ξ, N_ϕ and T_ξ, T_ϕ are analogous to the nominal (first Piola-Kirchhoff) stress and the true (Cauchy) stress in three dimensional continuum mechanics. We also note that (2.3)-(2.6) describe the deformation of the membrane

outside the contact zone. The contact zone in our case is the interior of a circle of *unknown* radius *a*. To determine *a*, we need to specify the boundary conditions at the contact edge. *A difficulty is that these boundary conditions depend on the manner in which the membrane is brought into contact with the substrate.* Specifically, these boundary conditions depend on the adhesion as well as friction between the membrane and the substrate. The adhesion model is introduced and discussed in detail in section 2.3. As for friction, we consider two limiting cases for simplicity, that is, frictionless contact and no-slip (full friction) contact. The boundary conditions for both frictionless and no-slip adhesive contact are derived in section 2.4.

2.3 Energy Release Rate

2.3.1 Modeling Adhesion

During inflation (Stage 2 in Figure 2.1), the contact area increases due to pressurization. The increase in contact area releases surface energy to the elastic membrane. Surface energy causes additional deformation of the elastic membrane and hence increases its elastic energy. At the end of the inflation phase, the applied pressure is reduced, causing the membrane to deflate (Stage 3 in Figure 2.1). In this phase, the contact line is often pinned (*i.e*. contact area stationary) at first, then starts to move once there is enough elastic energy available to free the contacting surfaces. Contact line pinning is due to the fact that the adhesion energy for breaking contact is usually much larger than that for making contact. The “contact line” means the boundary line of the contact region. On a cross-section graph, the contact line is also referred to as the contact edge (e.g. point *A* in Figure 2.3a).

A useful way of thinking about the process of making and breaking contact is to view the gap between the membrane and the substrate as an external crack. During inflation, the crack front recedes and adhesion energy is released to the system. During deflation,

the crack advances and elastic energy must be released by the system to create new surfaces. We define the energy release rate G as the energy released by the elastic system per unit contact area change. The energy release rate G provides a driving force for the motion of the contact line at a continuum level and does not address the complex bonding and debonding processes occurring near the contact line. The implicit assumption is that these processes take place in a cohesive region that is small compared with typical specimen dimensions. Therefore, the details of these processes have no effect on the continuum analysis. Using this assumption, the condition for making or breaking contact is

$$G = W_{ad}\,, \tag{2.13}$$

where W_{ad} is the *effective* work of adhesion of the interface. This condition will be used as a boundary condition to determine the size of the contact zone. It should be noted that W_{ad} need not to be a material constant. For example, adhesion hysteresis is observed in most experiments, *i.e.*, W_{ad} is much smaller for making contact than for breaking contact and is a function of contact line speed and history [2,13].

2.3.2 Derivation of Energy Release Rate

Expressions for the energy release rate for detaching an axisymmetric membrane from a rigid substrate were derived by Williams [14] and Wan & Liu [15], based on the assumption that the membrane is under uniform equi-biaxial stretch. Also, infinitesimal strain was assumed in their analysis. The energy release rate to detach a rigid punch from a circular flat membrane was evaluated numerically in Nadler & Tang [16]. Our goal in this section is to derive an exact expression for the energy release rate G. To the best of our knowledge, there is no analytical expression of the energy release rate for a fully nonlinear membrane.

2.3.2.1 Energy Release Rate: No-slip

To find the energy release rate, there is no loss in generality to consider the deflation phase. First, we assume a no-slip condition in the contact region. Let the current configuration of contact be specified by $\rho = \rho^*$, $r = a$; that is, the contact edge is located at ($r = a$, $z = -\delta_d$), which corresponds to the material point $\rho = \rho^*$ in the reference configuration. We denote the tangent angle of the free standing membrane at the contact edge, $\alpha(\rho = \rho^*)$, as the contact angle, θ. In general, θ is non-zero due to adhesion. Imagine a process where the applied pressure is fixed at P and the contact radius shrinks by da; the energy release rate is given by the negative change in potential energy of the elastic system per unit change in contact area.

A schematic of the shrinking of the contact line is shown in Figure 2.3a. During this process, a small portion of membrane is detached. Specifically, the material point ρ^* which occupies $r = a$ (A in Figure 2.3a) has now moved to A'. The detached membrane segment da corresponds to the line segment $(\rho^* - d\rho, \rho^*)$ in the reference configuration.

We call the membrane outside the original contact region, i.e., $\rho \in (\rho^*, R)$, part 1 and material points associated with the newly detached membrane part 2 (i.e. $\rho \in (\rho^* - d\rho, \rho^*)$, see Figure 2.3b). Before detachment, part 2 has an area of $2\pi a da$. After detachment, part 1 and part 2 move to new positions (see dashed lines in Figure 2.3b). The change in potential energy of the elastic system (membrane + loading device) $\Delta\Gamma$ due to the detachment of part 2 is

$$\Delta\Gamma = \Delta U - \Delta W_P, \tag{2.14}$$

where ΔU is the change in the elastic energy of the system and ΔW_P is the work done by the applied pressure on the system during the detachment of part 2. Since there

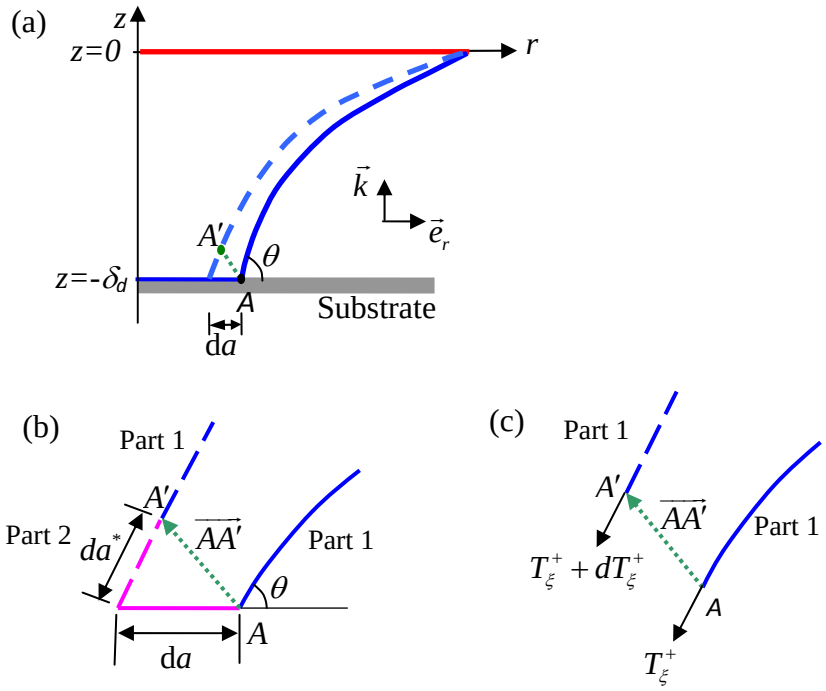

Figure 2.3 (a) Local change in geometry during an infinitesimal shrinkage in contact line da. The initial position of a material point on contact line is at A. The final position of the same material point after shrinkage is at A'. Full lines indicate the initial shape of the membrane both inside and outside the contact region. Dashed lines indicate the shape of the membrane outside the contact region after shrinkage. (b) Close-up of the contact edge before and after motion of the contact line. (c) Line tension acting on part 1 before and after motion of the contact line.

is no slip in the contact region, the elastic energy of the membrane that remains in contact is unchanged. Therefore,

$$\Delta U = \Delta U_1 + \Delta U_2, \tag{2.15}$$

where ΔU_1 and ΔU_2 denote the first order changes in elastic energy for part 1 and part 2 respectively. The total work of applied pressure ΔW_P can also be decomposed into ΔW_{P1} and ΔW_{P2}, which are the work done by the applied pressure on part 1 and part 2, respectively, i.e.,

$$\Delta W_P = \Delta W_{P1} + \Delta W_{P2}. \tag{2.16}$$

Equations (2.14)-(2.16) imply that

$$\Delta\Gamma = \left(\Delta U_1 - \Delta W_{P1}\right) + \left(\Delta U_2 - \Delta W_{P2}\right). \tag{2.17}$$

While it is difficult to calculate ΔU_1 and ΔW_{P1} individually, $\left(\Delta U_1 - \Delta W_{P1}\right)$ can be computed by examining the energy balance of part 1. The change in elastic energy of part 1, ΔU_1, equals the total work done on part 1, which is ΔW_{P1} plus the work done by the line tension $\vec{T}_\xi^+$ to carry A to A'(see Figure 2.3c). Note that we have not assumed that $\vec{T}_\xi$ is continuous across the contact edge. The superscript "+" in $\vec{T}_\xi^+$ denotes the line tension as ρ approaches the contact edge from $\rho > \rho^*$. Therefore,

$$\Delta U_1 - \Delta W_{P1} = 2\pi a \vec{T}_\xi^+ \bullet \overrightarrow{AA'}. \tag{2.18}$$

The right hand side of (2.18) is the work done by the line tension $\vec{T}_\xi^+$ acting on part 1 during the contact line shrinking. Using the unit vectors $\vec{e}_r$ and $\vec{k}$ shown in Figure 2.3a, we obtain

$$\vec{T}_\xi^+ = -T_\xi^+\left(\vec{e}_r \cos\theta + \vec{k}\sin\theta\right), \tag{2.19}$$

where θ is the contact angle and T_ξ^+ is the magnitude of the line tension, $\vec{T}_\xi^+$. A straightforward computation shows that

$$\overrightarrow{AA'} = -(da)\vec{e}_r + (da^*)\left(\vec{e}_r \cos\theta + \vec{k}\sin\theta\right), \tag{2.20}$$

where da^* is the arc length of the cross-section curve of membrane part 2 after being detached from the substrate (see Figure 2.3b). Combining (2.18)-(2.20), we obtain

$$\Delta U_1 - \Delta W_{P1} = 2\pi a T_\xi^+ \cos\theta da - 2\pi a T_\xi^+ da^*. \tag{2.21}$$

In general, the arc length da^* in (2.21) is not equal to da. This is because the stretch ratio λ_ξ at the contact edge is discontinuous. For example, the stretch ratio λ_ξ inside the contact region cannot change due to no-slip contact. However, the stretch ratio λ_ξ outside the contact region (free standing membrane) can be changed by changing the applied pressure *P*. In contrast, λ_ϕ must be continuous at the contact edge since $r(\rho)$ is continuous everywhere (see(2.2)). Let λ_ξ^- and λ_ξ^+ denote the stretch ratio as one approaches the contact edge from $\rho < \rho^*$ and $\rho > \rho^*$ respectively. Since $da = d\xi$, where $d\xi$ is the cross-section arc length of part 2 before detachment, (2.1) implies that

$$da = \lambda_\xi^- d\rho, \tag{2.22}$$

where $d\rho$ is the line segment corresponding to membrane part 2 in the reference configuration. After being detached, part 2 is outside the contact region and the arc length of part 2 changes to da^*, which, to first order, is

$$da^* = \lambda_\xi^+ d\rho. \tag{2.23}$$

Combining (2.21)-(2.23) we obtain:

$$\Delta U_1 - \Delta W_{P1} = -2\pi a T_\xi^+ da\left(\frac{\lambda_\xi^+}{\lambda_\xi^-} - \cos\theta\right). \tag{2.24}$$

Next, we compute $\Delta U_2 - \Delta W_{P2}$ in (2.17). The work done by the pressure on part 2, ΔW_{P2}, is on the order of $P \times 2\pi a da\left|\overrightarrow{AA'}\right| \sim (da)^2$ and therefore can be neglected. However, due to the *discontinuity of the stretch ratio* λ_ξ *at the contact edge*, the first

order term of ΔU_2 is not zero and is given by

$$\Delta U_2 = 2\pi\rho^* h_0 d\rho\left(W(\lambda_\xi^+, \lambda_\phi) - W(\lambda_\xi^-, \lambda_\phi)\right), \tag{2.25}$$

where $W(\lambda_\xi, \lambda_\phi)$ is the energy density and λ_ϕ is the latitudinal stretch ratio at the contact line. Note that we have used the continuity of λ_ϕ at the contact line in the derivation of (2.25). Combining (2.17), (2.24) and (2.25), we have:

$$\Delta\Gamma = -2\pi a T_\xi^+ da\left(\frac{\lambda_\xi^+}{\lambda_\xi^-} - \cos\theta\right) + 2\pi\rho^* h_0 d\rho\left(W(\lambda_\xi^+, \lambda_\phi) - W(\lambda_\xi^-, \lambda_\phi)\right), \tag{2.26}$$

and the energy release rate is found to be

$$G = -\lim_{da\to 0}\frac{\Delta\Gamma}{2\pi a da} = T_\xi^+\left(\frac{\lambda_\xi^+}{\lambda_\xi^-} - \cos\theta\right) - \frac{\rho^* h_0}{a\lambda_\xi^-}\left(W(\lambda_\xi^+, \lambda_\phi) - W(\lambda_\xi^-, \lambda_\phi)\right). \tag{2.27}$$

This expression can be cast in a more useful form by recognizing that $a/\rho^* = \lambda_\phi$ from (2.2), using (2.8) to express T_ξ^+ in terms of *W*, and defining the following quantities:

$$\Delta W \equiv W(\lambda_\xi^+, \lambda_\phi) - W(\lambda_\xi^-, \lambda_\phi), \quad \Delta\lambda_\xi \equiv \lambda_\xi^+ - \lambda_\xi^-. \tag{2.28}$$

In this way we obtain the following expression for the energy releaser rate:

$$G = T_\xi^+\left(1 - \cos\theta\right) + \frac{h_o}{\lambda_\xi^-\lambda_\phi}\left[\left.\frac{\partial W}{\partial\lambda_\xi}\right|_{\xi=\xi^+}\Delta\lambda_\xi - \Delta W\right]. \tag{2.29}$$

All quantities in (2.29) are evaluated at the contact line, i.e., at $\rho = \rho^*$.

2.3.2.2 Energy Release Rate: Frictionless

For frictionless contact, the membrane in the contact region (i.e. $\rho \in [0, \rho^* - d\rho]$) is under uniform equi-biaxial tension of $\lambda_\phi = \lambda_\xi^-$ and can slide on the substrate during the detachment of part 2. The displacement of the contact edge in the deformed configuration, *da* (see Figure 2.3a), consists of two components: $(da)_d$ and $(da)_s$. $(da)_d$ is due to detachment of part 2, i.e.,

$$(da)_d = \lambda_\xi^- d\rho. \tag{2.30}$$

$(da)_s$ is due to the shrinkage of the membrane that remains in contact, that is,

$$(da)_s = -(\rho^* - d\rho)d\lambda_\phi = -(\rho^* - d\rho)d\lambda_\xi^- \approx -\rho^* d\lambda_\xi^-, \tag{2.31}$$

where $d\lambda_\xi^- = d\lambda_\phi$ is the increment of the equi-biaxial stretch ratio of the membrane in the contact region during the detachment of part 2. To first order,

$$da = (da)_d + (da)_s = \lambda_\xi^- d\rho + (-\rho^* d\lambda_\xi^-). \tag{2.32}$$

Since adhesion only resists the contact edge motion due to detachment $(da)_d$, we define the energy release rate as

$$G = -\lim_{da_d \to 0} \frac{\Delta\Gamma}{2\pi a (da)_d}, \tag{2.33}$$

where $\Delta\Gamma$ is the first order change in potential energy of the elastic system due to detachment of part 2. $\Delta\Gamma$ can be computed using the procedure shown in section 2.3.2.1. Details are given in Appendix 2.1. We find that $\Delta\Gamma$ is given by (2.26) with da replaced by $(da)_d$. Therefore, for frictionless contact, the energy release rate is still given by (2.29), which can be further simplified by noting that $\lambda_\xi^- = \lambda_\phi$, since the stretch state in the contact zone is equi-biaxial.

2.3.2.3 Remarks

We conclude the derivation of energy release rate in this section with several remarks.

1) For a given strain energy function, the energy release rate G is completely determined by the contact angle and local stretch ratios and longitudinal line tension at the contact edge (see (2.29)).
2) In general, the longitudinal line tension and stretch ratio T_ξ and λ_ξ are discontinuous across the contact edge.
3) The energy release rate expression (2.29) is valid for both no-slip and frictionless

conditions. However, values of λ_ξ within the contact zone depend on the nature of the frictional boundary condition, and will affect the energy release rate.

4) For the special case of a material with a strain energy function given by (2.10) the energy release rate is

$$G = T_\xi^+ \left(1-\cos\theta\right) + \frac{Eh_0}{6}\left[\frac{\left(\lambda_\xi^+ - \lambda_\xi^-\right)^2}{\lambda_A} + \frac{1}{\lambda_A^3}\left(1-3\left(\frac{\lambda_\xi^-}{\lambda_\xi^+}\right)^2 + 2\left(\frac{\lambda_\xi^-}{\lambda_\xi^+}\right)^3\right)\right], \quad (2.34)$$

where we have defined λ_A as the area extension ratio of the membrane in the contact region, i.e., $\lambda_A \equiv \lambda_\phi \lambda_\xi^-$. Additional comments regarding (2.34) and its connection to forms that have been used in the linearly elastic regime are made in section 2.7.

2.4 Membrane Contact Problem

As mentioned in the section 2.1, there are three stages during the membrane contact experiment (see Figure 2.1). In Stage 1, the maximum membrane displacement (δ in Figure 2.2) is not large enough to bring the membrane into contact with the substrate. The membrane is under free inflation. In Stage 2, the membrane makes contact with the substrate and the contact area increases as the applied pressure increases. Once a certain contact area is achieved, Stage 3 starts, where the applied pressure is reduced, causing the membrane to deflate. Eventually, the membrane is detached from the substrate. The adhesion energy associated with the Stage 2 (inflation) is invariably smaller than the Stage 3 (deflation), a situation that is analogous to contact hysteresis observed with wetting liquids.

In this section we discuss the boundary conditions for solving (2.3)-(2.6), as well as the numerical methods to simulate the contact problem in all stages. Because we require the solution of four coupled first order differential equations, at least four boundary conditions need to be specified. If additional parameters are unknown (e.g. the pressure

required to achieve a specified membrane deformation or contact area), then additional boundary conditions are also needed. The relevant boundary conditions for each of the different experimental stages are given in the following subsections.

2.4.1 Stage 1: Free Inflation

For values of δ that are not sufficient to bring the membrane into contact with the substrate, the membrane is under free inflation [12, 17-18]. The solution of freely inflated membrane can be obtained by numerically integrating (2.3)-(2.6) using an ordinary differential equation (ODE) solver, subject to the following boundary conditions:

$$\begin{aligned}
&\text{a) } z(\rho = R) = 0 \\
&\text{b) } \lambda_\phi(\rho = R) = 1 \\
&\text{c) } \alpha(\rho = 0) = 0 \\
&\text{d) } z\left(\rho = 0\right) = -\delta \\
&\text{e) } \lambda_\phi(\rho = 0) = \lambda_\xi\left(\rho = 0\right).
\end{aligned} \tag{2.35}$$

The two boundary conditions involving z and λ_ϕ at $\rho = R$ pertain to the attachment of the outer portion of the membrane, and are valid for all of the stages. Three additional boundary conditions are required because the pressure required to displace the center of the membrane by an amount of δ is unknown. For the free inflation stage, these additional boundary conditions are all applied at $\rho = 0$.

Membrane shapes obeying a neo-Hookean constitutive law (see (2.10)) are shown in Figure 2.4a. The membranes have a nearly uniform radius of curvature for all degrees of inflation, consistent with one of the assumptions of the simplified treatment given by Flory *et al.* [8]. The average area strain, $\varepsilon_{A,avg}$, of the membranes is given by the following expression:

$$\varepsilon_{A,avg} \equiv \frac{A_m}{\pi R^2} - 1 = \left(\frac{\delta}{R}\right)^2, \tag{2.36}$$

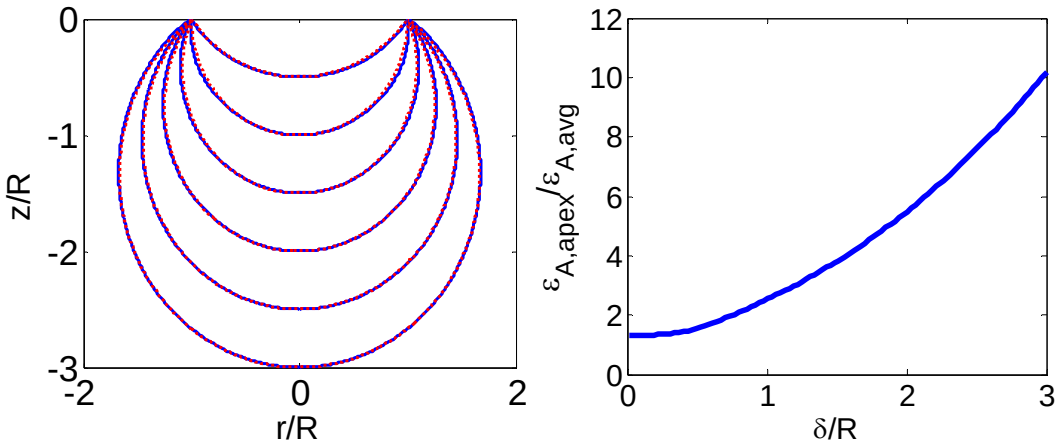

(a) (b)

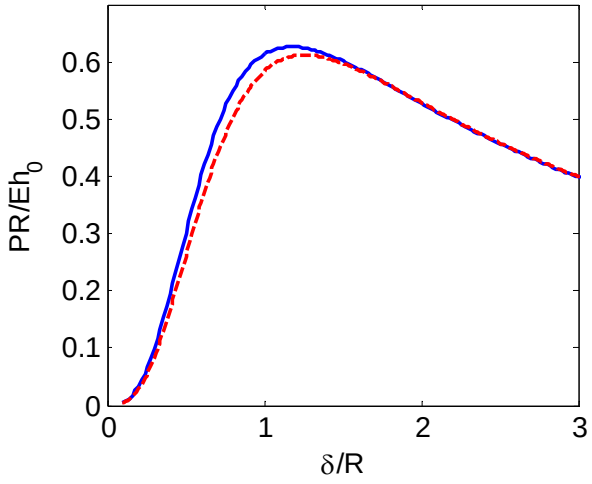

(c)

Figure 2.4 (a) Shapes of inflated membranes in the non-contact region for different values of δ and P; the solid line is obtained using our numerical solution and the dotted line is a section of a sphere; (b) Area strain at the apex, normalized by the average value given by (2.36); (c) Relationship between pressure and membrane deformation for a neo-Hookean membrane using the exact large deformation membrane theory (solid line) and the approximate form given by (2.40).

where A_m is the area of the deformed membrane. Equation (2.36) is exact for all values of δ provided that the deformed membrane can be viewed as a section of a sphere with a constant radius of curvature. For the neo-Hookean model, we find that the maximum error in (2.36) occurs for $\delta/R \sim 1$ and is only 8%.

In order to understand why many of the approximations from the previous treatment of Flory *et al.* work so well for a neo-Hookean model, we consider the relationship between membrane deformation and membrane tension for this particular strain energy function. For equi-biaxial stretch, observed at the apex of the inflated membrane where $\lambda_\xi = \lambda_\phi$, (2.8)-(2.10) can be combined to give the following expression for the membrane tension:

$$T_\xi = T_\phi = \frac{Eh_0}{3}\left(1 - 1/\lambda_\xi^6\right). \tag{2.37}$$

As the membrane stretch ratio increases, the membrane tension approaches a constant value of $Eh_0/3$, independent of the stretch. For this reason the membrane tension is roughly constant throughout the membrane, even when the stretch ratio of the membrane is heterogeneous, as is indeed the case for highly deformed membranes.

A useful measure of the strain heterogeneity in the deformed membranes is obtained by comparing $\varepsilon_{A,apex}$, the area strain (ratio of deformed to undeformed area subtracted by one) at the apex of the deformed membrane to the average membrane area strain given by (2.36). This comparison is shown in Figure 2.4b. At low deformations the strain is relatively uniform, with the area strain at the apex exceeding the average strain by a factor of 1.3. This discrepancy increases at larger deformations, with the strain at the apex greatly exceeding the average strain for large values of δ/R. The radius of curvature of the membrane remains nearly uniform, however, because of the asymptotic behavior of the membrane tension for highly deformed neo-Hookean materials (see (2.37)).

The pressure difference across the membrane is directly related to the tension, T_0, and the radius of curvature, R_0, both evaluated at the apex of the membrane ($\rho = 0$):

$$P = \frac{2T_0}{R_0}. \tag{2.38}$$

While (2.38) is valid in general, two approximations are made in the treatment of Flory *et al.* [8]. The first of these is that the two principal radii of curvature for the membrane are equal to R_0 everywhere, in which case R_0 is related to the membrane displacement, δ, by the following expression:

$$\frac{R_0}{R} = \frac{1}{2}\left(\frac{\delta}{R} + \frac{R}{\delta}\right). \tag{2.39}$$

For neo-Hookean membranes (2.39) is quite accurate, as the profiles shown in Figure 2.4a illustrate. The second approximation made in the treatment of Flory *et al.* is that T_0 is accurately described by (2.37), with $\lambda_\xi \lambda_\phi = \lambda_\xi^2$ equal to the average membrane area stretch ratio, *i.e.*, $1+(\delta/R)^2$ (see (2.36)). These assumptions lead to the following expression for the pressure:

$$\frac{PR}{Eh_0} = \frac{4\delta/R}{3\left(1+(\delta/R)^2\right)}\left(1 - \frac{1}{\left(1+(\delta/R)^2\right)^3}\right). \tag{2.40}$$

Even though (2.36) does not always provide an accurate approximation for the strain at the apex of the membrane, an accurate value for T_0 is still obtained from this approach because of the relative insensitivity of the tension to λ_ξ for large extensions (see (2.37)). This result is illustrated in Figure 2.4c, where the exact pressure/deformation relationship for a neo-Hookean material is compared to the prediction of (2.40).

Note that P does not monotonically increase with δ in Figure 2.4c; instead, it reaches a maximum and then decreases. There is no stable equilibrium solution for pressures exceeding this maximum. However, for other material models it has been found that the pressure continues to increase monotonically with separation δ (see [18]

for details). Similar instabilities were also found in a neo-Hookean solid with different geometries. For example, a spherical void in an infinite neo-Hookean solid subjected to internal pressure will grow without bound once the pressure reaches $5E/6$ [19-20]. In cases where different strain energy functions need to be used in order to adequately describe the elastic behavior of the membrane, approximations at the level of those used to generate (2.40) will no longer be sufficient, and the exact numerical approach described in this section will be necessary.

2.4.2 Stage 2: Adhesionless Contact

In this section, we consider Stage 2, where the contact area increases as the membrane is inflated past the point of initial contact. In experiments the adhesion associated with this phase is typically very small. Therefore, a good approximation is to assume that there is no adhesion between the membrane and substrate when the contact area is increasing, *i.e.* the energy release rate, *G*, is equal to zero. A vertical force balance at the contact line implies that the contact angle θ must be 0 if there is no adhesion (see Figure 2.7). Otherwise, the vertical component of $\vec{T}_{\xi}^{+}$ cannot be balanced. As a result boundary conditions (2.35c) and (2.35d) are simply shifted from $\rho = 0$ to $\rho = \rho^{*}$. Here ρ^{*} is the reference coordinate of the material point which now occupies the contact edge, *i.e.*, $\rho^{*} = a/\lambda_{\phi}$. The final boundary condition, corresponding to the value of λ_{ξ} at $\rho = \rho^{*}$, is different for frictionless and no-slip interfaces, as described below.

2.4.2.1 Frictionless Interface

The frictionless boundary condition implies that the part of the membrane that is in contact with the substrate is under uniform bi-axial stretch, that is, $\lambda_{\phi} = \lambda_{\xi}$. We contend that this condition is also satisfied at the contact edge $r = a$. The reasoning is as follows: λ_{ϕ} is continuous at the contact edge because of the continuity of $r(\rho)$ (see (2.2)).

Due to the frictionless condition and zero contact angle, a local force balance implies that the longitudinal line tension T_ξ must be continuous at the contact edge as well. Equation (2.8) and the continuity of T_ξ and λ_ϕ at $r = a$ imply that λ_ξ is also continuous at the contact edge. Therefore, $\lambda_\phi = \lambda_\xi$ at $r = a$. As a result, we obtain the following set of boundary conditions for adhesionless contact in the absence of friction:

$$\begin{aligned} &\text{a)}\ z(\rho = R) = 0 \\ &\text{b)}\ \lambda_\phi(\rho = R) = 1 \\ &\text{c)}\ \alpha(\rho = \rho^*) = 0 \\ &\text{d)}\ z\left(\rho = \rho^*\right) = -\delta_d \\ &\text{e)}\ \lambda_\phi(\rho = \rho^*) = \lambda_\xi\left(\rho = \rho^*\right). \end{aligned} \tag{2.41}$$

These boundary conditions and the geometry of the deformed shape are shown in Figure 2.5. The equations can be solved either by specifying ρ^* (related to the contact radius by $\rho^* = a / \lambda_\phi$) with an undetermined pressure, or by specifying the pressure with an undetermined value of ρ^*.

2.4.2.1 No-slip Interface

For no slip contact, $\lambda_\phi \neq \lambda_\xi$ at the contact line and (2.41e) is lost. In this case, the contact area depends on the history of contact and has to be determined incrementally using the following procedure. The starting point is when the apex of the deformed membrane just touches the substrate ($i = 0$). Let us seek the solution at the $(i+1)^{th}$ step assuming the solution at the i^{th} step has been determined. Denote the pressure at the i^{th} step by P_i, $i = 0,1,\ldots..$, with $P_{i=0} = P_c$. Also, denote the contact radius and its material coordinate at the i^{th} step by a_i and ρ_i^* respectively. We increase ρ_i^* by $\Delta\rho^*$, i.e., $\rho_{i+1}^* = \rho_i^* + \Delta\rho^*$. This will cause the contact radius to increase by Δa_i. Since λ_ξ is continuous at the contact line and the contact angle $\theta = 0$, (2.1) implies that Δa_i is

$$\Delta a_i \approx \left(\lambda_\xi\right)_i \Delta\rho^*, \tag{2.42}$$

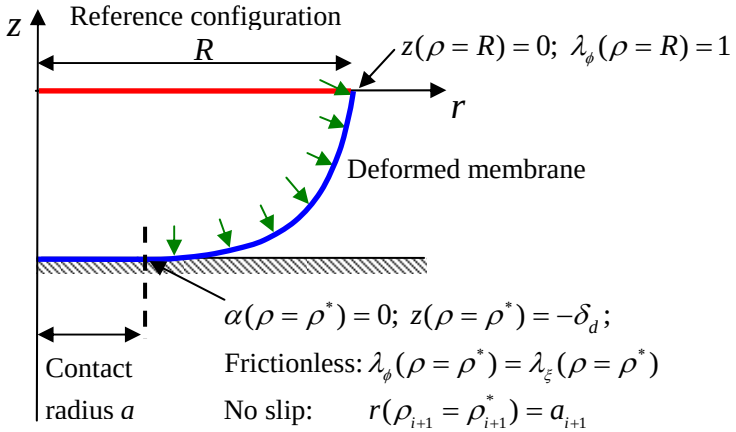

Figure 2.5 Boundary conditions of the membrane during Stage 2 (inflation).

where $\left(\lambda_\xi\right)_i$ is the stretch ratio evaluated at the contact line at the i^{th} step. Equation (2.42) allows us to update the contact radius to

$$r_{i+1}(\rho_{i+1}^*) = a_{i+1} = a_i + \Delta a_i \,. \tag{2.43}$$

Equation (2.43), together with the four boundary conditions in (2.41a-d), allows the ODE solver to march forward to solve the deformed profile and the pressure at the $(i+1)$ step. This process is repeated until the target contact radius is reached.

2.4.3 Stage 3: Adhesive Contact

In Stage 3, the pressure is reduced to detach the membrane. During deflation, the effective work of adhesion is not zero. According to (2.29), the contact angle in this stage is greater than zero. A schematic of this stage together with the boundary conditions is shown in Figure 2.6.

2.4.3.1 Frictionless Interface

The clamped boundary conditions at $\rho = R$ are still given by (2.41a,b). At the contact edge, we have

$$\begin{aligned} &\text{a)} \quad \alpha(\rho^*) = \theta \\ &\text{b)} \quad z(\rho^*) = -\delta_d \end{aligned} \tag{2.44}$$

where θ is the contact angle. At the beginning of deflation, the material coordinate ρ^* of the contact line is given by the solution of Stage 2 (see section 2.4.2.1). As the membrane is detached during deflation, the contact line coordinate ρ^* and the contact angle θ are unknown for a given pressure *P*. Two additional equations are needed to determine ρ^* and θ. One of them is obtained by applying a force balance to a membrane element near the contact line (see Figure 2.7). Due to adhesion, the contact angle is no longer zero. As a result, the line tension T_ξ is discontinuous at the contact edge.

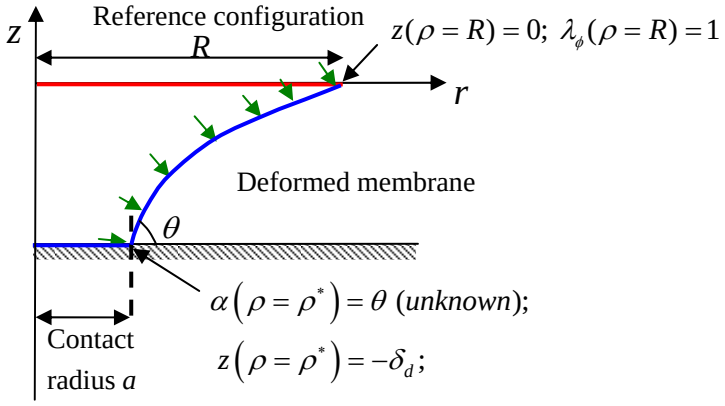

Figure 2.6 Boundary conditions associated with membrane during Stage 3 (deflation).

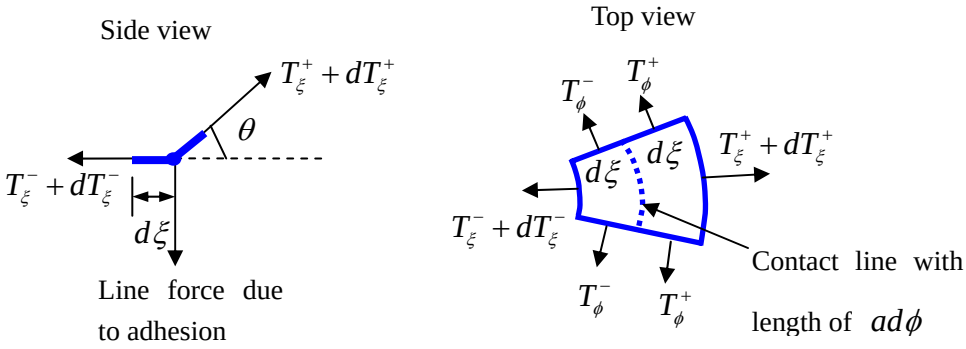

Figure 2.7 Free body diagram of the line forces acting on a membrane element in the neighborhood of the contact line.

Let T_ξ^+, T_ξ^- denote the line tension T_ξ as one approaches the contact edge from the outside and the inside respectively. As the dimension of the membrane element approaches 0, i.e., $d\xi, d\phi \to 0$, force balance implies that

$$T_\xi^+ \cos\theta = T_\xi^- . \tag{2.45}$$

The discontinuity of T_ξ and the continuity of the hoop stretch λ_ϕ at the contact line imply that λ_ξ must be discontinuous at the contact line.

The second condition can be obtained using (2.13) and (2.29), and the fact that $\lambda_\phi = \lambda_\xi^-$ inside the contact zone, *i.e.*,

$$G = T_\xi^+ \left(1-\cos\theta\right) + \frac{h_o}{\lambda_\xi^- \lambda_\phi}\left[\left.\frac{\partial W}{\partial \lambda_\xi}\right|_{\xi=\xi^+} \Delta\lambda_\xi - \Delta W\right] = W_{ad}\,; \quad \rho = \rho^* . \tag{2.46}$$

It should be noted that, because the adhesion energy in Stage 2 is zero, membrane detachment will not occur until the applied pressure decreases to some critical value. When no detachment occurs, i.e., when the pressure is above the critical value, ρ^* is given by the solution of Stage 2 and (2.46) is not satisfied, i.e.,

$$G = T_\xi^+ \left(1-\cos\theta\right) + \frac{1}{\lambda_\xi^-}\frac{h_o}{\lambda_\phi}\left[\left.\frac{\partial W}{\partial \lambda_\xi}\right|_{\xi=\xi^+} \Delta\lambda_\xi - \Delta W\right] < W_{ad}\,, \quad \rho = \rho^* . \tag{2.47}$$

If (2.47) is the case, the deformed shape as well as the pressure *P* is obtained by solving (2.3)-(2.6) by prescribing the contact angle θ and enforcing the boundary conditions (2.41a,b), (2.44a,b) and (2.45). At some contact angle θ, (2.46) will be satisfied, and then the deformed shape and the applied pressure *P* for some prescribed ρ^* can be obtained by using boundary conditions (2.41a,b,d), (2.45) and (2.46).

2.4.3.2 No-slip Interface

This case is straightforward since the initial values of ρ^* and *a* have been determined from the solution of Stage 2. The deformed profile and the contact angle θ

can be obtained by solving (2.3)-(2.6) subjected to the boundary conditions (2.41a,b,d) in addition to the following:

$$r(\rho^*) = a\,. \tag{2.48}$$

This procedure works as long as G, as given by (2.29), is less than W_{ad}, which is the condition for the pinning of the contact line. Note that λ_{ξ}^{-} is known from Stage 2 (see section 2.4.2.2). At some critical applied pressure, say P_D, the energy balance equation (2.13) is satisfied. The contact line will recede once the pressure drops below P_D. When this happens, equations (2.3)-(2.6) are solved iteratively using the same procedure described in section 2.4.2.2. The boundary conditions for this case are (2.41a,b,d), (2.48) and (2.13).

2.5 Generalizations: Fluid pressure and Surface Tension

Many experiments are conducted in water because of the importance of adhesive interactions in liquid environments. Also, very thin elastomeric membranes are permeable to air, and do not easily sustain a substantial pressure. This practical difficulty is minimized when the membrane is immersed in water. Our formulation above can be readily extended to accommodate this feature. If the test is conducted in a liquid of density ρ_w, the pressure P in (2.4) should be replaced by the following pressure, P_e, that is a function of z:

$$P_e = P - \rho_w g z\,, \tag{2.49}$$

where g is the gravitational acceleration and P is the pressure difference across the membrane at the $z=0$ plane defined in Figure 2.2.

Membranes used in experiments can have very small elastic modulus (as low as 14KPa in Flory *et al.* [8]). In this case, effect of surface energy cannot be neglected. The surface energy provides an isotropic contribution T_s to the membrane tension

independent of the strain state of the membrane, i.e.,

$$T_\xi = T_s + \frac{h_0}{\lambda_\phi}\frac{\partial W}{\partial \lambda_\xi}, \qquad T_\phi = T_s + \frac{h_0}{\lambda_\xi}\frac{\partial W}{\partial \lambda_\phi}, \tag{2.50}$$

where W is the elastic energy density. For a membrane inflated in air, T_s is equal to twice the surface tension. For membranes in contact with a substrate, however, T_s inside the contact region, T_{s_in}, is different from that outside the contact region, T_{s_out}. In Appendix 2.2 we re-derived the energy release rate taking into account of surface energy and found that (2.29) is still valid provided that T_ξ is interpreted using (2.50).

An important special case is where the membrane is the surface of a liquid drop resting on a substrate; in this case the elastic modulus goes to zero so the second term in (2.29) vanishes. Also, T_ξ^+ is the surface tension γ_{LV} of the liquid-vapor interface. The energy release rate (2.29) reduces to

$$G = \gamma_{LV}(1-\cos\theta). \tag{2.51}$$

The equilibrium configuration of the liquid drop requires the energy release rate to balance the work of adhesion, which is [21]

$$W_{ad} = \gamma_{LV} + \gamma_{SV} - \gamma_{SL}, \tag{2.52}$$

where γ_{SV}, γ_{SL} is the interfacial energy of the solid/vapor and solid/liquid interfaces respectively. Equating (2.51) to (2.52), we recover the Young's equation for liquid wetting. Note that the contact angle θ in (2.51) equals $\pi - \theta_c$, where θ_c is the usual definition of contact angle in liquid wetting literature.

2.6 Numerical results

We apply our formulation to a neo-Hookean membrane and present numerical results in this section. Whenever possible, we use material and geometric parameters that were reported in Flory *et al.* [8]. No-slip contact is assumed. For simplicity, we ignore the effect of fluid pressure and surface tension (T_s =0). In the following, all lengths are

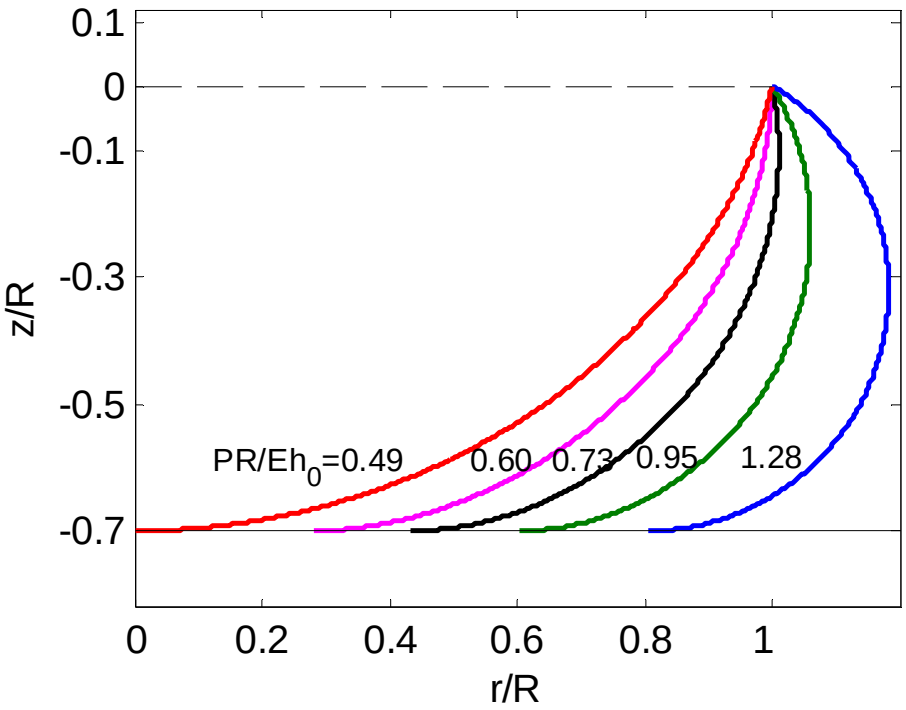

Figure 2.8 Inflated membrane profile at increasing applied pressure. The normalized applied pressures are $\overline{P} = 0.49$, 0.60, 0.73, 0.95 and 1.28. Note $\overline{P}_c = 0.49$ is the critical pressure to bring the membrane into initial contact.

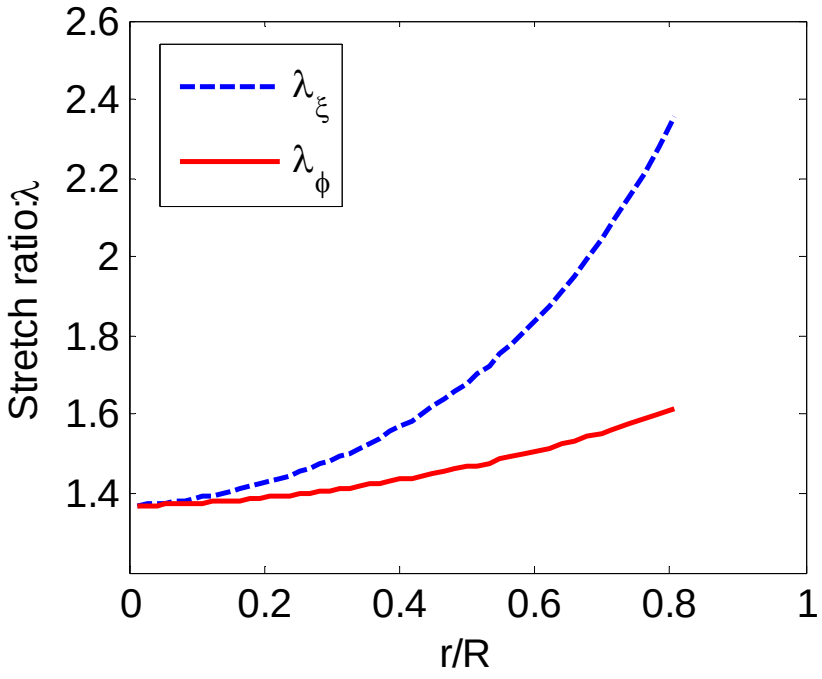

Figure 2.9 Stretch ratios λ_ξ and λ_ϕ in the contact region when $\bar{P} = 1.28$.

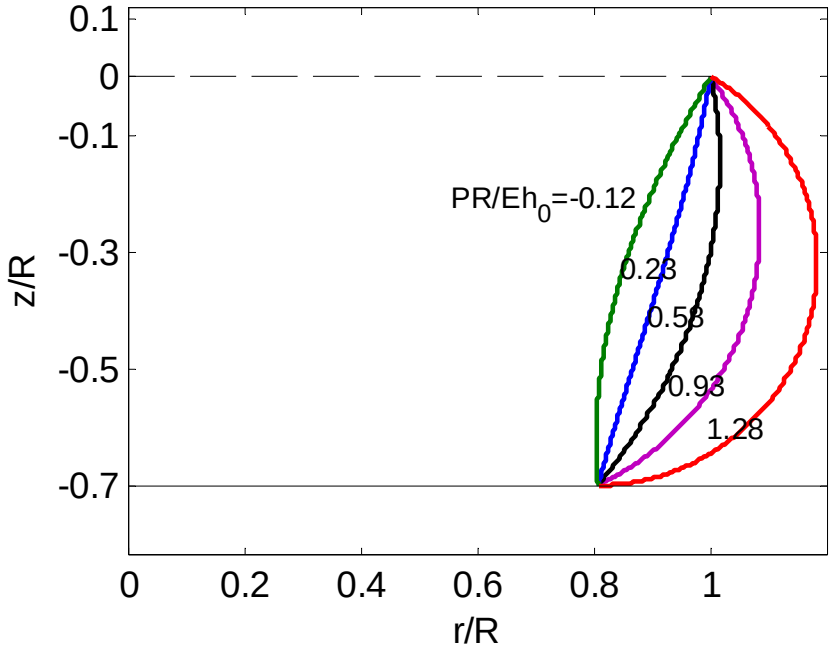

Figure 2.10 Membrane profile during deflation when the contact radius is pinned at $a/R = 0.81$ for five different applied pressures $\bar{P} = 1.28,\ 0.93,\ 0.58,\ 0.23,\ -0.12$. The pressure is reduced from an initial value of $\bar{P} = 1.28$.

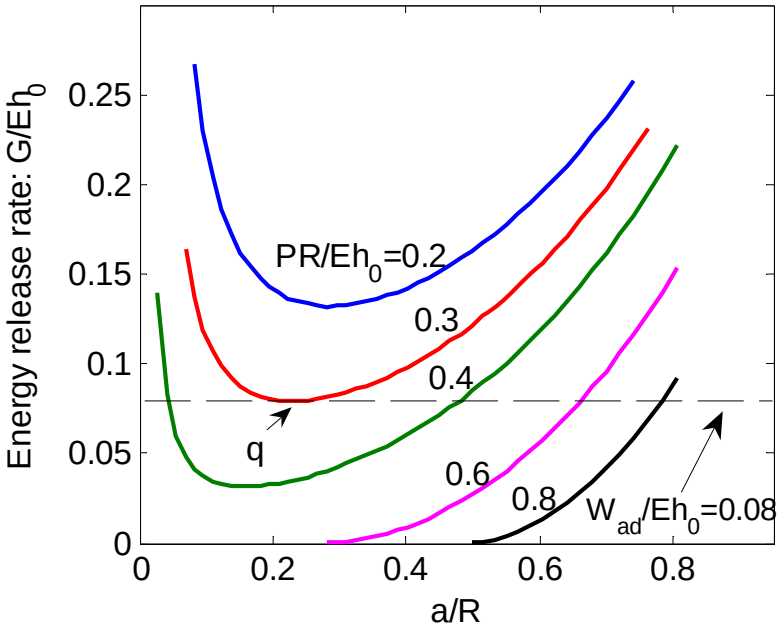

Figure 2.11 Energy release rate $\bar{G}$ versus contact radius a/R for different pressure PR/Eh_0 =0.2, 0.3, 0.4, 0.6 and 0.8.

normalized by R. The line tensions T_ϕ, T_ξ are normalized by Eh_0, where h_0 is the thickness of the undeformed membrane. The applied pressure P is normalized by Eh_o / R to give the following dimensionless pressure:

$$\bar{P} = \frac{PR}{Eh_0}. \tag{2.53}$$

In the simulations below, the normalized distance between the undeformed membrane and the substrate is $\bar{\delta}_d = \delta_d / R = 0.7$. The critical pressure needed to bring the membrane into contact with the substrate for this case is $\bar{P}_c = 0.49$ (see Figure 2.4c).

The evolution of the membrane profile during Stage 2 (inflation) is given in Figure 2.8. The maximum pressure we applied in our simulation is $\bar{P} = 1.28$. The resulting contact radius and contact area are $0.81R$ and $0.65A_0$ respectively, where $A_0 = \pi R^2$. Plots of the stretch ratios λ_ξ and λ_ϕ inside the contact region when $\bar{P} = 1.28$ are shown in Figure 2.9. Our result in Figure 2.9 shows that the latitudinal stretch λ_ϕ can be significantly smaller than the longitudinal stretch λ_ξ, in contrast to the case of frictionless contact, where they are equal. When the maximum contact area $0.65A_0$ ($\bar{P} = 1.28$) is achieved, we reduce the applied pressure. The membrane profile at the beginning of the Stage 3 (deflation) is shown in Figure 2.10, where contact line is pinned as the normalized pressure $\bar{P}$ decreases from 1.28 to -0.12. As the pressure is reduced, the contact angle and the energy release rate increases.

The energy release rate in this example is computed using (2.29). Figure 2.11 plots the normalized energy release rate $\bar{G} = G / Eh_o$ versus the normalized contact radius a / R for different normalized pressure $\bar{P}$. At a fixed pressure, the energy release rate is not monotonic, but reaches a minimum at some contact radius. Suppose the effective work of adhesion W_{ad} is a material constant (the horizontal dashed line in Figure 2.11), then it is tangent to some fixed normalized pressure curve at the point $q = (\bar{a}_q, \bar{G}_q)$ (see Figure 2.11). The branch of the curve to the right of q is stable since a reduction in

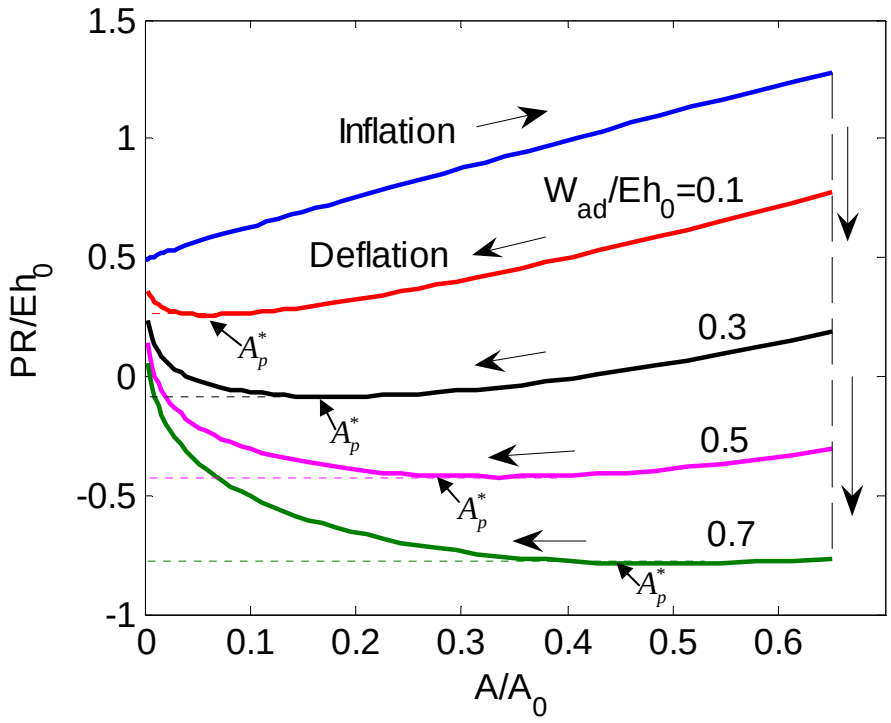

Figure 2.12 Pressure versus normalized contact area: A/A_0, where $A=\pi a^2$ and $A_0=\pi R^2$. The four curves for deflation phase correspond to normalized work of adhesion of W_{ad}/Eh_0=0.1, 0.3, 0.5 and 0.7. The pull-off instability points for the four deflation curves are indicated in the figure by the symbols A_p^*.

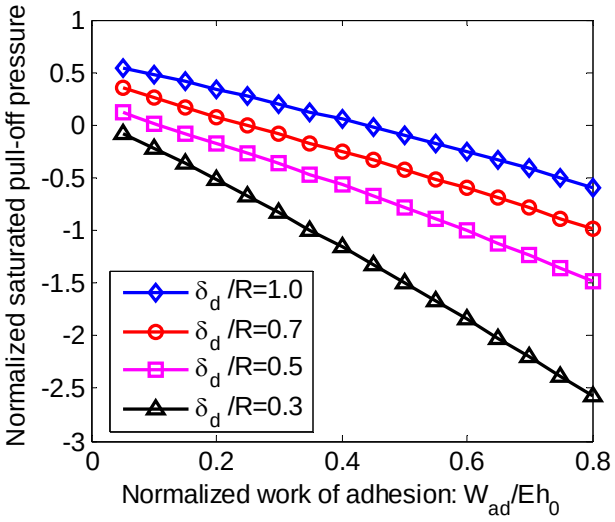

(a)

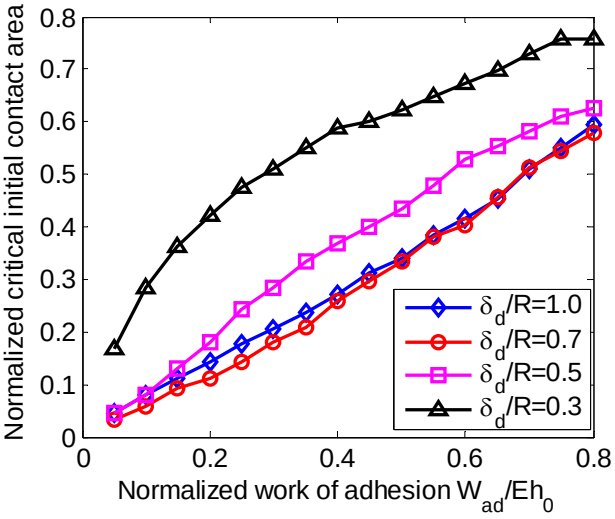

(b)

Figure 2.13 (a) Normalized saturated pull-off pressure $\bar{P}_p^* \equiv P_p^* R / Eh_0$ and (b) normalized critical initial contact area $\bar{A}_p^* \equiv A_p^* / A_0$ versus normalized work of adhesion W_{ad} / Eh_0. Several values of separation distance were considered, that is, $\delta_d / R = 1.0$ (diamond), 0.7 (circle), 0.5 (square), 0.3(triangle).

pressure is needed to decrease the contact radius. The branch of the curve to the left of q is unstable since decreasing the contact radius increases the energy release rate. Thus, unstable pull-off occurs at $q = (\overline{a}_q, \overline{G}_q)$. This instability corresponds to the minimum pressure in a pressure versus contact area plot which can be obtained using the detachment criterion $G = W_{ad}$. Several pressure versus contact area curves are shown in Figure 2.12 for different W_{ad}. Note pinning of contact line as the pressure is reversed at $A / A_0 \approx 0.65$. The lines below the inflation line show the pressure needed to unpin the contact and to decrease the contact area using different values of W_{ad}. For $W_{ad} = 0.1Eh_0$, there is an instability associated with pull-off at $A_p^* / A_0 \approx 0.06$, where A_p^* is the contact area at instability. Because of adhesion, the pull-off pressure (the pressure at instability), denoted by P_p, is substantially less than P_c ($\approx 0.49Eh_0 / R$), the pressure needed to bring the inflated membrane into contact with the substrate. Note that if the applied pressure is sufficiently small so that the contact area A at the end of the inflation phase is less than A_p^*, then pull-off will occur immediately after contact line unpins. In this regime, P_p depends on the initial contact area achieved in the inflation phase. In other words, the pull-off pressure is sensitive to the pressure applied in the inflation phase (Stage 2). However, when the applied pressure is sufficiently large so that the contact area A at the end of the inflation phase is equal to or greater than A_p^*, then the pull off pressure P_p is independent of the applied pressure in the inflation phase (Stage 2), we call this the saturated pull-off pressure P_p^*.

Figure 2.13 shows how the saturated pull-off pressure P_p^* and A_p^* depend on the work of adhesion and the initial separation δ_d. To reduce the number of simulation parameters, normalized variables are used in Figure 2.13a,b. Figure 2.13a allows one to determine the effective work of adhesion W_{ad} using the measured saturated pull-off pressure P_p^*.

2.7 Summary and Discussion

We developed a large deformation theory to study the adhesion and contact mechanics of a circular membrane inflated by the application of pressure. Both frictionless and no-slip contact conditions were considered in our formulation. We also extended our theory to include fluid pressure and surface tension. The membranes used in experiments are typically very soft and thin; thus allowing us to neglect bending deformation. Begley and Mackin [22] showed that the bending deformation in the membrane can be neglected if the dimensionless parameter

$$\chi = \left[12\left(1-\nu^2\right)\right]^{3/2}\left(\frac{FR^2}{Eh_0^4}\right) \tag{2.54}$$

is very large, where ν is the Poisson's ratio of the membrane and F is the total force acting on the membrane. For membranes loaded under uniform pressure P, $F=\pi R^2 P$. For example, for a clamped circular membrane under uniform pressure, the error in pressure-deflection relation made by neglecting bending deformation is less than 10% if $\chi > 2\times 10^3$ [22]. The Young's modulus E for membranes of our interest [8] is from $14KPa$ to $6MPa$ and the membrane thickness h_0 is from $1\mu m$ to $10\mu m$. Using $P=100Pa$, $R=3.5mm$, $E=6MPa$, $\nu=0.5$ and $h_0=10\mu m$, we obtain a lower bound of χ, i.e., $\chi=2\times 10^7$, which is four orders of magnitude larger than 2×10^3. One may also question our theory by noticing an infinite curvature on the contact edge when $\theta \neq 0$. This is not unlike the JKR theory [1], which is based on the existence of a stress singularity at the edge of the contact zone. The linear elastic solution in this case must break down as the edge is approached. This is analogous to the fact that our membrane solution must break down as the contact edge is approached, where bending and other three dimensional effects must be taken into consideration. Just as in JKR theory, we assume that bending and other three dimensional effects are confined in a small region near the contact edge. This region is much smaller than any length scale in our problem.

As a result, the energy balance equation is independent of these effects.

A key result in this work is the derivation of the energy release rate for a fully nonlinear membrane in contact with a flat rigid surface. Our analysis shows that the energy release rate is completely determined by the contact angle, the stretch ratios and the longitudinal component of the line tension at the contact line. Note that, as long as there is adhesion, the longitudinal extension ratio, λ_ξ, is discontinuous at the contact line. The energy release rate we derived, (2.29), is valid for the limiting cases of no-slip and frictionless contact. The fact that the same expression is valid for these two limiting cases suggests that it may be valid for intermediate cases as well.

Our energy release rate expression (2.29) can be applied to the peeling of a plane strain membrane by setting $\lambda_\phi = 1$, i.e., the energy release rate in a plane strain peel test ($\lambda_\phi = 1$) can be obtained by interpreting λ_ξ^- in (2.29) as the pre-stretch ratio. Chen *et al.* [23] derived the energy release rate in a plane strain peel test where a pre-stretched thin film is detached from a rigid substrate. Their energy release rate is based on infinitesimal strain theory. We show that our expression reduces to theirs if the strains are infinitesimal. In this case $T_\xi^+ = T$, where T is the peel force. For infinitesimal strains, we have

$$\lambda_\xi^+ = 1 + \frac{T}{E^* h_0}, \qquad \lambda_\xi^- = 1 + \frac{T_p}{E^* h_0}, \tag{2.55}$$

where T_p is the pretension, $E^* = E/\left(1-\nu^2\right) = 4E/3$ is the plane strain modulus for our case of incompressible materials. For infinitesimal deformations, neo-Hookean model reduces to linear elastic solid. Using $\lambda_\phi = 1$, $T/E^* h_0 << 1$, $T_p/E^* h_0 << 1$ and (2.55), equation (2.34) can be simplified by keeping only the first order terms, to obtain the following,

$$G = T\left(1-\cos\theta\right) + \frac{T^2}{2E^* h_0} - \frac{TT_p}{E^* h_0} + \frac{T_p^2}{2E^* h_0}, \tag{2.56}$$

which is identical to the energy release rate given in Chen *et al.* [23] (Equation 2.5). If the pretension $T_p = 0$, (2.56) reduces to Kendall's expression of energy release rate of peeling an elastic film [24].

The definition of energy release rate is subtle in large deformation theory. To the best of our knowledge, this subtlety has not been examined. In this chapter, the energy release rate is defined as the energy released per unit area of *deformed* membrane element that is detached from the substrate. In the literature of rubber facture mechanics, however, the energy release rate is usually defined with respect to the reference undeformed configuration [25-27]. Using this convention, the energy release rate is the release of elastic energy when a unit undeformed area element directly ahead of the contact line is detached, that is,

$$G_{undeform} \equiv -\lim_{d\rho \to 0} \frac{\Delta \Gamma}{2\pi \rho^* d\rho}. \tag{2.57}$$

Comparing (2.57) with (2.27), we obtain

$$G_{undeform} = \frac{ada}{\rho^* d\rho} G = \lambda_\xi^- \lambda_\phi G, \tag{2.58}$$

where we have used (2.22). The condition for making or breaking contact is

$$G_{undeform} = \lambda_\xi^- \lambda_\phi G = W_{ad}^{un}, \tag{2.59}$$

where W_{ad}^{un} is the effective work of adhesion in the *undeformed reference configuration*. The two different definitions are identical if and only if

$$\lambda_\xi^- \lambda_\phi W_{ad} = W_{ad}^{un}. \tag{2.60}$$

Since $\lambda_\xi^- \lambda_\phi$ is area stretch ratio of the contacting membrane on the contact edge, the two formulations are equivalent if stretching an area element changes *only* the area density of adhesive molecules on the membrane but not the details of their interaction with the substrate.

Finally, we point out that our theory assumes that the membrane is elastic, and the only place where dissipation occurs is in the vicinity of the contact line. In most practical systems this is not the case; the energy dissipation may be due to the mechanical hysteresis of the membrane itself (e.g. a viscoelastic membrane). For viscoelastic membranes, one has to include the viscous dissipation in the membranes while considering the energy balance. Therefore, the energy release rate expression (2.29) is not valid any more.

APPENDIX 2.1

DERIVATION OF ENERGY RELEASE RATE FOR FRICTIONLESS CONTACT

For frictionless contact, equation (2.17) becomes

$$\Delta\Gamma = \left(\Delta U_1 - \Delta W_{P1}\right) + \left(\Delta U_2 - \Delta W_{P2}\right) + \Delta U_3 . \tag{A2.1}$$

The additional term ΔU_3 is the change in elastic energy of the membrane in the contact region (i.e., $\rho \in [0, \rho^* - d\rho]$), since it can shrink by sliding on the substrate during the detachment of part 2. Energy balance implies ΔU_3 equals the work done by the line tension T_ξ^- acting at the material point $\rho = \rho^* - d\rho$ as this point slides on the substrate by the amount of $\left(\rho^* - d\rho\right) d\lambda_\xi^-$ (see (2.31)). Note that the line tension T_ξ is discontinuous at the contact edge due to non-zero contact angle (see (2.45)), so is the stretch ratio λ_ξ. We use T_ξ^+, T_ξ^- to denote the line tension T_ξ as one approaches the contact edge from the outside and the inside respectively. Therefore, the first order term of ΔU_3 is

$$\Delta U_3 = 2\pi a T_\xi^- \left(\rho^* - d\rho\right) d\lambda_\xi^- = -2\pi a T_\xi^- \left(da\right)_s , \tag{A2.2}$$

where we have used (2.31). Using the same method shown in section 2.3.2.1, we find that

$$\Delta U_1 - \Delta W_{P1} = 2\pi a T_\xi^+ \cos\theta da - 2\pi a T_\xi^+ da^* , \tag{A2.3}$$

$$\Delta U_2 - \Delta W_{P2} = 2\pi\rho^* h_0 d\rho \left(W(\lambda_\xi^+, \lambda_\phi) - W(\lambda_\xi^-, \lambda_\phi)\right) = 2\pi\rho^* h_0 d\rho \Delta W , \tag{A2.4}$$

where ΔW is defined in (2.28). Combining (A2.1) to (A2.4) and using (2.32), we obtain

$$\Delta\Gamma = 2\pi a \left[T_\xi^+ \cos\theta \left(da\right)_d - T_\xi^+ da^* + \frac{\rho^*}{a} h_0 d\rho \Delta W + \left(T_\xi^+ \cos\theta - T_\xi^-\right)\left(da\right)_s \right]. \tag{A2.5}$$

Force balance shows that $T_\xi^+ \cos\theta - T_\xi^- = 0$ at the contact edge (see (2.45) and Figure

2.7). Using this result, (A2.5) becomes

$$\Delta\Gamma = 2\pi a T_{\xi}^{+} \cos\theta \left(da\right)_d - 2\pi a T_{\xi}^{+} da^{*} + 2\pi\rho^{*} h_0 d\rho\Delta W \,. \tag{A2.6}$$

To first order, da^{*} is given by (2.23) and da_d by (2.30). Therefore,

$$\Delta\Gamma = -2\pi a T_{\xi}^{+} \left(da\right)_d \left(\frac{\lambda_{\xi}^{+}}{\lambda_{\xi}^{-}} - \cos\theta \right) + 2\pi\rho^{*} h_0 d\rho\Delta W \,, \tag{A2.7}$$

which is the same as (2.26) except da is replaced by $\left(da\right)_d$. Using (2.30) and (2.33), we can show that the energy release rate *G* for frictionless contact has the same form as the no-slip contact, i.e., (2.29) is also valid for frictionless contact.

APPENDIX 2.2

DERIVATION OF ENERGY RELEASE RATE WITH SURFACE ENERGY

We first assume no-slip condition and follow the same method presented in section 2.3.2.1. Equation (2.17), including change in the surface energy, becomes:

$$\Delta\Gamma^* = \left(\Delta U_1 + \Delta U_{T1} - \Delta W_{P1}\right) + \left(\Delta U_2 + \Delta U_{T2} - \Delta W_{P2}\right) \quad , \tag{A2.8}$$

where ΔU_{T1} and ΔU_{T2} denote respective surface energy change of membrane part 1 and part 2 (see Figure 2.3). The first bracketed term in (A2.8) equals the work done by the tension T_ξ^+ to carry *A* to *A'*, i.e.

$$\Delta U_1 + \Delta U_{T1} - \Delta W_{P1} = -2\pi a T_\xi^+ da\left(\frac{\lambda_\xi^+}{\lambda_\xi^-} - \cos\theta\right), \tag{A2.9}$$

where the tension T_ξ^+ is

$$T_\xi^+ = T_{s\_out} + \frac{h_0}{\lambda_\phi}\frac{\partial W}{\partial \lambda_\xi}\bigg|_{\xi=\xi^+} \tag{A2.10}$$

Note that T_{s_in} and T_{s_out} are the respective surface tension for membrane elements inside and outside the contact region. For membrane part 2, ΔW_{P2} can be neglected and ΔU_2 is still given by (2.25). The change in surface energy ΔU_{T2} is

$$\Delta U_{T2} = 2\pi a T_{s\_out} da^* - 2\pi a T_{s\_in} da = 2\pi a da\left(T_{s\_out}\frac{\lambda_\xi^+}{\lambda_\xi^-} - T_{s\_in}\right). \tag{A2.11}$$

Combining (A2.8), (A2.9), (2.25) and (A2.11), we obtain

$$\Delta\Gamma^* = -2\pi a T_\xi^+ da\left(\frac{\lambda_\xi^+}{\lambda_\xi^-} - \cos\theta\right) + 2\pi\rho^* h_0 d\rho\Delta W + 2\pi a da\left(T_{s\_out}\frac{\lambda_\xi^+}{\lambda_\xi^-} - T_{s\_in}\right). \tag{A2.12}$$

Using (A2.10) and (A2.12), we can show that

$$-\lim_{da\to 0}\frac{\Delta\Gamma^*}{2\pi a da} = \left(T_{s\_in} - T_{s\_out}\right) + T_\xi^+\left(1-\cos\theta\right) + \frac{h_0}{\lambda_\phi\lambda_\xi^-}\left(\frac{\partial W}{\partial\lambda_\xi}\bigg|_{\xi=\xi^+}\Delta\lambda_\xi - \Delta W\right). \tag{A2.13}$$

The first term in (A2.13), (T_{s_in} -T_{s_out}), is the difference in the surface energy of the

membrane inside or outside the contact region. This term is a part of the work of adhesion and should not be included in our energy release rate expression. Therefore, the energy release rate is given by the last two terms in (A2.13), i.e.,

$$G = T_{\xi}^{+}\left(1-\cos\theta\right)+\frac{h_0}{\lambda_{\phi}\lambda_{\xi}^{-}}\left(\left.\frac{\partial W}{\partial \lambda_{\xi}}\right|_{\xi=\xi^{+}}\Delta\lambda_{\xi}-\Delta W\right), \tag{A2.14}$$

where T_{ξ}^{+} is given by (A2.10) and W is the elastic work function of the material. Using a similar procedure as above, we have verified that this result is also valid for frictionless contact.

REFERENCES

[1] Johnson K.L., Kendall K., Roberts A.D., 1971, *Proc. R. Soc. London Ser. A*, **324**, 301-313.

[2] Maugis D., Barquins M., 1978, *J. Phys. D: Appl. Phys.*, **11**, 1989-2023.

[3] Shanahan M.E.R., 1995, *CR. Acad. Sci. Ser. II-B*, **321**, 259-264.

[4] Shanahan M.E.R., 1997, *J. Adhesion*, **63**, 15-29.

[5] Shanahan M.E.R., 2000, *CR. Acad. Sci. Ser. IV*, **1**, 517-522.

[6] Wan K.T., 2001, *J. of Adhesion*, **75**, 369-380.

[7] Wan K.T., Kogut L., 2005, *J. Micromech. Microeng.*, **15** 778-784.

[8] Flory A.L., Brass D.A., Shull, K.R., 2007, *J. Polym. Sci., Part B: Polym. Phys.* **45**, 3361-3374.

[9] Plaut R.H., White S.A., Dillard D.A., 2003, *Int. J. Adhes. Adhes.*, **23**, 207-214.

[10] Feng W.W., Yang W.H., 1973, *J. Appl. Mech.*, **40**, 209-214.

[11] Libai A., Simmonds J.G., 1998, *The nonlinear theory of elastic shells (2nd edition)*, Cambridge University Press, New York.

[12] Klingbeil W.W., Shield R.T., 1964, *ZAMP*, **15**, 608-629.

[13] Shull K.R., 2002, *Mater. Sci. Eng., R*, **36**, 1-45.

[14] Williams J.G., 1997, *Int. J. Fract.*, **87**, 265-288.

[15] Wan K.T., Liu K.K., 2001, *Med. Biol. Eng. Comput.*, **39**, 605-608.

[16] Nadler B., Tang, T., 2008, *Int. J. NonLin. Mech.*, **43**, 716-721.

[17] Hart-Smith L.J., Crisp J.D.C., 1967, *Int. J. Engr. Sci.*, **5**, 1-24.

[18] Hassager O., Kristensen S.B., Larsen J.R., Neergaard J., 1999, J. *Non-Newtonian Fluid Mech.*, **88**, 185-204.

[19] Gent A.N., Wang C., 1991, *J. Mater. Sci.*, **26**, 3392-3395.

[20] Crosby A.J., Shull K.R., Lakrout H., Creton C., 2000, *J. Appl. Phys.*, **88**,

2956-2966.

[21] Israelachvili J.N., 1992, *Intermolecular and surface forces, (2nd edition)* Academic press, London.

[22] Begley M.R., Mackin T.J., 2004, *J. Mech. Phys. Solids*, **52**, 2005-2023.

[23] Chen B., Wu P.D., Gao H.J., 2009, *J. R. Soc. Interface*, **6**, 529-537.

[24] Kendall K., 1975, *J. Phys. D: Appl. Phys.*, **8**, 1449-1452.

[25] Rivlin R.S., Thomas A.G. 1953, *J. Polym. Sci.* **10**, 291-318.

[26] Eshelby, J.D., 1975, *J. Elasticity*, **5**, 321-335.

[27] Yeoh, O.H., 2002, *Mech. Mater.*, **34**, 459-474.

CHAPTER 3

FINITE STRAIN ANALYSIS OF CRACK TIP FIELDS IN INCOMPRESSIBLE HYPERELASTIC SOLIDS LOADED IN PLANE STRESS[2]

3.1 Introduction

A fundamental problem in fracture mechanics is to determine the stress and deformation fields near the tip of a crack. These local fields can provide important information on the separation processes. For example, a highly triaxial stress state (e.g. hydrostatic tension) near the crack tip promotes cavitation and suppresses plastic deformation. These fields also provide useful loading parameters (such as energy release rate) which quantify the severity of the local deformation. Another use of these fields is that they provide asymptotic boundary conditions on analysis of separate processes.

For stiff materials such as ceramics and polymer glasses, these asymptotic stress and deformation fields can be derived using linear elasticity. The loading parameters associated with these asymptotic fields (e.g. stress intensity factor) formed the basis of linear elastic fracture mechanics (LEFM). LEFM assumes that large deformation and deviations from Hooke's law are confined in a region that is small compared to relevant specimen dimensions. This assumption often breaks down for soft materials such as gels and elastomers since these materials usually undergo very large deformation because of their low modulus (*kPa-MPa*). In addition, the relation between stress and deformation in soft materials is nonlinear as most elastomers strain harden at moderate to large deformation. As a result, the LEFM crack tip stress field may have very limited region of dominance, especially when the applied load is large. Nonlinear elastic behavior near the crack tip can significantly influence crack growth even when the overall deformation is small. For example, atomistic simulations of dynamic crack growth [1,2] have shown

[2] Long R., Krishnan V.R., Hui C.Y., 2010, submitted for publication.

that local hyper-elasticity governs crack speed and crack kinking instabilities. Livne *et al.* [3] experimentally demonstrated a hierarchy of local deformation fields at the tip of a dynamically growing crack in a brittle polyacrylamide gel. They found that the displacement gradient has a $1/r$ singularity inside the $1/\sqrt{r}$ field predicted by LEFM. This hierarchy of local crack tip fields was theoretically studied by Bouchbinder *et al.* [4,5].

Finding crack tip fields consistent with the fully nonlinear equation of hyperelasticity is a non-trivial problem. Unlike linear elastic theory, the governing equations are highly nonlinear and are very difficult to solve analytically or even numerically. There are several pioneering works on the asymptotic crack tip field of hyperelastic solids. Wong and Shield [6] considered the problem of a finite crack in a biaxially loaded infinite sheet of incompressible neo-Hookean solid (ideal rubber). Knowles and Steinberg [7-8] studied the asymptotic deformation field near the tip of a Mode-I plane strain crack for a class of compressible hyperelastic solids. Stephenson [9] determined the asymptotic deformation fields of a plane strain crack in an incompressible hyperelastic solid under mix-mode condition. Knowles [10] solved the problem of a Mode III crack in hyperelastic solids. Geubelle and Knauss (GK) [11] determined the plane stress crack tip solutions for incompressible generalized neo-Hookean (GNH) solids. Tarantino [12] studied the plane stress crack tip field in a compressible neo-Hookean solid. Interface cracks between two different hyperelastic materials were also studied, either in plane stress [13-15] or in plane strain [16].

To put our work into perspective, we briefly review GK's work, where the deformation and stress fields near the tip of a plane stress crack in generalized neo-Hookean (GNH) materials were determined. The GNH model was first introduced by Knowles in his study of Mode-III cracks [10]. The work function W of a GNH solid is

$$W = \frac{\mu}{2b}\left\{\left[1+\frac{b}{n}\left(I-3\right)\right]^{n}-1\right\}, \tag{3.1}$$

where μ is the small strain shear modulus, I is the sum of the square of the three principal stretches, $b > 0$ and $n > 1/2$ are material parameters. In uniaxial tension, GK have shown that b controls the extent of linearity and n the degree of strain hardening. When $n=1$, (3.1) reduces to the neo-Hookean solid (ideal rubber). The condition $n > 1/2$ ensures that the elastostatic equilibrium equations are elliptic [11]. In particular, GK have shown that the condition $n < 1/2$ leads to unstable behavior in uniaxial tension, i.e., the nominal tensile stress decreases as the stretch ratio increases.

There are difficulties in GK's analysis. As pointed out by GK, their asymptotic analysis is only valid for $n < n^*$. They found numerically that $n^* \approx 1.4$. This regime corresponds to materials with very low strain hardening. However, realistic constitutive models for elastomers exhibit very high strain hardening [17,18]. For example, it is well known that the neo-Hookean model (n=1 in (3.1)) substantially underestimates the degree of strain hardening for most elastomers [19]. In GK's analysis, the deformed coordinates of a material point is assumed to be separable functions of r and θ, where (r,θ) is a polar coordinate system with origin at the undeformed crack tip. Furthermore, they assumed the dependence of the deformation field on r is of power form. We point out that the assumptions of separable displacement fields and in particular the power dependence on r were used in all previous plane stress/strain asymptotic crack tip analysis. These assumptions restrict the analysis of crack tip fields to work functions which has a power dependence on the invariant I (e.g. (3.1)). However, more realistic material models such as the Arruda-Boyce model [17], Gent's model [18] and the exponentially hardening model [20] do not have power dependence on I. For these materials, the crack tip deformation fields may not be separable functions of r and θ. Even if separable solutions exist, the dependence on r may not be of power

form. These limitations motivate us to develop a new method that can be applied to a wider class of material models.

In this chapter, we focus on the leading order behavior of the deformation and stress fields near the tip of a Mode I plane stress crack in a homogeneous isotropic incompressible hyperelastic solid. Our analysis is partly motivated by recent experiments on fracture of elastic gels, which were carried out under predominantly plane stress conditions [20-22]. The plan of this chapter is as follows. Section 3.2 summarizes the finite deformation theory for plane stress problems. The asymptotic analysis for the leading order behavior of the deformation and stress fields of a Mode I plane stress crack is introduced in section 3.3. In sections 3.4 and 3.5, we apply this method to determine the crack tip fields for the GNH and an exponential hardening material respectively. Specifically, in section 3.4, we revisit the GNH model considered by GK and show that our technique can be used to deduce the dominant stress fields for *any* $n > 1/2$. We also use finite element method (FEM) to verify our asymptotic results. Summary and discussions are given in section 3.6.

3.2 Finite Strain Plane Stress Elastostatics

The finite strain plane stress elasticity formulation used in this work was derived in detail by Knowles and Steinberg [13]. Here we present a brief summary of the governing equations. For the purpose of asymptotic analysis, we need only to consider a semi-infinite straight crack in an infinite plate (see Figure 3.1a). A Cartesian coordinate system (x_1, x_2) with origin at the undeformed crack tip is used to denote the mid-plane coordinates of a material point in the undeformed reference configuration. The undeformed crack lies on the negative x_1 axis with its tip at the origin. We also define a polar coordinate system (r, θ) where $r = \sqrt{x_1^2 + x_2^2}$ and $\theta = \tan^{-1}\left(x_2 / x_1\right)$. In this work, Greek subscripts range from one to two. Also, bolded letters represent tensors in

three dimensions. For convenience, we use another Cartesian coordinate system (y_1, y_2) with the origin at the displaced crack tip to describe the deformed configuration (see Figure 3.1b). The deformed coordinates y_α of a mid-plane material point at (r, θ) or (x_1, x_2) are related to its displacements u_α by

$$y_\alpha = x_\alpha + u_\alpha - d_\alpha, \tag{3.2}$$

where d_α is the displacement of the crack tip, i.e., $d_1 = u_1(x_1 = 0, x_2 = 0), d_2 = 0$ for a Mode I crack.

The deformation gradient tensor $F_{\alpha\beta}$ is

$$F_{\alpha\beta} = \delta_{\alpha\beta} + u_{\alpha,\beta} \quad , \tag{3.3}$$

where $,_\beta \equiv \partial / \partial x_\beta$. In the absence of body forces, the equilibrium equations in the reference coordinates are

$$S_{\alpha 1,1} + S_{\alpha 2,2} = 0, \tag{3.4}$$

$$S_{\alpha 1} F_{\xi 1} + S_{\alpha 2} F_{\xi 2} = F_{\alpha 1} S_{\xi 1} + F_{\alpha 2} S_{\xi 2} \quad , \tag{3.5}$$

where $S_{\alpha\beta}$ is the first Piola-Kirchhoff stress tensor. The traction free crack boundary conditions in the reference configuration are:

$$S_{22} = 0, S_{12} = 0 \qquad \text{at} \quad \theta = \pm\pi. \tag{3.6}$$

The constitutive model of a homogeneous isotropic incompressible hyperelastic solid is specified by its work function $W = U(I, I_2)$, where I, I_2 are the trace and the second invariant of Cauchy-Green tensor, i.e., $\mathbf{F}^T\mathbf{F}$ or $\mathbf{F}\mathbf{F}^T$. In this chapter, the work function is assumed to have the following form:

$$W = U(I) \ , \tag{3.7}$$

where U is a smooth function such that

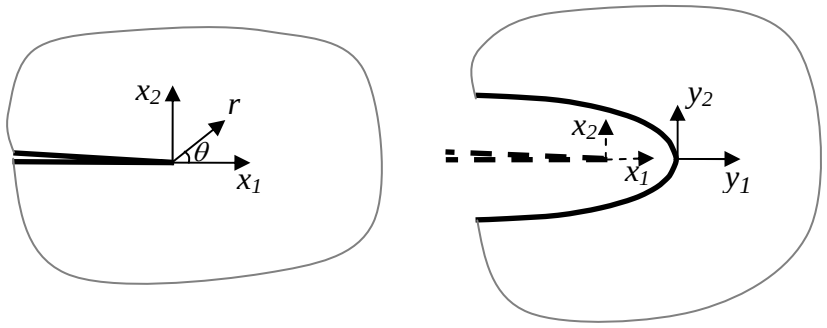

Figure 3.1 (a) Undeformed reference configuration of a semi-infinite crack in a homogeneous incompressible hyperelastic solid; (b) Deformed configuration of the crack. Dashed lines represent the undeformed crack. Note that the origin of the deformed coordinates y_α is located at the displaced crack tip.

$$U(I) \geq 0 . \tag{3.8}$$

The equality sign in (3.8) holds only for $I = 3$ so that the work function vanishes in the undeformed state. In plane stress, the three principal stretches consist of two in-plane principal stretches λ_α and an out of plane stretch λ. Note that I can also be expressed as the sum of the square of three principal stretches, that is,

$$I = \lambda_1^2 + \lambda_2^2 + \lambda^2 = (y_{1,1})^2 + (y_{1,2})^2 + (y_{2,1})^2 + (y_{2,2})^2 + \lambda^2 . \tag{3.9}$$

The incompressibility condition requires

$$\det F_{\alpha\beta} = y_{1,1}\, y_{2,2} - y_{1,2}\, y_{2,1} = 1/\lambda . \tag{3.10}$$

The relationship between deformation and the first Piola-Kirchhoff stress is given by [13]

$$S_{\alpha\beta} = 2\frac{dU}{dI}\left(F_{\alpha\beta} - \lambda^2 F^{-1}_{\beta\alpha}\right). \tag{3.11}$$

In matrix form, (3.11) is

$$\begin{bmatrix} S_{11} & S_{12} \\ S_{21} & S_{22} \end{bmatrix} = 2\frac{dU}{dI}\begin{bmatrix} y_{1,1} - \lambda^3 y_{2,2} & y_{1,2} + \lambda^3 y_{2,1} \\ y_{2,1} + \lambda^3 y_{1,2} & y_{2,2} - \lambda^3 y_{1,1} \end{bmatrix} . \tag{3.12}$$

The partial differential equations governing the deformed coordinates y_α are obtained by substituting (3.12) into (3.4):

$$\nabla^2 y_1 = (\lambda^3)_{,1} y_{2,2} - (\lambda^3)_{,2} y_{2,1} - \frac{d^2U/dI^2}{dU/dI}(y_{1,1}I_{,1} - \lambda^3 y_{2,2}I_{,1} + y_{1,2}I_{,2} + \lambda^3 y_{2,1}I_{,2}), \tag{3.13a}$$

$$\nabla^2 y_2 = (\lambda^3)_{,2} y_{1,1} - (\lambda^3)_{,1} y_{1,2} - \frac{d^2U/dI^2}{dU/dI}(y_{2,1}I_{,1} + \lambda^3 y_{1,2}I_{,1} + y_{2,2}I_{,2} - \lambda^3 y_{1,1}I_{,2}) . \tag{3.13b}$$

Using (3.12), the traction free boundary conditions on the crack faces (3.6) become:

$$y_{1,2} + \lambda^3 y_{2,1} = 0 , \tag{3.14a}$$

$$y_{2,2} - \lambda^3 y_{1,1} = 0 . \tag{3.14b}$$

Our goal is to find the leading order asymptotic solution for the stress and deformation fields as $r \to 0$.

3.3 Asymptotic Method for Smooth Work Functions

In this section, we present an asymptotic method to determine the leading order behavior of the stress and deformation fields near the tip of a Mode I plane stress crack. In Mode I, the deformed coordinates must satisfy the symmetry conditions:

$$y_1(x_1, x_2) = y_1(x_1, -x_2), \qquad y_2(x_1, x_2) = -y_2(x_1, -x_2). \tag{3.15}$$

To avoid a cusp-like or a wedge-like opening profile for a traction free crack, the condition,

$$\left|\frac{\partial y_2(r, \theta = \pi)}{\partial r}\right| >> \left|\frac{\partial y_1(r, \theta = \pi)}{\partial r}\right| \quad \text{as} \quad r \to 0 \quad , \tag{3.16a}$$

must be satisfied on the crack face. This condition motivates us to assume

$$\left|y_{2,\alpha}\right| >> \left|y_{1,\alpha}\right| \tag{3.16b}$$

in a region surrounding the crack tip. *The condition imposed by (3.16b) is consistent with all previous works on Mode I crack tip fields.* Note that if the dominant crack tip strain field $y_{2,\alpha}$ is singular, the out of plane stretch λ must vanish as $r \to 0$, as demanded by the incompressibility condition (3.10). This fact and (3.16b) imply that

$$\left|y_{2,1}\right| >> \left|\lambda^3 y_{1,2}\right| \text{ and } \left|y_{2,2}\right| >> \left|\lambda^3 y_{1,1}\right| \quad \text{as} \quad r \to 0. \tag{3.17}$$

According to (3.9) and (3.16b), the leading order behavior of I is completely determined by $y_{2,\alpha}$, i.e.,

$$I = y_{2,1}^2 + y_{2,2}^2 + \text{higher order terms} \quad \text{as} \quad r \to 0. \tag{3.18}$$

Combining (3.12), (3.17) and (3.18), we obtain the following leading order behavior of $S_{2\alpha}$,

$$S_{2\alpha} = \Sigma(\gamma^2) y_{2,\alpha} \equiv \frac{\tau(\gamma)}{\gamma} y_{2,\alpha} \qquad \text{as} \quad r \to 0\,, \tag{3.19a}$$

where

$$\Sigma\left(\gamma^2\right) \equiv 2\frac{dU}{dI}\,, \tag{3.19b}$$

$$\gamma \equiv \sqrt{y_{2,1}^2 + y_{2,2}^2} \approx \sqrt{I}\,, \quad \tau(\gamma) \equiv \gamma\Sigma\left(\gamma^2\right). \tag{3.19c}$$

Equations (3.19a) and (3.19c) imply that, to leading order,

$$\tau = \sqrt{S_{21}^2 + S_{22}^2}\,. \tag{3.20}$$

Equations (3.19a-c) suggest that y_2 is decoupled from y_1 in the leading order analysis. Indeed, the equilibrium equation $S_{21,1} + S_{22,2} = 0$ reduces to

$$\left(\Sigma(\gamma^2) y_{2,1}\right)_{,1} + \left(\Sigma(\gamma^2) y_{2,2}\right)_{,2} = 0\,. \tag{3.21}$$

The boundary condition (3.14b), to leading order, is

$$y_{2,2}(r, \theta = \pm\pi) = 0\,. \tag{3.22}$$

Equations (3.21) and (3.22) completely determine the leading order behavior of y_2 near the crack tip.

The nonlinear governing equation (3.21) can be transformed to a linear equation by treating the physical coordinates x_α as functions of the strains $\gamma_\alpha \equiv y_{2,\alpha}$. Detailed derivation of this transformation can be found in an earlier work by Rice [23], where an anti-plane shear (Mode III) crack was studied. To follow Rice's formulation, we identify y_2 as the out of plane displacement, u_3, of an anti-plane shear crack problem. Rice [23] has shown that there exists a function $\psi(\gamma_1, \gamma_2)$ such that

$$x_\alpha = \partial\psi / \partial\gamma_\alpha\,. \tag{3.23}$$

Following Rice [23], we use a polar strain coordinate system (γ, ϕ), defined by

$$\gamma_1 = -\gamma\sin\phi\,, \quad \gamma_2 = \gamma\cos\phi \quad , \qquad \phi \in \left[-\pi/2, \pi/2\right]. \tag{3.24a}$$

Note that $\gamma_2 \equiv y_{2,2} > 0$ for all x_α in Mode I condition. In polar strain coordinates, (3.23) becomes [23]

$$x_1 = -\sin\phi \frac{\partial \psi}{\partial \gamma} - \frac{\cos\phi}{\gamma} \frac{\partial \psi}{\partial \phi} \quad , \qquad x_2 = \cos\phi \frac{\partial \psi}{\partial \gamma} - \frac{\sin\phi}{\gamma} \frac{\partial \psi}{\partial \phi} \, . \tag{3.24b}$$

Using (3.23), (3.24a,b) and $y_{2,\alpha} \equiv \gamma_\alpha$, (3.21) can be transformed to a *linear* partial differential equation (PDE) with γ and ϕ as independent variables (see [23]), i.e.,

$$\frac{\tau}{\gamma \tau'(\gamma)} \frac{\partial^2 \psi}{\partial \gamma^2} + \frac{1}{\gamma} \frac{\partial^2 \psi}{\partial \gamma^2} + \frac{1}{\gamma^2} \frac{\partial^2 \psi}{\partial \phi^2} = 0 \, , \tag{3.25a}$$

where

$$\tau'(\gamma) = \frac{d\tau}{d\gamma} = \Sigma\left(\gamma^2\right) + 2\gamma^2 \frac{d\Sigma}{d\gamma^2} \, . \tag{3.25b}$$

In strain coordinates, the boundary condition (3.22) is

$$\partial \psi / \partial \gamma_2 = 0 \quad \text{and} \quad \partial \psi / \partial \gamma_1 < 0 \quad \text{at} \quad \gamma_2 = 0 \, . \tag{3.26}$$

The condition $\partial \psi / \partial \gamma_1 < 0$ is included in (3.26) since the undeformed crack lies on the negative x_1 axis ($x_1 = \partial \psi / \partial \gamma_1 < 0$). Equations (3.25a,b) and (3.26) completely determine the leading order behavior of y_2. Note that (3.25a) is valid for *any* smooth work function *U*(*I*); this feature allows us to study the crack tip fields for a much wider class of work functions. Once the leading behavior of y_2 is found, the leading behavior of y_1 can be deduced by solving (3.13a) and (3.14a). In the following, we demonstrate this method using GNH and an exponential hardening model.

3.4 Asymptotic Crack Tip Fields in Generalized neo-Hookean (GNH) Materials

We first give a brief review of GK's analysis. They sought a separable solution of the form:

$$y_\alpha(r \to 0, \theta) \approx r^{p_\alpha} v_\alpha\left(\theta\right) \qquad \alpha = 1, 2 \tag{3.27}$$

with the condition that $1 > p_1 > p_2 > 0$ to ensure a smooth crack opening profile. Note (3.16b) is a generalization of this condition. Substituting (3.27) into (3.13a,b) and neglecting higher order terms, GK reduced these PDEs into two coupled nonlinear ordinary differential equations (ODE) for the unknown angular functions $v_\alpha(\theta)$ in (3.27). The unknown power exponents p_α were determined by requiring $v_\alpha(\theta)$ to satisfy the traction free boundary conditions (3.14a,b). GK showed that

$$p_2 = 1 - \frac{1}{2n}, \qquad n > 1/2 . \tag{3.28}$$

The angular function v_2 can be obtained in closed form using a method introduced by Knowles and Sternberg [7]. The other unknowns p_1 and $v_1(\theta)$ were determined by numerically solving a boundary value problem associated with a second order nonlinear ODE. To solve for p_1 and $v_1(\theta)$, GK assumed that

$$y_{1,1} >> \lambda^3 y_{2,2} \quad \text{and} \quad y_{1,2} >> \lambda^3 y_{2,1} \ . \tag{3.29}$$

These assumptions allow GK to neglect certain higher order terms in (3.13b) which simplifies their analysis. *However, GK found in their numerical solution that, when* $n > n^* \approx 1.4$*, the conditions in (3.29) are violated.* In their words, "the separable form (3.27) of near tip solution is not expected to be applicable."

3.4.1 Leading behavior of y_2

In this section, we use the method derived in section 3.3 to obtain the leading order solution for *all* $n > 1/2$. Using the elastic energy density function given in (3.1) and (3.19b,c), we found

$$\tau(\gamma) = \mu\gamma\left(1 + \frac{b}{n}\left(\gamma^2 - 3\right)\right)^{n-1} \ . \tag{3.30}$$

Substituting (3.30) into (3.25a), the governing equation for the function ψ becomes

$$\frac{n-3b+b\gamma^2}{n-3b+(2n-1)b\gamma^2}\frac{\partial^2\psi}{\partial\gamma^2}+\frac{1}{\gamma}\frac{\partial\psi}{\partial\gamma}+\frac{1}{\gamma^2}\frac{\partial^2\psi}{\partial\phi^2}=0 \quad . \tag{3.31}$$

The leading order behavior of (3.31) as $\gamma\to\infty$ can be obtained by solving

$$\frac{1}{2n-1}\frac{\partial^2\psi}{\partial\gamma^2}+\frac{1}{\gamma}\frac{\partial\psi}{\partial\gamma}+\frac{1}{\gamma^2}\frac{\partial^2\psi}{\partial\phi^2}=0\,. \tag{3.32}$$

The linear PDE (3.32) has a separable solution:

$$\psi=h(\gamma)t(\phi)\,. \tag{3.33}$$

The boundary conditions (26) imply that

$$\left.\frac{dt}{d\phi}\right|_{\phi=\pm\pi/2}=0 \quad \text{and} \quad t(\pi/2)=-t(-\pi/2) \quad . \tag{3.34}$$

Substituting (33) into (32) results in two linear ODEs:

$$\frac{\left(\frac{1}{2n-1}\right)\gamma^2\frac{d^2h}{d\gamma^2}+\gamma\frac{dh}{d\gamma}}{h}=\eta\,, \tag{3.35a}$$

$$-\frac{\frac{d^2t}{d\phi^2}}{t}=\eta\,, \tag{3.35b}$$

where η is a constant which must be non-negative for otherwise the boundary condition (3.34) cannot be satisfied by a non-trivial *t*. Solutions of (3.35b) subject to (3.34) are

$$t(\phi)=C\sin\sqrt{\eta}\phi \quad (\sqrt{\eta}=1,3,5...)\,. \tag{3.36}$$

where C is an unknown constant. The solution of (3.35a) is

$$h(\gamma)=\gamma^m \quad , \tag{3.37a}$$

where

$$m=-(n-1)\pm\sqrt{(n-1)^2+(2n-1)\eta}\,. \tag{3.37b}$$

Equation (3.24b) and the fact that $\gamma \to \infty$ as the crack tip is approached imply that

$$r = \sqrt{x_1^2 + x_2^2} = \sqrt{\left(\frac{\partial \psi}{\partial \gamma}\right)^2 + \frac{1}{\gamma^2}\left(\frac{\partial \psi}{\partial \phi}\right)^2} \to 0 \quad \text{as} \quad \gamma \to \infty . \tag{3.38a}$$

Substituting (3.33) and (3.37a) into (3.38a), we obtain

$$r \sim \gamma^{m-1} \qquad \text{or} \qquad \gamma \sim r^{\frac{1}{m-1}} . \tag{3.38b}$$

Since we are seeking the leading order behavior of the strain field, the exponent *m-1* in (3.38b) should be negative and has the minimum absolute value. This condition requires us to pick the negative sign in (3.37b) and $\eta = 1$, which results in

$$m = -(2n-1) . \tag{3.39}$$

Using (3.36), (3.37a) and (3.39), the leading order behavior of the function ψ is

$$\psi \approx C_1 \gamma^{-(2n-1)} \sin\phi , \tag{3.40}$$

where C_1 is a constant coefficient. The leading order behavior of γ, using (3.40) and (3.38a), is

$$\gamma \approx \left(|C_1|/r\right)^{1/(2n)} \left[(2n-1)^2 \sin^2\phi + \cos^2\phi\right]^{1/4n} . \tag{3.41}$$

The leading order behavior of y_2 can be found using (3.19c), (3.24a) and (3.41). The result, expressed in the physical plane, is

$$y_2 = A r^{1-1/2n} f(\theta; n) , \tag{3.42a}$$

where

$$f(\theta; n) = \left[n(w + k\cos\theta)\right]^{\frac{n-1}{2n}} \sin\frac{\theta}{2}\left[1 - \frac{2k^2\cos^2(\theta/2)}{1+w}\right]^{1/2} , \tag{3.42b}$$

$$k = 1 - n^{-1} \quad \text{and} \quad w = \sqrt{1 - k^2\sin^2\theta} . \tag{3.42c}$$

In (3.42a), *A* is a constant which cannot be determined by asymptotic analysis. It characterizes the strength of the crack tip fields and its value depends on the specimen

geometry and the loading conditions. Detailed derivation of (3.42a,b) is given in Appendix 3.1. Equations (3.42a-c) are identical to the results given in GK. As pointed out by GK, this leading order behavior for y_2 is valid for *all* $n > 1/2$.

3.4.2 Leading behavior of y_1

The harder question is finding the leading order behavior of y_1, which requires us to solve the equilibrium equation $S_{11,1} + S_{12,2} = 0$. Equation (3.12) implies that the leading order behavior of $S_{1\beta}$ must be determined by one of the following three possibilities:

Case 1: $|y_{1,1}| << |\lambda^3 y_{2,2}|$ and $|y_{1,2}| << |\lambda^3 y_{2,1}|$; (3.43a)

Case 2: $|y_{1,1}| >> |\lambda^3 y_{2,2}|$ and $|y_{1,2}| >> |\lambda^3 y_{2,1}|$; (3.43b)

Case 3: $|y_{1,1}| \sim |\lambda^3 y_{2,2}|$ and $|y_{1,2}| \sim |\lambda^3 y_{2,1}|$. (3.43c)

Case 1 can be ruled out since the traction free boundary condition cannot be satisfied. This is because the leading behavior of S_{12} is

$$S_{12} \approx 2\frac{dU}{dI}\lambda^3 y_{2,1} . \tag{3.44}$$

Since $2\lambda^3 dU/dI \neq 0$, (3.44) implies that the traction free boundary condition, $S_{12}(r, \theta = \pm\pi) = 0$, can be satisfied only if

$$y_{2,1}(r, \theta = \pm\pi) = 0 . \tag{3.45}$$

However, (3.45) is unphysical, since the crack face is expected to open non-uniformly. In addition, (3.45) is inconsistent with the solution of y_2 obtained earlier (see (3.42)).

Case 2 was considered by GK. Specifically, we can reproduce their result if we assume y_1 has a separable solution of the form

$$y_1 = Br^c q(\theta; n) , \tag{3.46}$$

where *B* is a constant which is assumed to be *independent* of *A* (see (3.42a)). This assumption allows *GK* to enforce the normalization condition $q(0; n) = 1$.

Substituting (3.42a) and (3.46) into (3.10), we found $\lambda \sim r^{1-c+1/2n}$. This means Case 2 or (3.43b) is satisfied if

$$c < 1 + \frac{1}{4n}. \tag{3.47}$$

Using (3.42a), (3.43b) and (3.46), the leading order behavior of the equilibrium equation $S_{11,1} + S_{12,2} = 0$ (see (3.12)) reduces to the following ODE for $q(\theta, n)$:

$$\frac{d^2 q}{d\theta^2} + \frac{(n-1)^2 \sin\theta}{n\sqrt{n^2 - (n-1)^2 \sin^2\theta}} \frac{dq}{d\theta} + \left(\frac{c}{n} - c + c^2 \right) q = 0. \tag{3.48a}$$

The traction free boundary condition (3.6) requires

$$q'(\pi) = 0. \tag{3.48b}$$

Since $q(\theta)$ is an even function, we also have

$$q'(0) = 0. \tag{3.48c}$$

Equations (3.48a,b,c) together with the normalization condition, $q(0) = 1$, can be solved numerically with c as an eigenvalue. Numerical solutions of c and $q(\theta)$ were determined by GK (referred to as p and $g(\theta)$, see Figure 6 and Figure 7 in [11]). They also obtained approximate closed form solutions of c and $q(\theta)$ using WKB method (see Appendix in [11]). *They found numerically that the condition imposed by (3.47) can not be satisfied for* $n > n^* \approx 1.4$.

The analysis above shows that Case 3 is the only choice when $n > n^*$. If we assume a separable solution for y_1 as in (3.46), then c can be determined using (3.43c), i.e.,

$$c = 1 + \frac{1}{4n} \tag{3.49a}$$

and

$$y_1 = B r^{1+\frac{1}{4n}} g(\theta; n). \tag{3.49b}$$

In (3.49b), we use a different notation for the angular variation of y_1 (g instead of q,

see (3.46)), since g is found to satisfy a different ODE. The equilibrium equation $S_{11,1} + S_{12,2} = 0$ is

$$\left(2\frac{dU}{dI}(y_{1,1} - \lambda^3 y_{2,2})\right)_{,1} + \left(2\frac{dU}{dI}(y_{1,2} + \lambda^3 y_{2,1})\right)_{,2} = 0 \quad . \tag{3.50}$$

Substituting (42a-c), (49b) into (50), we obtain the following complicated nonlinear ODE for $g(\theta; n)$.

$$\left(\xi^4 + 3\left(1-\frac{1}{2n}\right)^2 f^2\right)g'' = -\frac{5}{4n}\left(1+\frac{1}{4n}\right)g\xi^4 + \left(\frac{7}{4n}-1\right)f'\xi$$
$$+\frac{3}{4n}\left(1-\frac{1}{2n}\right)f\left(3f'g' + (4n+1)f''g\right) - (n-1)\frac{2\left(1-\frac{1}{2n}\right)^2 ff' + 2ff''}{\left(1-\frac{1}{2n}\right)^2 (f)^2 + (f')^2}\left(g'\xi^4 + \left(1-\frac{1}{2n}\right)f\xi\right) \quad , \tag{3.51}$$

where

$$\xi = \left(1+\frac{1}{4n}\right)f'g - \left(1-\frac{1}{2n}\right)fg' \quad . \tag{3.52a}$$

The prime denotes derivative with respect to θ and f is given by (3.42b). Detailed derivation of (3.51) is given in Appendix 3.2. The boundary conditions are

$$g'(\theta = 0) = 0\,, \tag{3.52b}$$

$$g'(\theta = \pi) = -\sqrt{\frac{2n}{2n-1}} \quad . \tag{3.52c}$$

Equation (3.52b) states that g is an even function of θ (see (3.15)) whereas (3.52c) is the leading order expansion of the traction free condition (3.14a). Derivation of (3.52c) is also given in Appendix 3.2. In contrast to Case 2 or $n < n^*$, *we cannot apply normalization condition such as* $g(\theta = 0) = 1$ *since we have used the condition that* $B^4 = A^{-2}$ *in the derivation of (3.51) (see Appendix 3.2), so that there is no loss of generality.* Equations (3.51) and (3.52b,c) was solved numerically using a shooting

method in the interval $\theta \in [0, \pi]$. The solution can be extended to the domain $[-\pi, \pi]$ using the symmetry of $g(\theta; n)$. Examples of $g(\theta; n)$ for different *n* are shown in Figure 3.2.

We can not find any numerical solution of $g(\theta; n)$ *when* $n < 1.46$. Due to the complicated nonlinear nature of (3.51), we are unable to provide a rigorous proof of this result. However, this result is consistent with GK's finding. As mentioned earlier, GK discovered numerically that their result (Case 2, (3.46)) breaks down for $n > n^*$; n^* was found to be approximately 1.4. Our numerical result suggested the slightly higher value of $n^* \approx 1.46$. The important result we have discovered is that there is a *bifurcation of asymptotic results* at $n = n^*$. Specifically, below n^*, y_1 is determined by (3.46); for $n > n^*$, y_1 is given by (3.49b).

3.4.3 Asymptotic Stress Fields

The asymptotic solutions of y_α allow us to compute the stress field near the crack tip for any $n > 1/2$. The leading order behavior of S_{21} and S_{22} can be found using (3.12) and (3.42a-c):

$$S_{21} = \frac{\Lambda}{2} r^{-1+\frac{1}{2n}} \left[n\left(w + k\cos\theta\right) \right]^{-(n-1)/(2n)} \left[\sqrt{2n-1}\cos\theta \sin\frac{\theta}{2} \left(1 - \frac{2k^2 \cos^2(\theta/2)}{1+w} \right)^{1/2} - \frac{1}{\sqrt{2}} \sin\theta \sqrt{w + \cos\theta} \right] \tag{3.53a}$$

$$S_{22} = \frac{\Lambda}{2} r^{-1+\frac{1}{2n}} \left[n\left(w + k\cos\theta\right) \right]^{-(n-1)/(2n)} \left[\sqrt{2n-1}\sin\theta \sin\frac{\theta}{2} \left(1 - \frac{2k^2 \cos^2(\theta/2)}{1+w} \right)^{1/2} + \frac{1}{\sqrt{2}} \cos\theta \sqrt{w + \cos\theta} \right] \tag{3.53b}$$

where

$$\Lambda = \mu \left(\frac{b(2n-1)^2}{4n^3} \right)^{n-1} A^{2n-1} \frac{\sqrt{2n-1}}{n}. \tag{3.53c}$$

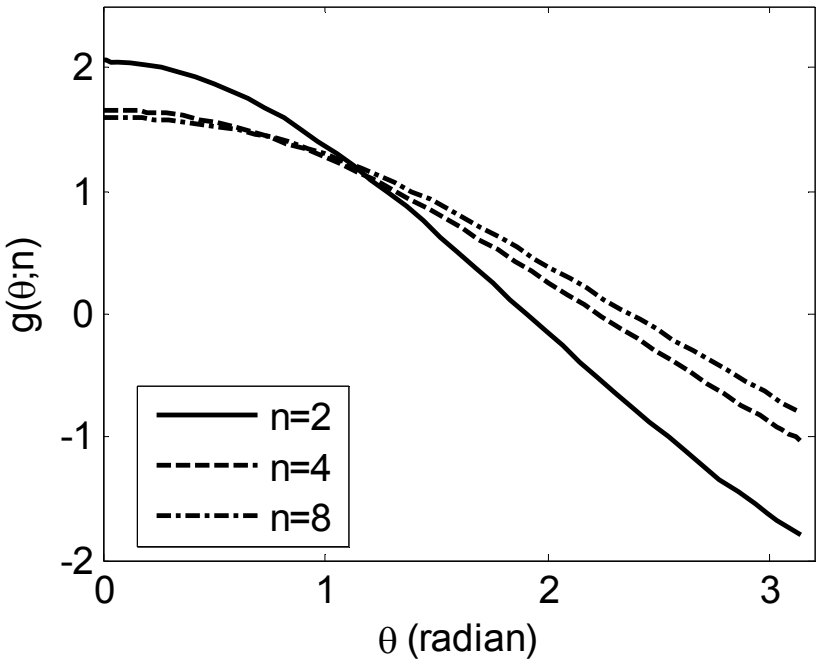

Figure 3.2 Numerical solutions of $g(\theta;n)$ for *n = 2, 4, 8*.

Recall A is the undetermined constant in y_2 (see (3.42a)) and w and k are given in (3.42c).

Since the solution of y_1 bifurcates at $n = n^*$, so do S_{11} and S_{12}. For $n < n^*$, the leading order terms of S_{11} and S_{12} can be found using (3.12), (3.42a-c) and (3.46):

$$S_{11} = Br^{c-2+1/n}\Phi(\theta)\left(cq(\theta)\cos\theta - q'(\theta)\sin\theta\right), \tag{3.54a}$$

$$S_{12} = Br^{c-2+1/n}\Phi(\theta)\left(cq(\theta)\sin\theta + q'(\theta)\cos\theta\right), \tag{3.54b}$$

where

$$\Phi(\theta) = \mu\left(\frac{b(2n-1)^2}{4n^3}\right)^{n-1} A^{2n-2}\left[n\left(w + k\cos\theta\right)\right]^{-(n-1)/n}. \tag{3.54c}$$

In (3.54a,b), c and $q(\theta)$ are solutions of (3.48a-c) and B is a constant coefficient in y_1 (see (3.46)). The unknown constants A and B *are independent and* can not be determined by asymptotic analysis since they depend on the specimen geometry and the applied load.

For $n > n^*$, S_{11} and S_{12} can be found using (3.12), (3.42a-c) and (3.49):

$$S_{11} = Br^{-1+\frac{5}{4n}}\Phi(\theta)K(\theta) \quad , \tag{3.55a}$$

$$S_{12} = Br^{-1+\frac{5}{4n}}\Phi(\theta)L(\theta) \quad , \tag{3.55b}$$

where $K(\theta)$ and $L(\theta)$ are defined in Appendix 3.2 (see (A3.20)). Note, for this case, *B is determined by $B^4 = A^{-2}$. In other words, the strength of the asymptotic fields $S_{1\alpha}$ is completely determined by the strength of $S_{2\alpha}$.*

In practice, the stress measure of interest is the true stress or Cauchy stress. For incompressible materials, the Cauchy stress tensor $\mathbf{T}$ is related to the first Piola-Kirchhoff tensor $\mathbf{S}$ by

$$\mathbf{T} = \mathbf{S}\mathbf{F}^T \tag{3.56}$$

where $\mathbf{F}$ is the deformation gradient tensor (see (3.3)). We use (3.56) to derive true

stresses. The results are summarized here. For $n < n^*$, the true stress components T_{11} and T_{12} $(= T_{21})$ are

$$T_{11} = B^2 r^{2c-3+1/n} \Phi(\theta) \left[c^2 q^2(\theta) + \left(q'(\theta) \right)^2 \right] \tag{3.57a}$$

$$T_{12} = ABr^{c-2+\frac{1}{2n}} \Phi(\theta) \left[\left(1 - \frac{1}{2n} \right) cf(\theta) q(\theta) + f'(\theta) q'(\theta) \right], \tag{3.57b}$$

where $f(\theta)$ is given by (3.42b).

The true stress components T_{11} and T_{12} $(= T_{21})$ for $n > n^*$ are

$$T_{11} = B^2 r^{-1+\frac{3}{2n}} \Phi(\theta) \left[\left(1 + \frac{1}{4n} \right)^2 g^2 + (g')^2 + \frac{2(2n-1) fg' - (4n+1) f'g}{4n\xi^3} \right], \tag{3.57c}$$

$$T_{12} = ABr^{-1+\frac{3}{4n}} \Phi(\theta) \left[\left(1 + \frac{1}{4n} \right) \left(1 - \frac{1}{2n} \right) fg + f'g' \right]. \tag{3.57d}$$

Note that ξ in (3.57c) is defined in (3.52a) and $g(\theta)$ is the solution of (3.51) subjected to (3.52b,c).

For *all* $n > 1/2$, the opening true stress component T_{22} is

$$T_{22} = \mu \left(\frac{b}{n} \right)^{n-1} \left(A \frac{2n-1}{2n} \right)^{2n} \frac{1}{r} \frac{1}{(n-1)\cos\theta + \sqrt{n^2 - (n-1)^2 \sin^2\theta}} \quad . \tag{3.57e}$$

It is interesting to note that $T_{22} \sim 1/r$ for *all* $n > 1/2$. In particular, the opening component of the true stress, T_{22}, is asymptotically dominant as one approaches the crack tip, that is, $T_{11}/T_{22} \to 0$, $T_{12}/T_{22} \to 0$ as $r \to 0$. In other words, *every material element near the crack tip is under uniaxial tension.*

3.4.4 FEM Simulation

We carried out FEM simulations using ABAQUS to check our asymptotic analysis. We focus on $n > n^*$ here since the solutions for $n < n^*$ have been verified by GK

using FEM [11]. The geometry of our FEM model is shown in Figure 3.3a. A crack of length 2.5a is located at the left edge of a $10a \times 2a$ strip of height $2a$. A uniform vertical displacement of Δ is applied to the top and bottom boundaries of the strip (Figure 3.3a). The horizontal displacements on these boundaries are fixed to be zero. We set $\Delta = a$ to simulate large deformation. To resolve the singular fields, our minimum mesh size near the crack tip is on the order of $10^{-5} a$. We used a sub-modeling technique similar to Krishnan *et al.* [24] to increase accuracy. To verify our asymptotic solution of y_1 and y_2, we extract the displacements u_α of material points along four curves in the undeformed configuration. These curves are indicated by dashed lines in Figure 3.3b. Specifically, they are: a small circle, $r_o = 2 \times 10^{-4} a$; a large circle, $r_o = 4 \times 10^{-4} a$; a line directly ahead of the crack tip, $\theta = 0$ (0-line); and a tilted line $\theta = \pi / 4$ (45-line). Recall (r, θ) are the polar coordinates of a material point in the undeformed reference configuration. Equation (3.2) is used to evaluate y_α from FEM solutions of u_α. We compare these FEM results on the small circle and large circle with the angular variations of y_α determined using asymptotics, i.e., $f(\theta; n)$ and $g(\theta; n)$. FEM results of y_α along the two straight paths were used to check the radial dependence of y_α. For example, according to our solution, when $n = 2$, $y_1 \sim r^{1.125}$ and $y_2 \sim r^{0.75}$. These scaling relations should be predicted by the FEM results, if our analysis is correct.

Figure 3.4 plots the variation of y_1 and y_2 for $n = 2, 4$ along the two circular paths (see Figure 3.3b). Since $f(\theta)$ satisfies the normalization condition $f(\pi) = 1$, we have, by (3.42a),

$$f(\theta) = y_2(r = r_o, \theta) / y_2(r = r_o, \theta = \pi) \quad . \tag{3.58a}$$

Likewise, (3.49b) implies that

$$g(\theta) / g(\theta = 0) = y_1(r = r_o, \theta) / y_1(r = r_o, \theta = 0) . \tag{3.58b}$$

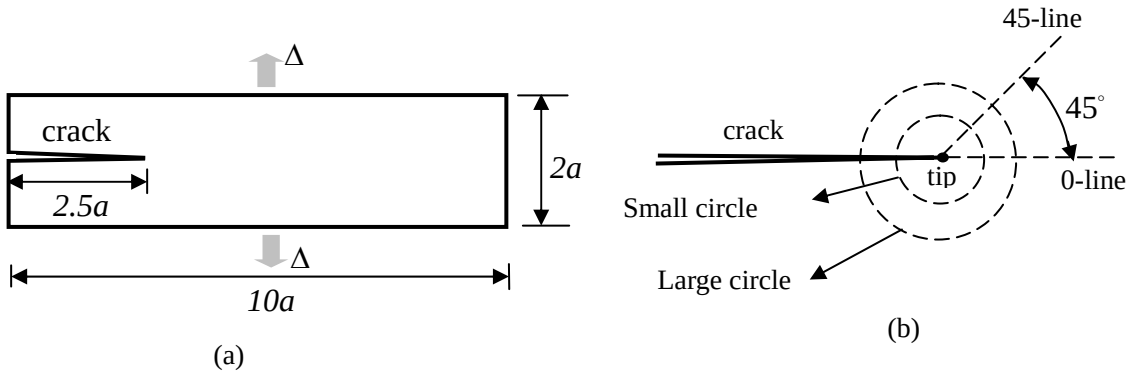

Figure 3.3 (a) Geometry of FEM model: a thin rectangular strip with an edge crack. A vertical displacement of Δ is applied at the top and bottom boundaries. (b) We obtain the displacements of material points on four dashed curves in the undeformed configuration: small circle with radius of $2\times10^{-4}a$, large circle with radius of $4\times10^{-4}a$, 0-line directly ahead of the crack tip and 45-line that is tilted for 45 degrees from the 0-line.

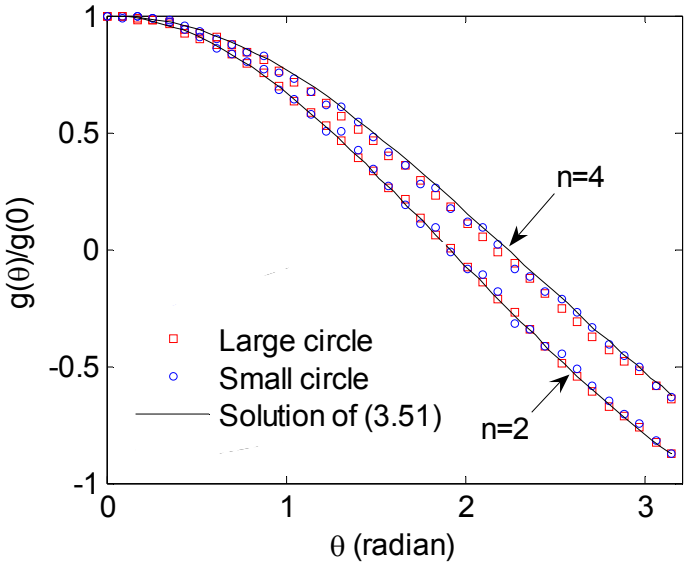

(a)

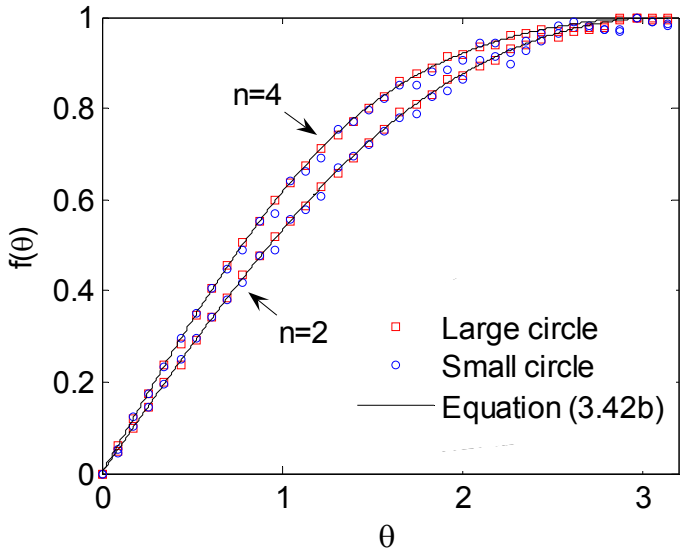

(b)

Figure 3.4 (a) Angular variation of y_1 or $g(\theta)/g(0)$ for $n=2$ and 4. Symbols are FEM results; solid line is solution of (3.51) subjected to (3.52b,c). (b) Angular variation of y_2 or $f(\theta)$ for $n=2$ and 4. Symbols are FEM results and the solid line is (3.42b).

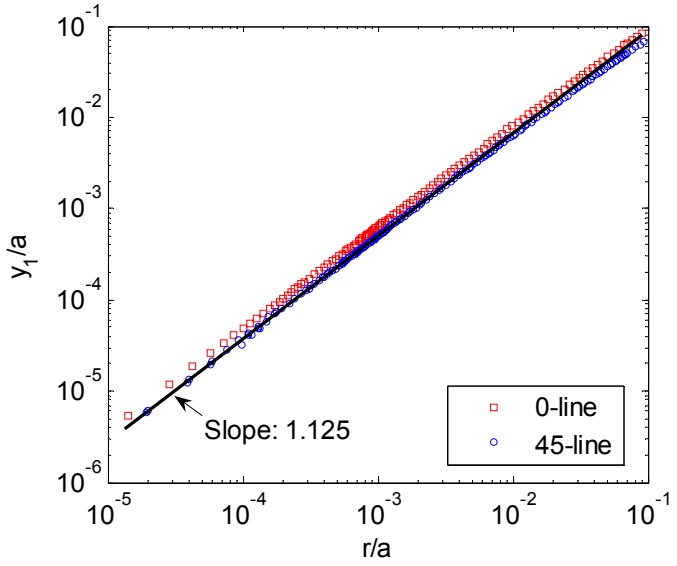

(a)

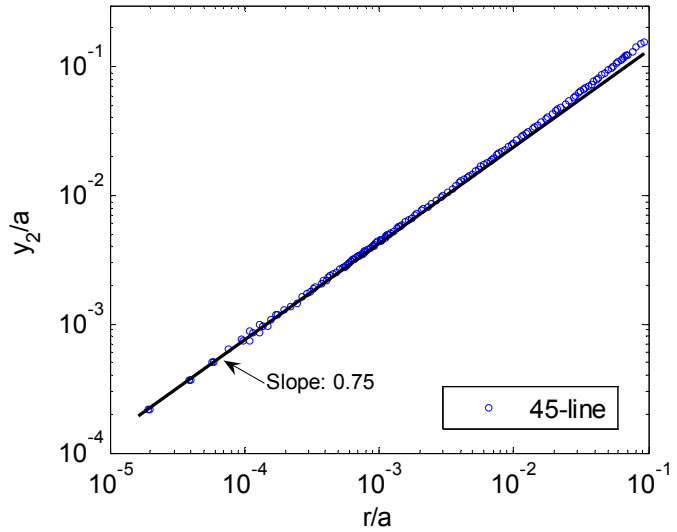

(b)

Figure 3.5 (a) Radial variation of y_1 along the 0-line and 45-line (see Figure 3.3b) on a log-log plot. The solid line serves as a reference and has a slope of 1.125. (b) Radial variation of y_2 along the 45-line indicated in Figure 3.3b on a log-log plot. Note y_2 is identically zero along the 0-line. The reference solid line has a slope of 0.75.

Recall $r_o = 2\times10^{-4}a$ for the small circle and $r_o = 4\times10^{-4}a$ for the large circle. The left hand sides of (3.58a,b) have been determined by our theory, while the right hand side of (3.58a,b) can be obtained using FEM. It is clear from Figure 3.4 that our asymptotic results for $g(\theta)/g(\theta=0)$ and $f(\theta)$ agree very well with the predictions of FEM. Furthermore, the FEM data using small circle and large circle yields the same curve for both $g(\theta)/g(\theta=0)$ and $f(\theta)$. This result supports our asymptotic results that y_1 and y_2 are separable functions of r and θ.

Log-log plots of y_1 and y_2 versus r/a along the 0-line and 45-line for *n=2* are shown in Figure 3.5. For *n=2*, our asymptotic results show that

$$y_1 \sim r^{1.125} \quad \text{and} \quad y_2 \sim r^{0.75} \quad \text{for} \quad n=2. \tag{3.59}$$

Equation (3.59) implies that the slopes of y_1 and y_2 on log-log plots should be 1.125 and 0.75, respectively. This result is confirmed by Fig.5a and 5b. Note, in Figure 3.5a, the FEM results on the 0-line and 45-line are parallel, which also confirms the validity of the separable solution.

We also checked our asymptotic solution with FEM results for cases where $n < n^*$ using the same procedure. Since GK have performed FEM calculations for these cases, we do not present the results.

3.5 Asymptotic crack tip fields in an exponentially hardening solid

Seitz *et al* [20] found that the experimental data of their uniaxial compression tests on acrylic triblock copolymers can be fitted very well using an exponentially hardening material model. This model was also used to fit polyurethane elastomers in cavitation experiments [25]. The work function of this model is

$$U = \frac{\mu J_m}{2}\left[\exp\left(\frac{I-3}{J_m}\right)-1\right], \tag{3.60}$$

where μ is the small strain shear modulus and J_m is a material constant that measures the degree of strain hardening. Larger J_m implies less strain hardening. Note that (3.60) approaches the neo-Hookean model as $J_m \to \infty$. The exponentially hardening model is able to capture the finite extensibility of gels and rubbers by rapidly increasing U once $I-3 > J_m$. It is also interesting to note that the limit of GNH's work function (see (3.1)) as $n \to \infty$ is (3.60).

3.5.1 Leading behavior of y_2

In this section we determine the leading order behavior of y_2 under Mode-I loading assuming that the work function is given by (3.60). The analysis follows the procedure outlined in section 3.3. Briefly, using (3.12), (3.60) and the equilibrium equation $S_{21,1} + S_{22,2} = 0$, we find

$$\frac{I_{,1}}{J_m}\left(y_{2,1} + \lambda^3 y_{1,2}\right) + \left(y_{2,1} + \lambda^3 y_{1,2}\right)_{,1} + \frac{I_{,2}}{J_m}\left(y_{2,2} - \lambda^3 y_{1,1}\right) + \left(y_{2,2} - \lambda^3 y_{1,1}\right)_{,2} = 0 . \qquad (3.61a)$$

Using (3.17) and (3.18), the leading order behavior of (3.61a) is governed by

$$\left(\frac{\gamma^2}{J_m}\right)_{,1} y_{2,1} + y_{2,11} + \left(\frac{\gamma^2}{J_m}\right)_{,2} y_{2,2} + y_{2,22} = 0 , \qquad (3.61b)$$

where γ is given by (3.19c). Equation (3.61b) is equivalent to

$$\left[\exp\left(\frac{\gamma^2}{J_m}\right) y_{2,1}\right]_{,1} + \left[\exp\left(\frac{\gamma^2}{J_m}\right) y_{2,2}\right]_{,2} = 0 . \qquad (3.61c)$$

Using (3.25a,b) with $\Sigma\left(\gamma^2\right) = \exp\left(\gamma^2 / J_m\right)$, we obtain the differential equation for the function ψ,

$$\left[1 + \frac{2\gamma^2}{J_m}\right]^{-1} \frac{\partial^2 \psi}{\partial \gamma^2} + \frac{1}{\gamma}\frac{\partial \psi}{\partial \gamma} + \frac{1}{\gamma^2}\frac{\partial^2 \psi}{\partial \phi^2} = 0 . \qquad (3.61d)$$

where γ and ϕ are the polar coordinates in the strain plane (see (3.24a)). The traction

free boundary condition is still given by (3.26).

It is convenient to normalize γ by $\sqrt{J_m/2}$, i.e.,

$$\rho = \gamma / \sqrt{J_m/2}\,. \tag{3.62}$$

Using (3.62), (3.61d) becomes

$$\left[1+\rho^2\right]^{-1} \frac{\partial^2 \psi}{\partial \rho^2} + \rho^{-1} \frac{\partial \psi}{\partial \rho} + \rho^{-2} \frac{\partial^2 \psi}{\partial \phi^2} = 0 \quad . \tag{3.63a}$$

As in section 3.4.1, we seek a solution of the form

$$\psi = z(\rho) l(\phi)\,. \tag{3.63b}$$

Substituting (3.63b) into (3.63a) gives

$$\left[1+\rho^2\right]^{-1} \rho^2 \frac{d^2 z}{z d\rho^2} + \rho \frac{dz}{z d\rho} = -\frac{d^2 l}{l d\phi^2} = \chi\,, \tag{3.64}$$

where χ is a constant. As in the case of GNH material, the non-trivial solutions of $l(\phi)$ subjected to the boundary condition (3.26) is

$$l(\phi) = C_2 \sin\sqrt{\chi}\phi \quad (\sqrt{\chi}=1,3,5...)\,, \tag{3.65}$$

where C_2 is an integration constant. In Appendix 3.3, we show that the asymptotic behavior of $z(\rho)$ as $\rho \to \infty$ is given by

$$z(\rho) \approx \frac{C_3 e^{-\rho^2/2}}{\rho^{\chi+2}} \qquad \rho \to \infty\,, \tag{3.66}$$

where C_3 is an integration constant. As in the GNH case (see (3.38a)), the leading order behavior of y_2 is determined by the value of χ such that $z(\rho)$ approaches zero at the slowest rate as $\rho \to \infty$. Equation (3.66) shows that this condition requires χ to be minimized, i.e., $\chi = 1$ in (3.65) and (3.66). The function ψ is obtained by combining (3.62), (3.63b), (3.65) and (3.66), which results in

$$\psi = -A_2 \frac{e^{-\gamma^2/J_m}}{\gamma^3} \sin\phi \qquad \text{as} \quad \gamma \to \infty , \tag{3.67}$$

where A_2 is a constant which depends on the external loading and specimen geometry. The physical coordinates (x_1, x_2) can be determined using (3.24b) and (3.67), i.e.,

$$x_1 = -\frac{A_2 e^{-\gamma^2/J_m}}{\gamma^2}\left(\frac{2}{J_m}\sin^2\phi - \frac{1}{\gamma^2}\cos^2\phi\right) \qquad \text{as} \quad \gamma \to \infty \ , \tag{3.68a}$$

$$x_2 = \frac{A_2 e^{-\gamma^2/J_m}}{\gamma^2}\frac{2}{J_m}\sin\phi\cos\phi \qquad \text{as} \quad \gamma \to \infty \ . \tag{3.68b}$$

To obtain (3.68a,b), we neglected all higher order terms except the term $\cos^2\phi/\gamma^2$ on the right hand side of (3.68a). This term is retained since it becomes dominant at $\phi = 0$, that is, the $\sin^2\phi$ term in (3.68a) vanishes at $\phi = 0$. Note that $\phi = \pm\pi/2$ on the crack face where $x_1 < 0$, this fact, together with (3.68a), implies that $A_2 > 0$. Using (3.68a,b), (r,θ) is related to (γ,ϕ) by

$$r = \frac{A_2 e^{-\gamma^2/J_m}}{\gamma^2}\sqrt{\left(\frac{2}{J_m}\right)^2 \sin^2\phi + \frac{1}{\gamma^4}\cos^2\phi} , \tag{3.69a}$$

$$\tan\theta = \frac{-\sin\phi\cos\phi}{\sin^2\phi - (J_m/2)\gamma^{-2}\cos^2\phi} \ . \tag{3.69b}$$

Equation (3.69a) implies that the leading behavior of γ is

$$\gamma = \sqrt{-J_m \ln\left(\frac{r}{A_2}\right)} \qquad \text{as} \quad r \to 0 . \tag{3.70}$$

The relation between θ and ϕ can be found by solving (3.69b) numerically. However, this relation is complicated by the fact that $\sin^2\phi$ vanishes at $\phi = 0$; this means that θ depends not only on ϕ but also on γ. As a result, y_2 is *not separable* in r and θ. In the following, we present an *approximate* relation between θ and ϕ that is independent of γ. For $|\phi| >> \sqrt{J_m/2\gamma^2}$, (3.69b) reduces to

$$\tan\theta = \frac{x_2}{x_1} \approx -\cot\phi\,, \tag{3.71a}$$

i.e.,

$$\theta = \phi \pm \frac{\pi}{2}\,. \tag{3.71b}$$

Note that (3.71b) is not uniformly valid for all $\phi \in [-\pi/2, \pi/2]$; there is a boundary layer at $\phi = 0$. For example, in the region where $|\phi| << \sqrt{J_m / 2\gamma^2}$,

$$\tan\theta = \frac{x_2}{x_1} \approx \frac{2\gamma^2}{J_m}\tan\phi\,. \tag{3.72}$$

Figure 3.6 plots θ versus ϕ using (3.69b) for two different values of $J_m / 2\gamma^2$. It shows that as $\gamma \to \infty$ or $J_m / 2\gamma^2 \to 0$, θ increases rapidly from 0 to $\pi/2$ near the origin, after this $\theta = \phi + \pi/2$. For $\gamma >> 1$, a first order approximation of ϕ is

$$\phi = \begin{cases} \theta - \pi/2 & \theta \in [\pi/2, \pi] \\ 0 & \theta \in (-\pi/2, \pi/2) \\ \theta + \pi/2 & \theta \in [-\pi, -\pi/2] \end{cases} \tag{3.73}$$

Figure 3.6 shows that (3.73) is valid for small $J_m / 2\gamma^2$, however, it should be noted that (3.73) is accurate only for extremely small *r*, given the weak logarithmic singularity of γ.

Equation (3.73) suggests dividing the region surrounding the crack tip into three sectors (see inset of Figure 3.6). In Region I, $\theta \in [\pi/2, \pi]$, the spatial gradient of y_2 can be determined using (3.24a), (3.70) and (3.73), i.e.,

$$y_{2,1} \approx \sqrt{-J_m \ln\left(\frac{r}{A_2}\right)}\cos\theta\,, \quad y_{2,2} \approx \sqrt{-J_m \ln\left(\frac{r}{A_2}\right)}\sin\theta \quad \text{as} \quad \gamma \to \infty\,. \tag{3.74}$$

Integrating (3.74) and retaining only the first order terms, we found

$$y_2 \approx r\sqrt{-J_m \ln\left(\frac{r}{A_2}\right)} \qquad \theta \in [\pi/2, \pi]\,, \tag{3.75}$$

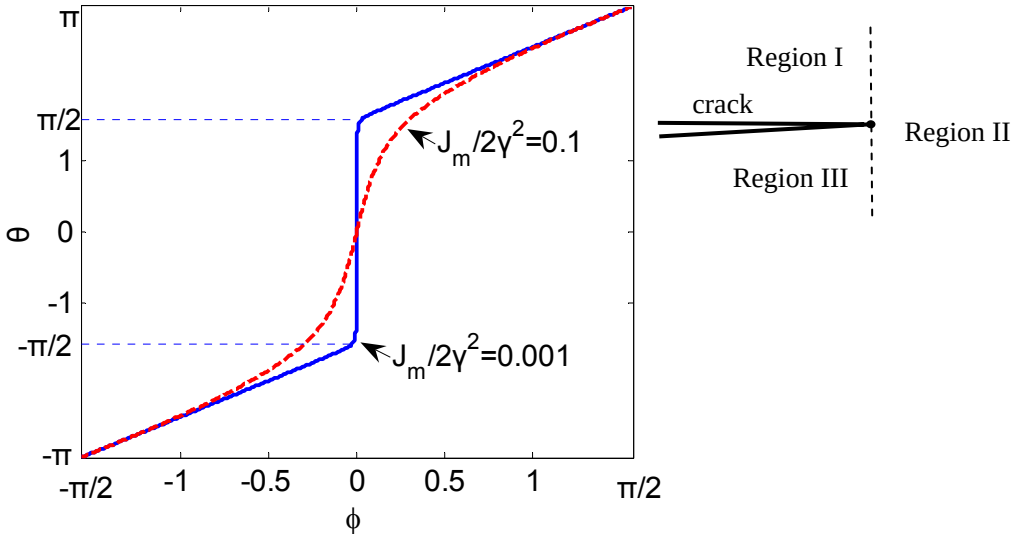

Figure 3.6 The polar angle θ of the physical plane versus the polar angle ϕ of the strain plane given by (3.69b) for $J_m / 2\gamma^2$ =0.1 and 0.001. The solid line for the case $J_m / 2\gamma^2 = 10^{-3}$ is practically indistinguishable from (3.73). Inset shows Region I, Region II, Region III in the reference undeformed configuration.

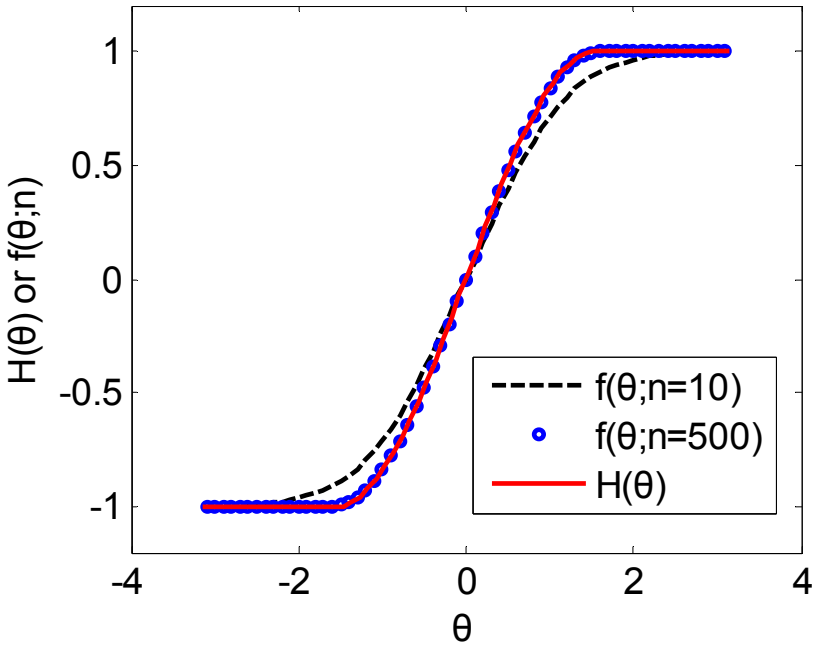

Figure 3.7 Plot of $H(\theta)$ (see (3.78b)) and $f(\theta;n)$ (see (3.42b)) with $n=10$ and 500.

which is *independent of* θ. Similarly, in Region II, $\theta \in (-\pi/2, \pi/2)$, $y_{2,\alpha}$ is determined using (3.24a), (3.70) and (3.73), i.e.,

$$y_{2,1} \approx 0, \quad y_{2,2} \approx \sqrt{-J_m \ln\left(\frac{r}{A_2}\right)} \quad \text{as} \quad \gamma \to \infty. \tag{3.76}$$

Integrating (3.76), the leading behavior of y_2 in Region II is

$$y_2 \approx r\sqrt{-J_m \ln\left(\frac{r}{A_2}\right)} \sin\theta \qquad \theta \in (-\pi/2, \pi/2). \tag{3.77}$$

Finally, y_2 in Region III can be readily determined using the symmetry condition (3.15). It is given by $-y_2$ in Region I. The leading order behavior of y_2 can be summarized by the single equation

$$y_2 \approx r\sqrt{-J_m \ln\left(\frac{r}{A_2}\right)} H(\theta), \tag{3.78a}$$

where

$$H(\theta) \approx \begin{cases} 1 & \theta \in [\pi/2, \pi] \\ \sin\theta & \theta \in (-\pi/2, \pi/2) \\ -1 & \theta \in [-\pi, -\pi/2] \end{cases}. \tag{3.78b}$$

It is very interesting to observe that $H(\theta)$ coincides with $f(\theta; n)$ (see (3.42b)) as $n \to \infty$, as shown in Figure 3.7. As mentioned earlier, the exponential model can be regarded as the "formal" limit of the GNH model as $n \to \infty$.

3.5.2 Leading behavior of y_1

The more difficult task is to determine y_1. Motivated by the results of the GNH material, we assume the leading behavior of y_1 is a separable function of r, θ and

$$|y_{1,1}| \sim |\lambda^3 y_{2,2}|, \quad |y_{1,2}| \sim |\lambda^3 y_{2,1}|. \tag{3.79}$$

Based on these assumptions, we can show that

$$y_1 \approx r\left(-J_m \ln\left(\frac{r}{A_2}\right)\right)^{-1/4} G(\theta), \tag{3.80}$$

where $G(\theta)$ is determined numerically by solving the equation $S_{11,1} + S_{12,2} = 0$ using the leading order behavior of y_2 given by (3.78a,b). The governing equation for $G(\theta)$ and its numerical solution are given in Appendix 3.4.

3.5.3 Asymptotic Stress Fields

The leading order behavior of the stress fields is obtained using the asymptotic deformation fields given in section 3.5.1 and 3.5.2. Equation (3.12) shows that the first Piola-Kirchhoff stresses are proportional to $2dU/dI$, which, for the exponentially hardening model, is

$$2\frac{dU}{dI} = \mu \exp\left(\frac{I-3}{J_m}\right), \tag{3.81a}$$

where

$$I = \gamma^2 + \left(y_{1,1}\right)^2 + \left(y_{1,2}\right)^2 + \lambda^2. \tag{3.81b}$$

Near the crack tip ($r \to 0$), $\left(y_{1,1}\right)^2 + \left(y_{1,2}\right)^2 \to 0$ (see (3.80)) and $\lambda \to 0$. Therefore, (3.81a) becomes

$$2\frac{dU}{dI} \approx \mu \exp\left(\frac{\gamma^2 - 3}{J_m}\right) \qquad \text{as} \quad r \to 0. \tag{3.81c}$$

We now use (3.69a), (3.70) and (3.73) to obtain the leading behavior of $\exp\left(\gamma^2 / J_m\right)$, i.e.,

$$\exp\left(\gamma^2 / J_m\right) = \begin{cases} \dfrac{A_2}{r\left[-J_m \ln\left(r/A_2\right)\right]^2} & \theta \in \left(-\dfrac{\pi}{2}, \dfrac{\pi}{2}\right) \\ \dfrac{A_2}{rJ_m \ln\left(r/A_2\right)} \dfrac{2}{J_m} \cos\theta & \theta \in \left[-\pi, -\dfrac{\pi}{2}\right] \cup \left[\dfrac{\pi}{2}, \pi\right] \end{cases}. \tag{3.82}$$

It is important to note that, because of our approximation in (3.73), (3.82) is accurate only for very large γ or very small r. The first Piola-Kirchhoff stresses can be determined using (3.12), (3.78a,b), (3.80), (3.81c) and (3.82). The results are summarized here.

In regions I and III, $\theta \in [\pi/2, \pi]$ or $[-\pi, -\pi/2]$, these stresses are

$$S_{11} \approx \frac{2\Omega}{J_m} \frac{-\cos\theta}{r\left(-J_m \ln\left(r/A_2\right)\right)^{5/4}} \left(G\cos\theta - G'\sin\theta + \frac{\sin\theta}{\left(G'\right)^3} \right) \tag{3.83a}$$

$$S_{12} \approx \frac{2\Omega}{J_m} \frac{-\cos\theta}{r\left(-J_m \ln\left(r/A_2\right)\right)^{5/4}} \left(G\sin\theta + G'\cos\theta - \frac{\cos\theta}{\left(G'\right)^3} \right) \tag{3.83b}$$

$$S_{21} \approx \frac{2\Omega}{J_m} \frac{-1}{r\sqrt{-J_m \ln\left(r/A_2\right)}} sign(\theta)\cos^2\theta\,, \tag{3.83c}$$

$$S_{22} \approx \frac{2\Omega}{J_m} \frac{-1}{r\sqrt{-J_m \ln\left(r/A_2\right)}} sign(\theta)\cos\theta\sin\theta \quad , \tag{3.83d}$$

where

$$sign(\theta) \equiv \begin{cases} 1 & \theta > 0 \\ -1 & \theta < 0 \end{cases}. \tag{3.83e}$$

In region II, $\theta \in (-\pi/2, \pi/2)$, $S_{\alpha\beta}$ are found to be

$$S_{11} \approx \frac{\Omega}{r\left(-J_m \ln\left(r/A_2\right)\right)^{9/4}} \left(G\cos\theta - G'\sin\theta - \frac{1}{\left(G\cos\theta - G'\sin\theta\right)^3} \right) \tag{3.84a}$$

$$S_{12} \approx \frac{\Omega}{r\left(-J_m \ln\left(r/A_2\right)\right)^{9/4}} \left(G\sin\theta + G'\cos\theta \right) \tag{3.84b}$$

$$S_{21} = o\left(r^{-1}\left(-J_m \ln\left(r/A_2\right)\right)^{-3/2} \right) << S_{22} \tag{3.84c}$$

$$S_{22} \approx \frac{\Omega}{r\left(-J_m \ln\left(r/A_2\right)\right)^{3/2}}\,, \tag{3.84d}$$

where $G(\theta)$ is defined in (3.80) and is determined numerically (see Appendix 3.4). The constant Ω specifies the strength of the singular stress fields and is related to the

positive constant A_2 defined in (3.67) by

$$\Omega = \mu A_2 \exp\left(-3/J_m\right). \tag{3.85}$$

Asymptotic behaviors of the true stress components can be obtained using (3.83), (3.84) and $\mathbf{T} = \mathbf{S}\mathbf{F}^T$. In regions I and III, $\theta \in \left[\pi/2, \pi\right]$ or $\left[-\pi, -\pi/2\right]$, these stresses are

$$T_{11} = \frac{2\Omega}{J_m} \frac{-\cos\theta}{r\left(-J_m \ln\left(r/A_2\right)\right)^{3/2}} \left[G^2 + \left(G'\right)^2 - \frac{1}{\left(G'\right)^2} \right] \tag{3.86a}$$

$$T_{12} = T_{21} = \frac{2\Omega}{J_m} \frac{-\cos\theta}{r\left(-J_m \ln\left(r/A_2\right)\right)^{3/4}} sign(\theta) G \tag{3.86b}$$

$$T_{22} = -\frac{2\Omega}{J_m r} \cos\theta \,. \tag{3.86c}$$

In region II, i.e., $\theta \in \left(-\pi/2, \pi/2\right)$, these stresses are

$$T_{11} = \frac{\Omega}{r\left(-J_m \ln\left(r/A_2\right)\right)^{5/2}} \left[G^2 + \left(G'\right)^2 - \frac{1}{\left(G\cos\theta - G'\sin\theta\right)^2} \right] \tag{3.87a}$$

$$T_{12} = T_{21} = \frac{\Omega}{r\left(-J_m \ln\left(r/A_2\right)\right)^{7/4}} \left(G\sin\theta + G'\cos\theta\right) \tag{3.87b}$$

$$T_{22} = \frac{\Omega}{-J_m r \ln\left(r/A_2\right)} \,. \tag{3.87c}$$

3.5.4 FEM Simulation

To check our asymptotic analysis, we carried out FEM calculations similar to those in Section 3.4.4. The geometry of the FEM model is shown in Figure 3.3a. The applied displacement Δ is *a*. We use $J_m = 3.5$ (see (3.60)) in all simulations. FEM result of the crack opening displacement $y_2(r, \theta = \pi)$ is plotted in Figure 3.8. Our asymptotic result of y_2 in (3.78) with $A_2 = 0.42a$ is also plotted in Figure 3.8. This figure shows good agreement between our asymptotic solution and FEM results for all $r \le 10^{-3} a$. Recall *a*

is the characteristic size of the FEM model (half height of strip). Figure 3.9 compares the FEM result with the asymptotic solution (see (3.80)) of y_1 directly ahead of the crack tip ($\theta = 0$). There are two undetermined constants in (3.80), A_2 and $G(0)$. We use the A_2 determined earlier, i.e., $0.42a$, and use $G(0)$ to fit the FEM results. In this particular example, we found $G(0) = 1.75$ gives a good fit for all $r \le 10^{-2} a$.

To check the angular variation of y_1 and y_2, we use $G(0)$ obtained above to compute $G(\theta)$ (see Appendix 3.4 for the determination of $G(\theta)$). A comparison of numerical solution of $G(\theta)$ with FEM data on two circular paths near the crack tip is shown in Figure 3.10a. These circular paths are the same as those shown in Figure 3.3b. We also compare $H(\theta)$ in (3.78b) with the FEM results in Figure 3.10b. Although our asymptotic solutions deviate from the FEM result, they capture the essential behavior of the angular variation of y_α, e.g. $G(\theta)$ is linear for $\theta > \pi/2$ and nearly constant $H(\theta)$ near $\theta = \pi$. These discrepancies are due to fact that the y_α's are obtained using the approximation (3.73). As mentioned earlier, this approximation is valid only for very large γ or extremely small *r*. When the strains γ are not large enough (see Figure 3.6), (3.73) is accurate only for θ close to 0 and π.

Using the FEM results, we are able to visualize Region I, II and III in the deformed configuration. This is shown in Figure 3.11a. Also, we compare the near-tip crack opening profiles for different material models (GNH with various *n* and the exponentially hardening material) in Figure 3.11b. Although the dominant true stress component, T_{22}, has a similar singularity (~*1/r*), the local crack opening depends on the degree of strain hardening, as is shown in Figure 3.11b.

Finally we plot T_{22} along $\theta = 0$ and $\theta = 3\pi/4$ to check (3.86c) and (3.87c). Figure 3.12 shows different scaling behaviors along the two directions, which is predicted by our solution. In an earlier paper [24], we also plotted T_{22} directly ahead of the crack tip ($\theta = 0$) as a function of *R*, where *R* is the distance from the crack tip in the

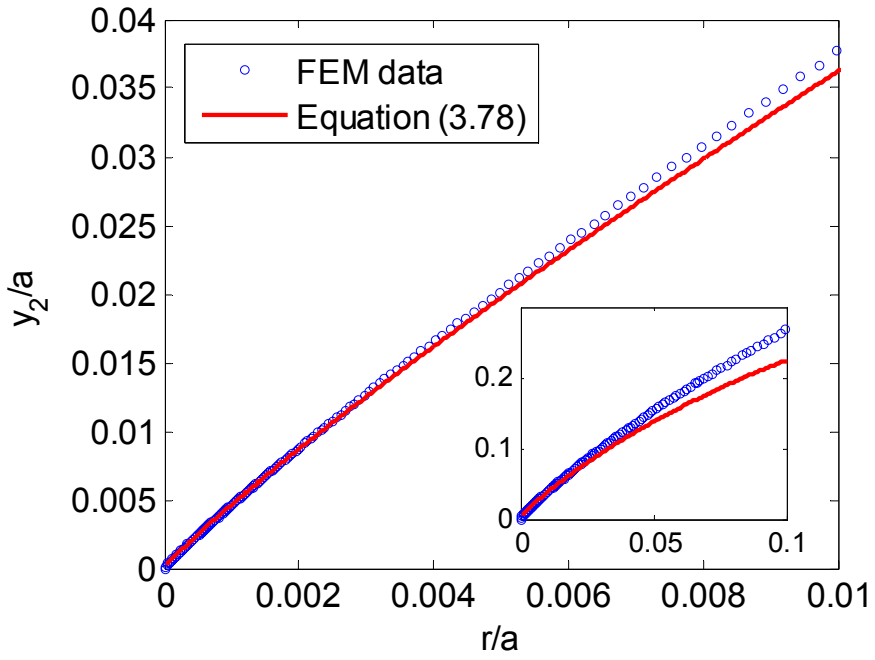

Figure 3.8 Crack opening displacement y_2 / a versus r / a. Symbols are FEM data and the solid line is given by asymptotic solution, (3.78), with $A_2 = 0.42a$. The inset shows the same plot with a larger range of r / a.

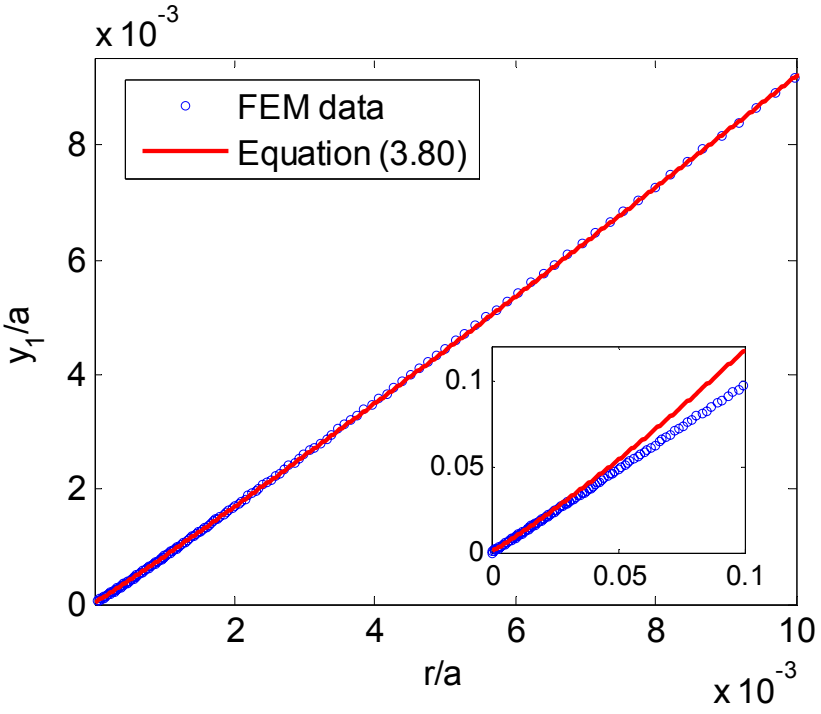

Figure 3.9 Plot of y_1/a ahead of the crack tip ($\theta = 0$) versus r/a. Symbols are FEM data and the solid line is given by asymptotic solution (3.80), with $A_2 = 0.42a$ and $G(0) = 1.75$. The inset shows the same plot with a larger range of r/a.

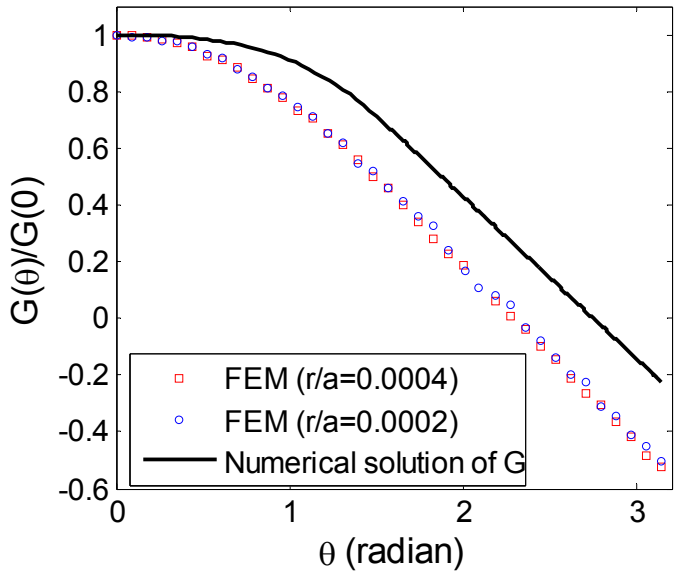

(a)

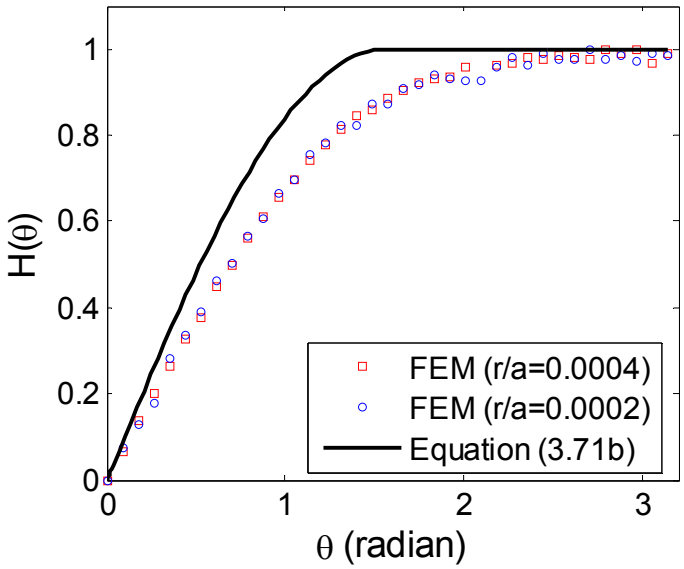

(b)

Figure 3.10 (a) $G(\theta)/G(0)$ versus θ near the crack tip; (b) $H(\theta)$ versus θ near the crack tip. The symbols are FEM data along two circular path with radius r being $4\times10^{-4}a$ and $2\times10^{-4}a$. The solid lines are obtained using our asymptotic solution.

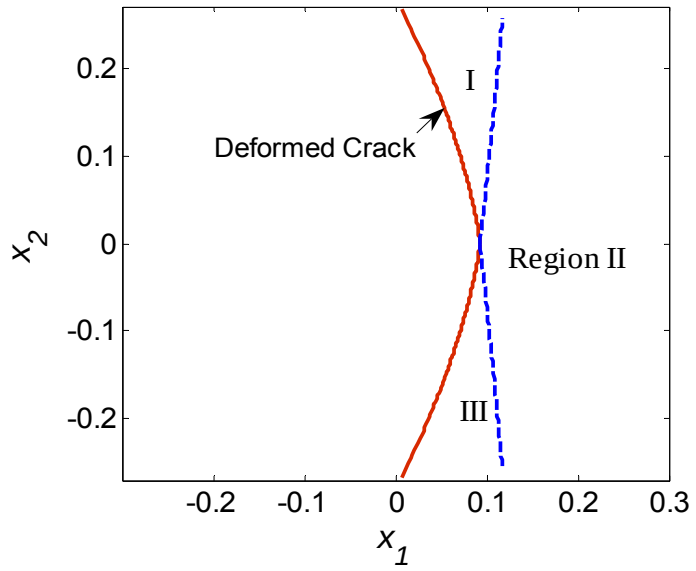

(a)

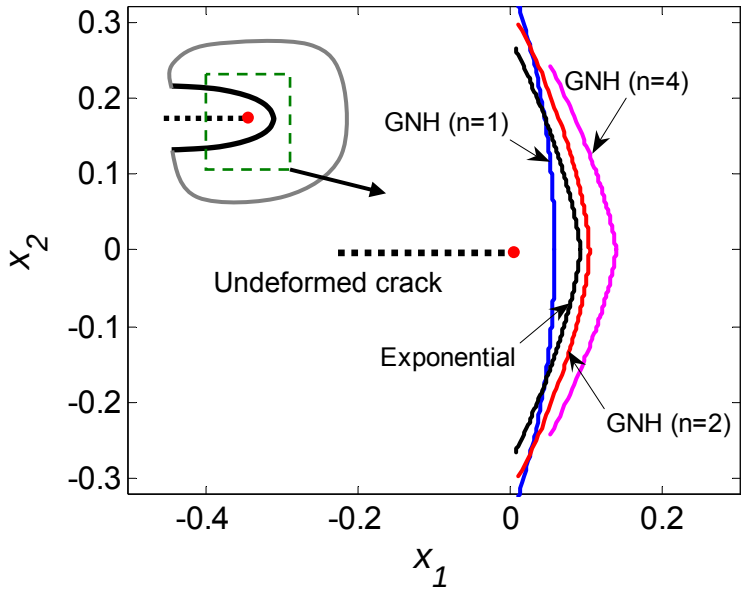

(b)

Figure 3.11 (a) Region I, II and III in the deformed configuration. The dashed lines are the deformed shape of the radial lines $\theta = \pm\pi/2$ that represent the boundary between these regions. (b) FEM results of the local crack opening profile for four different material models, GNH materials with n=1, 2, 4 and the exponentially hardening material with J_m=3.5. The applied displacements Δ are the same for these cases ($\Delta = a$).

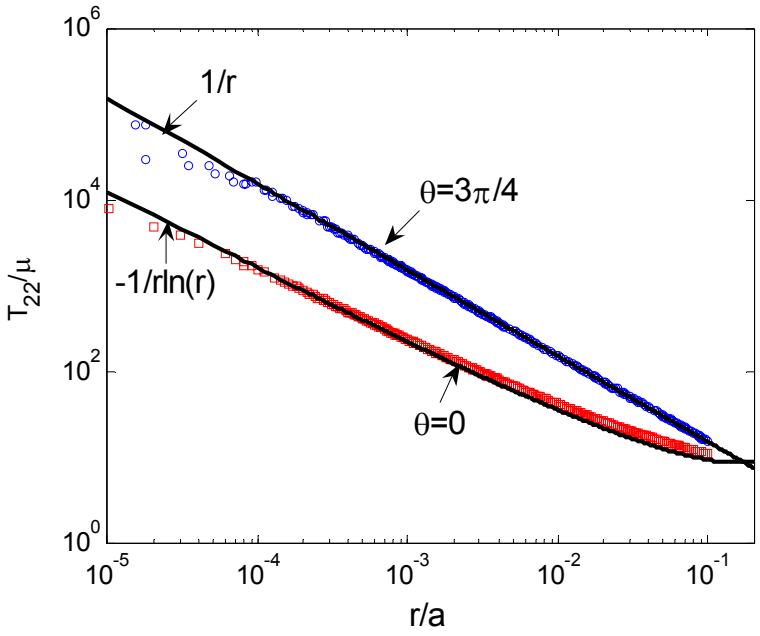

Figure 3.12 True opening stress T_{22} obtained using FEM normalized by shear modulus μ versus r/a along $\theta = 0$ (Region II) and $\theta = 3\pi/4$ (Region I).

deformed configuration. At that time, we had not carried out an asymptotic analysis of the near tip field, so we suggested

$$T_{22} \sim -1/R\ln(R), \quad R=\sqrt{y_\alpha y_\alpha} \tag{3.88}$$

based on a curve fitting of the FEM results. The result of this work shows that (3.88) is slightly different from our asymptotic solution, i.e., it is off by a factor of $\left(-\ln R\right)^{0.25}$. To see this, we set $\theta=0$ in (3.80) and find

$$y_1\left(\theta=0\right)\equiv R=r\left(-J_m\ln\left(\frac{r}{A_2}\right)\right)^{-1/4} G\left(0\right)\Rightarrow r\sim R\left(-\ln R\right)^{1/4}. \tag{3.89}$$

Substituting (3.89) into (3.87c) with $\theta=0$ leads to

$$T_{22}\sim\frac{1}{R\left(-\ln R\right)^{1.25}}. \tag{3.90}$$

3.6 Summary and Discussion

We have developed a method to determine the leading asymptotic behavior of the deformation and stress fields near the tip of a Mode-I plane stress crack in a homogeneous isotropic incompressible hyperelastic solid. Unlike previous analysis, our method does not make assumptions on the specific forms of the crack tip deformation field and thus can be applied to a wider class of material models. We show that the leading order behavior of y_2 under Mode-I loading can be decoupled from y_1 in the vicinity of the crack tip. The nonlinear PDE governing the leading behavior of y_2 can be transformed to a *linear* PDE in the strain plane, where uniqueness and existence of solutions are much easier to prove (we have not provided such proofs). We demonstrated our method for a generalized neo-Hookean solid and an exponentially hardening material. Our asymptotic solutions were supported by FEM simulations.

The finite strain crack tip fields obtained in our analysis differ considerably from

the crack tip fields in LEFM. For example, in LEFM, all stress components have a square root singularity. This means that material elements near the crack tip are subjected to a multi-axial state of stress. In contrast, for GNH and exponential hardening solids, the opening stress component T_{22} has the most severe singularity. As a consequence, material elements in the crack tip region are under unaxial tension. This point has been verified experimentally in Livne *et al.* [3] for a polyacrylamide gel (described by a neo-Hookean material model) under dynamic fracture.

For GNH materials, we extended the results of GK [11] by determining the leading order behavior of y_1 and y_2 for *all* strain hardening exponent *n*. We resolved a problem encountered by GK in their crack tip analysis [11]. They noted that their leading order solution is valid only for $n < n^*$. As a result, how to solve for y_1 when *n* is larger than n^* remains an open question. We resolved this difficulty by discovering an interesting bifurcation in the behavior of y_1 at $n = n^*$ and we found numerically that $n^* \approx 1.46$, consistent with an earlier result by GK. For $n < n^*$, y_1 is given by (3.46), whereas for $n > n^*$, y_1 is given by (3.49b). Note that for $n < n^*$, the leading order behaviors of y_α depend on *two independent* constants (*A* and *B*) which cannot be determined by asymptotic analysis. However, for $n > n^*$, the leading behavior of both y_α is determined by a *single* constant. Stephenson [9] also observed a similar bifurcation when studying plane strain cracks. The material model used by Stephenson [9] is essentially the same as GNH material in the limit of $I \to \infty$. He found that the leading behavior of y_1 under Mode-I condition bifurcates at $n = 1.5$.

It is important to determine near tip fields for $n > n^*$ because soft materials usually exhibit considerable strain hardening. In addition, true stresses near the deformed crack tip are needed to interpret fracture experiments. To determine the true stresses $T_{\alpha\beta}$ from the first Piola-Kirchhoff stresses, it is necessary to determine y_1. It should be noted that although the stresses (both Cauchy and first Piola-Kirchhoff) are *separable* in the

undeformed coordinates (r,θ) for the GNH solid or the exponentially hardening material (*approximately* separable), *they are not separable in the deformed polar coordinates.* This point has not been emphasized in previous works. Indeed, even for the simplest case of a neo-Hookean solid (*n=1* in (1)), the true stresses are not separable in the deformed coordinates [24].

The opening true stress component T_{22} in Mode-I loading for GNH materials decays like $1/r$. This scaling is independent of the material parameter *n*. For the exponentially hardening material, (3.86c) and (3.87c) show that $T_{22} \sim -1/r \ln(r)$ for $|\theta| < \pi/2$ and $T_{22} \sim 1/r$ for $\pi > |\theta| > \pi/2$. This result suggests that it may be a universal fact that T_{22} scales as $1/r$ at least in some angular sector surrounding the crack tip. An examination of the path independent *J*-intergral for large deformation [26] can shed some light on this hypothesis. *J* is defined by

$$J = \int_{\Gamma} \left(W n_1 - \sum_{\beta=1,2} \sum_{\alpha=1,2} S_{\alpha\beta} n_\beta u_{\alpha,1} \right) ds \,, \tag{3.91}$$

where Γ is any path enclosing the crack tip in the reference configuration, n_α is the outward unit normal vector to Γ and *s* is the arc length along Γ. The *J*-integral is the energy release rate of the crack and should have a finite non-zero value. Because of path-independence, we can choose Γ to be a circle of arbitrarily small radius *r* with the center at the crack tip. Assuming the integral of the second term in (3.91) does not vanish as $r \to 0$, we obtain

$$\sum_{\beta=1,2} \sum_{\alpha=1,2} S_{\alpha\beta} n_\beta u_{\alpha,1} \sim 1/r \qquad \text{as} \quad r \to 0 \tag{3.92}$$

for some finite range of θ. In Mode-I loading, it can be shown that, using (3.16b)

$$\sum_{\beta=1,2} \sum_{\alpha=1,2} S_{\alpha\beta} n_\beta u_{\alpha,1} \sim T_{22} \qquad \text{as} \quad r \to 0 \tag{3.93}$$

Equation (3.92), together with (3.93), supports our conjecture on the scaling of T_{22}.

Using the contour Γ described above and the asymptotic solutions, we can

compute the *J*-integral for both material models studied in this chapter. For GNH materials, the *J*-integral is found to be

$$J = \frac{\mu\pi}{2}\left(\frac{b}{n}\right)^{n-1}\left(\frac{2n-1}{2n}\right)^{2n-1} A^{2n}. \tag{3.94}$$

Note that *A* is a coefficient characterizing the magnitude of y_2 (see (3.42a)). Equation (3.94) shows that *A* determines the energy flux to the crack tip. Similarly, for the exponentially hardening material, we found

$$J = \frac{\mu\pi\, \mathrm{e}^{-3/J_m}}{J_m} A_2 \ . \tag{3.95}$$

For this case, A_2 (see (3.78a)) is proportional to the energy flux to the crack tip.

In principle, our method can be extended to obtain the leading behavior of y_α when the crack is subjected to mix-mode loading. Stephenson [9] showed that the near tip displacement fields for mix-mode loading can be obtained by a rotation of the Mode-I displacement fields. Therefore, in mix-mode loading, both y_1 and y_2 will have the same leading behavior (with different amplitudes), and is given by the leading behavior of y_2 in Mode-I. However, the higher order terms are difficult to determine using our method and these higher order terms are necessary to determine the asymptotic behavior of all the stress components. One of the advantages of using power law constitutive models is that it is easier to obtain these higher order terms for mixed mode loading. Indeed, higher order singular terms were obtained in [8-11].

Our analysis can also be extended to compressible materials. For example, consider a compressible material with a work function of the form $W = U_1(I) + U_2(J)$, where $J = \det(\mathbf{F})$ is the volume change ratio of a material element. Under plane stress condition, the in-plane first Piola-Kirchhoff stresses are

$$\begin{bmatrix} S_{11} & S_{12} \\ S_{21} & S_{22} \end{bmatrix} = 2\frac{dU_1}{dI}\begin{bmatrix} y_{1,1} - \lambda^3 y_{2,2}/J & y_{1,2} + \lambda^3 y_{2,1}/J \\ y_{2,1} + \lambda^3 y_{1,2}/J & y_{2,2} - \lambda^3 y_{1,1}/J \end{bmatrix}, \tag{3.96}$$

where λ is the out of plane stretch. Since a material element conserves its mass, J is expected to be positive and bounded everywhere. Thus, one can follow the procedures described in section 3.3 and show that the leading behavior of y_2 is the same as the incompressible case if $U_1(I) = U(I)$. Furthermore, if the following condition is satisfied (similar to (3.43b))

$$\left|y_{1,1}\right| >> \left|\lambda^3 y_{2,2}/J\right| \quad , \quad \left|y_{1,2}\right| >> \left|\lambda^3 y_{2,1}/J\right|, \tag{3.97}$$

then the leading order behavior of y_1 is also the same as the incompressible case if $U_1 = U$. This result is consistent with the analysis of Geubelle and Knauss [11] (incompressible solid) and Tarantino [12] (compressible neo-Hookean solid). However, if (3.97) is not the case, the solution for y_1 is more complicated and is out of the scope of this chapter.

For material models with finite extensibility such as Gent's model [18] and Arruda-Boyce model [17], our method cannot be applied since the strain field is *bounded* near the crack tip. For this class of materials, the deformation field y_1 and y_2 cannot be decoupled. However, we have studied anti-plane shear cracks in these materials and found stress fields that are similar to the exponential model. For example, for Gent's model, our analysis shows that the deformation field is bounded near the crack tip while the shear stress scales as $1/r$.

APPENDIX 3.1

DERIVATION OF (3.42)

Using (3.24b) and (3.40), the physical coordinates (x_1, x_2) are

$$x_1 = r\cos\theta = C_1\gamma^{-2n}\left[(2n-1)\sin^2\phi - \cos^2\phi\right], \tag{A3.1}$$

$$x_2 = r\sin\theta = -2nC_1\gamma^{-2n}\sin\phi\cos\phi\,. \tag{A3.2}$$

Recall that θ and ϕ are the angular polar coordinates of the physical plane and the strain plane, respectively. On the upper crack face ($\theta = \pi$), $y_{2,1} < 0$ and $y_{2,2} = 0$ (see (3.22)). This condition and (3.24a) imply that $\phi = \pi/2$ at $\theta = \pi$. Therefore, (A3.1) requires $C_1 < 0$. Using (A3.1), (A3.2) and (3.41), we obtain

$$\cos\theta = \left[(2n-1)^2\sin^2\phi + \cos^2\phi\right]^{-1/2}\left[(2n-1)\sin^2\phi - \cos^2\phi\right], \tag{A3.3}$$

$$\sin\theta = 2n\left[(2n-1)^2\sin^2\phi + \cos^2\phi\right]^{-1/2}\sin\phi\cos\phi\,. \tag{A3.4}$$

The solution of $\sin\phi$ and $\cos\phi$ in terms of θ is

$$\sin^2\phi = \frac{1}{2n} + \frac{k}{2}\cos^2\theta - \frac{\cos\theta}{2}w \quad , \tag{A3.5}$$

$$\cos^2\phi = 1 - \frac{1}{2n} - \frac{k}{2}\cos^2\theta + \frac{\cos\theta}{2}w\,, \tag{A3.6}$$

where

$$k = 1 - 1/n \quad \text{and} \quad w = \sqrt{1 - k^2\sin^2\theta}\,. \tag{A3.7}$$

Equation (3.41) motivates us to assume that the form of y_2 is

$$y_2 = Ar^{1-1/2n}f(\theta;n), \quad f(\pi;n) = 1\,. \tag{A3.8}$$

where A is a constant coefficient. Equation (3.24a) and (A3.8) imply

$$y_{2,1} = -\gamma\sin\phi = Ar^{-1/2n}\left(1 - \frac{1}{2n}\right)f(\theta;n)\cos\theta - Ar^{-1/2n}f'(\theta;n)\sin\theta\,, \tag{A3.9}$$

$$y_{2,2} = \gamma \cos\phi = Ar^{-1/2n}(1-\frac{1}{2n}) f(\theta;n)\sin\theta + Ar^{-1/2n} f'(\theta;n)\cos\theta . \qquad \text{(A3.10)}$$

$(\text{A3.9})\times\cos\theta + (\text{A3.10})\times\sin\theta$ yields

$$Ar^{-1/2n}(1-\frac{1}{2n}) f(\theta;n) = \gamma\left(-\sin\phi\cos\theta + \cos\phi\sin\theta\right) \ . \qquad \text{(A3.11)}$$

Substituting (3.41) into (A3.11) and replacing θ by ϕ using (A3.3) and (A3.4), we get

$$f(\theta;n) = A^{-1}\left|C_1\right|^{1/2n} 2n\left[\left(2n-1\right)^2 \sin^2\phi + \cos^2\phi\right]^{-\frac{1}{2}+\frac{1}{4n}} \sin\phi . \qquad \text{(A3.12)}$$

To express f in terms of the physical angle θ, we substitute (A3.5) and (A3.6) into $f^2\left(\theta;n\right)$, which gives

$$f^2(\theta;n) = 2nA^{-2}\left|C_1\right|^{1/n}\left[\left(4n^2-4n\right)\left(\frac{1}{2n}+\frac{k}{2}\cos^2\theta-\frac{\cos\theta}{2}w\right)+1\right]^{-1+\frac{1}{2n}} \left(1+nk\cos^2\theta-n\cos\theta w\right) \qquad \text{(A3.13)}$$

Equation (A3.13) can be simplified to

$$f^2(\theta;n) = 4n^2A^{-2}\left|C_1\right|^{1/n}\left(2n-1\right)^{-2+\frac{1}{n}}\left[n\left(k\cos\theta+w\right)\right]^{(n-1)/n}\sin^2\left(\frac{\theta}{2}\right)\left(1-\frac{2k^2\cos^2\left(\theta/2\right)}{1+w}\right). \qquad \text{(A3.14)}$$

We use the fact that $f\left(\theta;n\right)$ is an odd function of θ to obtain a consistent sign convention. Finally, using the normalization condition that $f(\pi;n)=1$, we obtain (3.42b).

APPENDIX 3.2

DERIVATION OF (3.51) AND (3.52)

In this appendix, we derive the governing equation for $g(\theta;n)$. For simplicity, we refer to $f(\theta;n)$ in (42b) and $g(\theta;n)$ in (3.49b) as f and g in the following text. Using the expression of $U(I)$ of generalized neo-Hookean materials (see (3.1)) and the fact $I \approx y_{2,1}^2 + y_{2,2}^2 >> 1$ as $r \to 0$, we can simplify (3.50) to

$$I\left(y_{1,1} - \lambda^3 y_{2,2}\right)_{,1} + (n-1) I_{,1}\left(y_{1,1} - \lambda^3 y_{2,2}\right) + I\left(y_{1,2} + \lambda^3 y_{2,1}\right)_{,2} + (n-1) I_{,2}\left(y_{1,2} + \lambda^3 y_{2,1}\right) = 0 \tag{A3.15}$$

Since $y_1 = Br^{1+\frac{1}{4n}} g$ and $y_2 = Ar^{1-1/2n} f$, we obtain

$$y_{1,1} = B\left(1+\frac{1}{4n}\right) r^{1/4n} \cos\theta g - Br^{1/4n} \sin\theta g', \quad y_{1,2} = B\left(1+\frac{1}{4n}\right) r^{1/4n} \sin\theta g + Br^{1/4n} \cos\theta g',$$
$$y_{2,1} = A\left(1-\frac{1}{2n}\right) r^{-1/2n} \cos\theta f - Ar^{-1/2n} \sin\theta f', \quad y_{2,2} = A\left(1-\frac{1}{2n}\right) r^{-1/2n} \sin\theta f + Ar^{-1/2n} \cos\theta f', \tag{A3.16}$$

where prime denotes derivative with respect to θ. The out of plane stretch ratio λ is

$$\lambda = \frac{1}{y_{1,1}y_{2,2} - y_{1,2}y_{2,1}} = \frac{r^{1/4n}}{AB\left[\left(1+\frac{1}{4n}\right) f'g - \left(1-\frac{1}{2n}\right) fg'\right]}. \tag{A3.17}$$

Let $\xi = \left(1+\frac{1}{4n}\right) f'g - \left(1-\frac{1}{2n}\right) fg'$ and thus $\lambda = r^{1/4n} A^{-1} B^{-1} \xi^{-1}$. The leading term of I is

$$I \approx y_{2,1}^2 + y_{2,2}^2 = A^2 r^{-1/n}\left[\left(1-\frac{1}{2n}\right)^2 f^2 + \left(f'\right)^2\right] \equiv A^2 r^{-1/n} M\left(\theta\right). \tag{A3.18}$$

The first order term of $y_{1,1}-\lambda^3 y_{2,2}$ is

$$y_{1,1}-\lambda^3 y_{2,2}=B\left(1+\frac{1}{4n}\right)r^{1/4n}\cos\theta g-Br^{1/4n}\sin\theta g'-r^{1/4n}\frac{\left(1-\frac{1}{2n}\right)\sin\theta f+\cos\theta f'}{A^2B^3\xi^3}$$

(A3.19)

We impose the condition that $B^4=A^{-2}$. As a result, to ensure no loss of generality, $g(\theta=0)$ can not be prescribed by the normalization condition but is part of the solution. Using this condition, we obtain

$$y_{1,1}-\lambda^3 y_{2,2}=Br^{1/4n}\left(\left(1+\frac{1}{4n}\right)g\cos\theta-g'\sin\theta-\frac{\left(1-\frac{1}{2n}\right)f\sin\theta+f'\cos\theta}{\xi^3}\right)\equiv Br^{1/4n}K(\theta)$$

and

$$y_{1,2}+\lambda^3 y_{2,1}=Br^{1/4n}\left(\left(1+\frac{1}{4n}\right)g\sin\theta+g'\cos\theta+\frac{\left(1-\frac{1}{2n}\right)f\cos\theta-f'\sin\theta}{\xi^3}\right)\equiv Br^{1/4n}L(\theta)$$

(A3.20)

Using (A3.18) and (A3.20), we obtain

$$\left(\frac{5}{4n}-1\right)M\left(K\cos\theta+L\sin\theta\right)+M\left(-K'\sin\theta+L'\cos\theta\right)+\left(n-1\right)M'\left(L\cos\theta-K\sin\theta\right)=0$$

(A3.21)

Equation (A3.21) is a second order differential equation for $g(\theta;n)$. To solve it numerically, we need an explicit expression of g''. We can show that

$$-K'\sin\theta+L'\cos\theta=\left(1+\frac{1}{4n}\right)g+g''-\frac{f'}{2n\xi^3}-3\left(1-\frac{1}{2n}\right)f\frac{3f'g'+\left(4n+1\right)f''g-\left(4n-2\right)fg''}{4n\xi^4}$$

(A3.22)

$$K\cos\theta + L\sin\theta = \left(1+\frac{1}{4n}\right)g - \frac{f'}{\xi^3} \tag{A3.23}$$

$$L\cos\theta - K\sin\theta = g' + \left(1-\frac{1}{2n}\right)\frac{f}{\xi^3} \tag{A3.24}$$

$$M' = 2\left(1-\frac{1}{2n}\right)^2 ff' + 2ff'' \quad . \tag{A3.25}$$

Substituting (A3.22)-(A3.25) into (A3.21), we can obtain the governing equation (3.51). Next we derive boundary conditions for $g(\theta;n)$. By symmetry, $g(\theta;n)$ should be an even function of θ, which implies

$$g'(\theta=0)=0 \quad . \tag{A3.26}$$

Using (A3.20) and the fact that $f(\theta=\pm\pi;n)=\pm1$ and $f'(\theta=\pm\pi;n)=0$, the traction free boundary condition (3.14d) becomes

$$\left[g'(\pm\pi)\right]^2 = \frac{2n}{(2n-1)} \quad . \tag{A3.27}$$

Since $g'(\theta;n)$ is an odd function of θ, we impose the following condition without loss of generality:

$$g'(\theta=\pi) = -\sqrt{\frac{2n}{2n-1}} \ , \ g'(\theta=-\pi) = \sqrt{\frac{2n}{2n-1}} . \tag{A3.28}$$

APPENDIX 3.3

ASYMPTOTIC BEHAVIOR OF $z(\rho)$ IN (3.66)

Equation (3.64) implies

$$\frac{d^2z}{d\rho^2}+\frac{1+\rho^2}{\rho}\frac{dz}{d\rho}-\chi\left(1+\frac{1}{\rho^2}\right)z=0 \quad . \tag{A3.29}$$

Equation (A3.29) has an irregular singular point at $\rho=\infty$; so we assume a solution of the form:

$$z=e^{S(\rho)} . \tag{A3.30}$$

Substituting (A3.30) into (A3.29) leads to

$$\left[\ddot{S}+\left(\dot{S}\right)^2\right]+\left(\rho+\frac{1}{\rho}\right)\dot{S}-\chi\left(1+\frac{1}{\rho^2}\right)=0 . \tag{A3.31}$$

where dot denotes derivatives with respect to ρ. Assuming that $\left(\dot{S}\right)^2 >> \ddot{S}$ as $\rho\to\infty$ and neglecting $\ddot{S}$ in (A3.31), we obtain an algebraic equation for $\dot{S}_0$, where S_0 is the leading order term in the expansion of $S(\rho)$ as $\rho\to\infty$. The solution of (A3.31) is

$$\dot{S}_0=-\frac{1}{2}\left(\rho+\frac{1}{\rho}\right)\pm\frac{1}{2}\sqrt{\left(\rho+\frac{1}{\rho}\right)^2+4\chi\left(1+\rho^{-2}\right)} \quad . \tag{A3.32}$$

As $\rho\to\infty$, the asymptotic behaviors of two solutions in (A3.32) are

Solution 1 (negative sign in (A3.32)): $\dot{S}_0\approx-\rho$ as $\rho\to\infty$, (A3.33)

Solution 2 (positive sign in (A3.32)): $\dot{S}_0\approx\chi/\rho$ as $\rho\to\infty$. (A3.34)

(A3.34) implies $\left(\dot{S}_0\right)^2$ is on the same order as $\ddot{S}_0$, a contradiction to our assumption. As a result, we choose Solution 1, i.e., (A3.33). Next we calculate the second order term in

the expansion of $S(\rho)$. Let $S = -\rho^2/2 + S_1$ and $|S_1| << \rho^2/2$ as $\rho \to \infty$. Substituting this relation into (A3.31) gives

$$-2 + \ddot{S}_1 - \rho\dot{S}_1 + (\dot{S}_1)^2 + \dot{S}_1/\rho - \chi(1-\rho^{-2}) = 0\,. \tag{A3.35}$$

Since $|\rho\dot{S}_1| >> (\dot{S}_1)^2$, $|\rho\dot{S}_1| >> |\dot{S}_1/\rho|$ and $|\ddot{S}_1| << 1$, we have

$$2 + \chi + \rho\dot{S}_1 = 0 \quad , \tag{A3.36}$$

which implies $\dot{S}_1 = -(2+\chi)/\rho$. One can follow this procedure to obtain the third order term S_2 in S. It can be shown that $\dot{S}_2 = O(\rho^{-3})$. Therefore, the asymptotic behavior of $\dot{S}$ as $\rho \to \infty$ is

$$\dot{S} = -\rho - \frac{(\chi+2)}{\rho} + O(\rho^{-3}) \quad . \tag{A3.37}$$

This means that

$$S(\rho) \approx -\frac{\rho^2}{2} - (\chi+2)\ln\rho + O(\rho^{-2})\,. \tag{A3.38}$$

Using (A3.30) and (A3.38), we obtain (3.66).

APPENDIX 3.4

SOULUTION OF $G(\theta)$ IN (3.80)

Similar to Appendix 3.2 where we derive the governing equation of y_1 for generalized neo-Hookean materials, using (3.12) and (3.60), we can simplify the equilibrium equation $S_{11,1}+S_{12,2}=0$ to

$$\frac{I_{,1}}{J_m}\left(y_{1,1}-\lambda^3 y_{2,2}\right)+\left(y_{1,1}-\lambda^3 y_{2,2}\right)_{,1}+\frac{I_{,2}}{J_m}\left(y_{1,2}+\lambda^3 y_{2,1}\right)+\left(y_{1,2}+\lambda^3 y_{2,1}\right)_{,2}=0\,, \tag{A3.39}$$

where *I* is determined by the leading order behavior of y_2 given in (3.78a,b), i.e.

$$I=-J_m\ln\left(\frac{r}{A_2}\right),\quad I_{,1}=-\frac{J_m}{r}\cos\theta\,,\quad I_{,2}=-\frac{J_m}{r}\sin\theta\ . \tag{A3.40}$$

Using (3.78a,b) and (3.79) and assuming y_1 is a separable function of r,θ, we obtain (3.80). For $\theta\in[\pi/2,\pi]$, (A3.39) implies

$$G''=0\quad , \tag{A3.41}$$

where prime denotes derivative with respect to θ. The traction free boundary condition $S_{12}|_{\theta=\pi}=0$ leads to

$$G'|_{\theta=\pi}=\pm 1 \tag{A3.42}$$

Equations (A3.41) and (A3.42) show that $G'=\pm 1$ for all $\theta\in[\pi/2,\pi]$. However, $G'=1$ implies that y_1 is an increasing function of θ in $\theta\in[\pi/2,\pi]$ for a constant *r* near the crack tip. This will generate an unphysical crack tip deformation field, since y_2 is nearly independent of θ in $\theta\in[\pi/2,\pi]$ (see (3.78)). Therefore, we choose

$$G'=-1\qquad \text{for}\ \ \theta\in[\pi/2,\pi] \tag{A3.43}$$

For $\theta\in[-\pi/2,\pi/2]$, the governing equation for $G(\theta)$ is

$$G'' = -\frac{3G\sin^2\theta + G\cos^2\theta - G'\sin\theta\cos\theta}{\left(G\cos\theta - G'\sin\theta\right)^4 + 3\sin^2\theta} \quad \text{with} \quad G'|_{\theta=0} = 0 \ . \tag{A3.44}$$

The boundary condition in (A3.44) comes from the requirement that $G(\theta)$ should be an even function because of the symmetry in Mode-I condition. We impose the continuity of $G'(\theta)$ at $\theta = \pi/2$, that is

$$G'|_{\theta=(\pi/2)^-} = -1 \tag{A3.45}$$

Equations (A3.44) and (A3.45) can be solved using a shooting method. We should require $G(0) > 0$ since $y_1(r, \theta = 0) > 0$. Numerical experiments suggest that for $G(0)$ larger than 0.2, (A3.45) can always be satisfied with relative error smaller than 0.1%. This feature suggests that $G(0)$ depends on the external loading and specimen geometry and can not be determined by asymptotic analysis. Once $G(0)$ is known we can solve for $G(\theta)$ where $\theta \in [0, \pi]$ using (A3.43) and (A3.44), with the requirement that $G(\theta)$ is continuous at $\theta = \pi/2$. This solution can be easily extended to $[-\pi, \pi]$ since $G(\theta)$ is an even function.

REFERENCES

[1] Buehler M.J., Abraham F.F., Gao, H.J., 2003, *Nature*, **426**, 141-146.

[2] Buehler M.J., Gao H.J., 2006, *Nature*, **439**, 301-310.

[3] Livne A., Bouchbinder E., Svetlizky I., Fineberg J., 2010, *Science*, **327**, 1359-1363.

[4] Bouchbinder E., Livne A., Fineberg J., 2008, *Phys. Rev. Lett.*, **101**, 264302.

[5] Bouchbinder E., Livne A., Fineberg J., 2009, *J. Mech. Phys. Solids*, **57**, 1568-1577.

[6] Wong F., Shield T., 1969, *ZAMP*, **20**, 176-199.

[7] Knowles J.K., Sternberg, E., 1973, *J. Elasticity*, **3**, 67-107.

[8] Knowles J.K., Sternberg, E., 1974, *J. Elasticity*, **4**, 201-233.

[9] Stephenson R.A., 1982, *J. Elasticity*, **12**, 65-99.

[10] Knowles J.K., 1977, *Int. J. Fract.*, **13**, 611-639.

[11] Geubelle P.H., Knauss W.G., 1994, *J. Elasticity*, **35**, 61-98.

[12] Tarantino A.M., 1996, *J. Elasticity*, **44**, 37-59.

[13] Knowles J.K., Sternberg E., 1983, *J. Elasticity*, **13**, 257-293.

[14] Geubelle P.H., Knauss W.G., 1994, *J. Elasticity*, **35**, 99-138.

[15] Geubelle P.H., Knauss W.G., 1994, *J. Elasticity*, **35**, 139-174.

[16] Herrmann J.M., 1989, *J. Elasticity*, **21**, 227-269.

[17] Arruda E.M., Boyce M.C., 1993, *J. Mech. Phys. Solids*, **41**, 389-412.

[18] Gent A.N., 1996, *Rubber Chem. Tech.*, **69**, 59-61.

[19] Boyce M.C., Arruda E.M., 2000, *Rubber Chem. Tech.*, **73**, 504-523.

[20] Seitz M.E., Martina D., Baumberger T., Krishnan V.R., Hui C.Y., Shull, K.R., 2009, *Soft Matter*, **5**, 447-456.

[21] Baumberger T., Caroli C., Martina D., 2006, *Nature Mater.*, **5**, 552-555.

[22] Baumberger T., Caroli C., Martina D., 2006, *Euro. Phys. J. E.*, **21**, 81-89.

[23] Rice J.R., 1967, *J. Appl. Mech.*, **34**, 287-298.

[24] Krishnan V.R., Hui C.Y., Long, R., 2008, *Langmuir*, **24**, 14245-14253.

[25] Cristiano A., Marcellan A., Long R., Hui C.Y., Stolk J., Creton C., 2010, *J. Polym. Sci., Part B: Polym. Phys.*, **48**, 1409-1422.

[26] Eshelby J.D., 1969, *Energy relastions and the energy-momentum tensor in continuum mechanics* in *Inelastic behavior of solids*. McGraw-Hill, New York, pp.77-11.

CHAPTER 4

EFFECTS OF TRIAXIALITY ON THE GROWTH OF CRACK-LIKE CAVITIES IN SOFT INCOMPRESSIBLE ELASTIC SOLIDS[3]

4.1 Introduction

Soft elastic materials such as rubber and gels often fail by nucleation and growth of cavities [2-6]. For example, Gent and Lindley [2] discovered the sudden appearance of internal cracks in a rubbery layer bonded between two flat rigid substrates under a comparatively small applied tensile load. Nucleation of cavities was also observed in pressure sensitive adhesives at or near the adhering interface upon debonding [3-6]. These cavities grow parallel to the interface and form a fibrillar structure before the adhesive eventually fails [3,4].

A large literature of theoretical works has studied how cavities deform in soft elastomers [7-12]. Most of these studies focus on spherical or cylindrical cavities under hydrostatic tension. This is because the deformation field under these conditions is one-dimensional which allows analytical treatment. A well known result is that a spherical cavity in an infinite block of neo-Hookean solid loaded by internal pressure will grow without bound when the pressure reaches a value of $5E/6$, where E is the small strain elastic modulus [7]. Approximate analytical solution for the growth of an initially spherical cavity in a neo-Hookean solid under remote tensile loads that are non-hydrostatic was obtained by Hou and Abeyaratne [12]. A special case of Hou and Abeyaratne's work where the remote tensile stresses are axis-symmetric was studied by Chang *et al.* [13] numerically using finite element method (FEM). The critical loads for the cavity to grow without bound were determined in these works.

---

[3]Long R., Hui C.Y., 2010, *Soft Matter*, **6**, 1238-1245. *Reproduced by permission of The Royal Society of Chemistry*.
Paper Link: http://www.rsc.org/publishing/journals/SM/article.asp?doi=b917148g

The works mentioned above typically assume that cavities are spherical and grow by reversible elastic deformation. In reality, cavities can have different shapes. Furthermore, they can grow by irreversibly breaking molecular bonds and creating new defect surface. Here we consider cavities that are crack-like defects. In this case, whether it grows or not depends on how much energy is available to drive the crack growth. Qualitatively, this energy flow can be characterized by energy release rate G which is the amount of potential energy loss per unit area of crack growth. Experiments have shown that the initiation of crack growth in elastomers can be determined by the condition $G = G_c$ where G_c is the fracture toughness [14,15]. The deformation and energetic of cracks in stiff elastic solids are well established by linear elastic fracture mechanics (LEFM) theory. However, soft materials often undergo very large deformation because of their low modulus which ranges from several KPa to MPa. Such large deformation invalidates the basic assumption of LEFM which is based on small strain theory. For example, the crack tip stress fields near the tip of plane strain or plane stress cracks are very different from those predicted by LEFM, as demonstrated by previous theoretical works [16-20]. Recent numerical results [21, 22] lend further support to these finite strain fracture theories.

Our study in this chapter is partly motivated by a recent experiment of Cristiano *et al.* [23]. A schematic of this experiment is shown in Figure 4.1. A thin elastomer layer is bonded between a flat rigid substrate and a rigid spherical indenter which has a radius much greater than the average thickness of the layer. The elastomer layer is curved on one side to conform to the curvature of the sphere to eliminate residual stresses. The idea behind this set up is to introduce a stress concentration at the center of the layer so that a *single* cavity is nucleated there when the indenter is pulled upwards. Nucleation of a single crack-like defect is indeed observed in their experiments. They found that the defect grows when the applied displacement reaches a critical level. The lateral

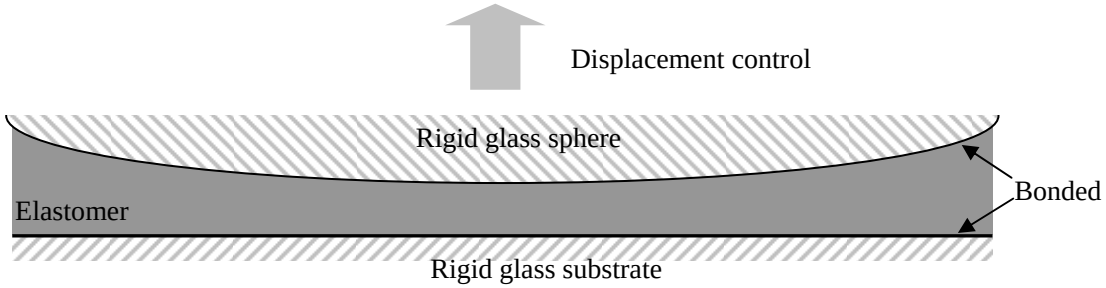

Figure 4.1 Schematic of the elastomer cavitation experiment. Only a cross section of the axis-symmetric geometry is shown in this graph.

constraint caused by the incompressible thin layer suggested that the small crack-like defect is initially subject to almost pure hydrostatic tension. As it grows, it enters into regions of lower triaxiality η, which we defined as the ratio of tensile stress parallel to the undeformed crack face (S) versus the tensile stress perpendicular to the undeformed crack face (T).

An interesting question is how changes in triaxiality affect the energy release rate. According to LEFM, the energy release rate is *not* affected by triaxiality since a stress field that is parallel to the crack faces can be superimposed without changing the stress intensity factor. Indeed, the energy release rate G of a penny-shaped crack with radius a in an infinite block of incompressible *linearly* elastic solid subjected to remote tension T is [24]

$$G = \frac{3T^2 a}{\pi E} \quad , \tag{4.1}$$

where E is the Young's modulus. This result is independent of S, the remote stress field applied parallel to the crack faces.

The experimental set up of Cristiano *et al.* [23] is very specific and complicated to analyze. Here we consider a more generic problem, that is, we study the effect of triaxility on the energy release rate of a single penny-shaped crack in an infinite block of hyperelastic solid subjected to remote tension stress T and S (see Figure 4.2). Specifically, T and S are the true (Cauchy) stresses normal and parallel to the undeformed crack faces respectively. The undeformed radius of the penny-shaped crack is denoted by a. The degree of triaxiality is measured by η, which is defined as

$$\eta = S / T \, . \tag{4.2}$$

The energy release rate G is defined as [25]:

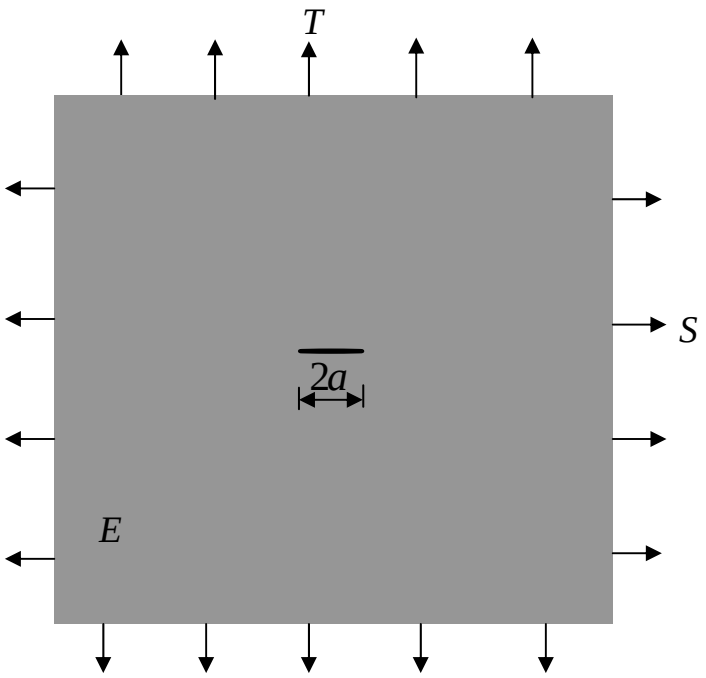

Figure 4.2 Cross-section of a circular crack of undeformed radius *a* in an infinite hyperelastic material under axisymmetric tensile loading. The solid has an infinitesimal Young's modulus *E*. *T* and *S* is the true tension perpendicular and parallel to the undeformed crack faces respectively. The crack is shown in the undeformed configuration. When subjected to *T* and *S*, the crack will open and deform to a cavity enclosing some finite volume.

$$G = -\left.\frac{\partial U}{\partial A}\right|_{T,S} \quad , \tag{4.3}$$

where U is the potential energy of the system and A is the area of one crack surface in the undeformed reference configuration.

The energy release rate of cracks under large deformation was studied by Gent and Wang [26]. They used an approximate analysis to determine the energy release rate of a penny-shaped crack in an infinite neo-Hookean material under remote hydrostatic tension. Their analysis was based on the analytical solution of a spherical cavity deforming under internal pressure [27]. As pointed out by Lin and Hui [1], who studied the same problem numerically using a finite element method, the approximate solutions of Gent and Wang deviate significantly from their FEM results. Their FEM method is based on an energy balance argument and is a special case of our problem where $S/T = 1$. To our best knowledge, there have been no investigations on how the energy release rate of a penny-shape crack depends on the triaixiality. It should be noted that although there exist many theoretical analyse on the crack tip field of a plane stress or plane strain crack in large deformation [16-20], no such results are available for axis-symmetric cracks in the literature.

The plan of this chapter is as follows. The theoretical framework on the calculation of energy release rate is established in section 4.2. Section 4.3 introduces the material models we used in the calculation. Section 4.4 explains the FEM implementation we used to calculate the energy release rate. Results are presented in section 4.5 and summary and discussion is given in section 4.6.

4.2 Energy Release Rate

Energy release rate can be determined using the global energy change method, the

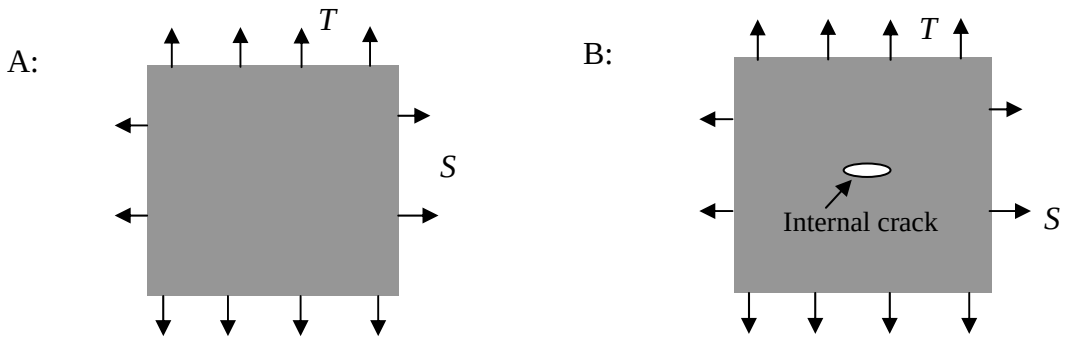

Figure 4.3 State A: an infinite uncracked elastic solid under axisymmetric tensile load *T* and *S*; State B: the same solid with an internal penny-shaped crack of undeformed radius *a* subjected to remote tensile true stresses *T* and *S*.

J-integral method, compliance method and virtual crack extension method (VCEM) [28]. However, global energy change method and compliance method are difficult to apply in our problem because the media is infinite. The J-integral and VCEM method requires very accurate stress fields around the crack tip which creates difficulty in the finite element implementation at very large deformations. The method we used in this chapter is based on a simple energy balance argument which only requires us to compute the deformed crack volume. This feature significantly increases accuracy and reduces computational efforts.

We start the derivation of our energy balance method by comparing the difference of potential energy between the two states A and B shown in Figure 4.3. Denote the potential energy of state A and state B by U_A and U_B respectively. The potential energy of state A or B is a combination of strain energy of the elastic solid and potential energy of the loading system that applies tensile loads to the solid. U_A and U_B are both infinite because the elastic media is infinite. However, the difference between U_A and U_B, denoted by ΔU, is finite, i.e.,

$$\Delta U \equiv U_A - U_B \quad . \tag{4.4}$$

Since a is the only length scale in this problem, dimensional analysis shows that ΔU is given by

$$\Delta U = Ea^3 \tilde{U}\left(\frac{T}{E}, \frac{S}{T}\right) \ , \tag{4.5}$$

where E is the infinitesimal Young's modulus of the hyper-elastic solid and $\tilde{U}$ is a dimensionless quantity which only depends on T/E and S/T. Equations (4.3), (4.4) and (4.5) and axisymmetry imply the energy release rate is proportional to $\tilde{U}$, that is,

$$G = -\frac{\partial U_B}{\partial A} = -\frac{\partial\left(U_A - \Delta U\right)}{\partial\left(\pi a^2\right)} = \frac{3Ea}{2\pi}\tilde{U}\left(\frac{T}{E}, \frac{S}{T}\right). \tag{4.6}$$

Since the material is elastic, the energy difference between state A and B is independent of deformation history. Therefore, the normalized potential energy difference $\tilde{U}$ can be found by considering the following process. In the first step of this process, we make a cut in the elastic solid in state A to create a circular crack so that this crack will have radius *a* upon unloading. Note that the circular cut in state A has a different radius than the undeformed crack radius *a* because material elements in state A is deformed due to the applied stress *T* and *S*. For example, if *S=0* and *T>0*, the radius of the circular cut in state A is smaller than *a* because of lateral contraction. During this step, a uniform normal traction *T* is applied to the two crack faces to prevent the crack from opening. In other words, the cut does not change the potential energy of state A. The normal traction *T* applied on the crack faces can also be viewed as a hydrostatic tension or negative hydrostatic pressure acting on them. Next, we release the hydrostatic tension applied on the crack face, denoted by *t*, from *T* to 0 quasi-statically while keeping the remote tensile true stress *T* and *S* constant. State B is achieved when $t = 0$. During this crack face tension releasing process, the volume enclosed by the crack surface, denoted by *V*, increases from 0 to V_0, where V_0 is the crack volume in state B.

Energy balance requires

$$U_B - U_A = W = -\int_0^{V_0} t dV , \tag{4.7}$$

where *W* is the work done by the crack face tension. We introduce the normalized tension $\bar{t}$ and normalized crack volume $\bar{V}$ by:

$$\bar{t} = t / E, \qquad \bar{V} = V / a^3 . \tag{4.8}$$

Dimensional analysis implies that $\bar{t}$ can be written as

$$\bar{t} = \bar{t}\left(\bar{V}; \frac{T}{E}, \frac{S}{T}\right) . \tag{4.9}$$

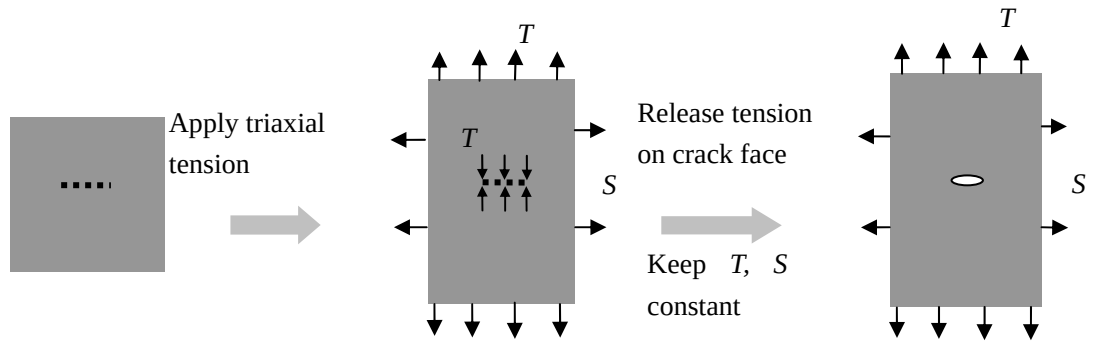

(a). Undeformed (b). Crack face held by tension T (c). Crack face traction free

Figure 4.4 Our path to calculate energy release rate: (a) Infinite elastic solid with a circular crack of radius a. (b) Apply remote axis-symmetric tensile load T and S to the elastic solid while holding the crack face closed by tension T. State A in Figure 4.3 is achieved after this step. (c) Release the hydrostatic tension applied on the crack face from T to 0 quasi-statically. Determine the volume enclosed by crack face during the release of crack face tension. Equation (4.10) is then used to calculate the energy release rate.

Using (4.6), (4.7), (4.8) and (4.9), we obtain

$$G = \frac{3Ea}{2\pi}\tilde{U}\left(\frac{T}{E},\frac{S}{T}\right) = \frac{3Ea}{2\pi}\int_0^{\bar{V}_0} \bar{t}\left(\bar{V};\frac{T}{E},\frac{S}{T}\right)d\bar{V} \tag{4.10}$$

where $\bar{V}_0 = V_0 / a^3$.

Our calculations of energy release rate are based on equation (4.10), that is, we first determine how $\bar{t}$ changes with $\bar{V}$ for a given *T* and *S*. We then evaluate the integral in (4.10) to obtain energy release rate *G*. Our idea is illustrated schematically in Figure 4.4.

Our energy balance argument is inspired by Yeoh [29], who studied the energy release rate of a *plane stress* crack in an infinite hyper-elastic sheet. In his paper, the energy difference ΔU was calculated by releasing the crack face tension. Instead of using a hydrostatic tension, the crack face tension in Yeoh's work was always perpendicular to the undeformed crack face. The energy difference was computed by the work done on displacing the crack face in the direction of the crack face tension. So far, his analysis is exact. However, he used the approximation that the crack opening displacement in the direction of the crack face tension is a linear function of crack face tension despite the fact that the crack faces undergo very large deformation. Another approximation employed by Yeoh is that the crack face is stretched uniformly along the direction of the undeformed crack. These two approximations were justified by the FEM results in his paper. In our case, we choose a release process based on hydrostatic crack face tension because of axis-symmetry. We do not use the linearity and uniform stretch assumptions. Instead, we use FEM to study exactly on how $\bar{t}$ depends on $\bar{V}$ for a given set of remote stresses *T* and *S*.

4.3 Material Model

Two incompressible hyper-elastic material models are used in this chapter:

neo-Hookean material and a material model that strain hardens exponentially. The strain energy density function for a neo-Hookean solid, first proposed by Treloar [30], is

$$W = \frac{E}{6} I_1 \tag{4.11}$$

where

$$I_1 = \lambda_1^2 + \lambda_2^2 + \lambda_3^2 . \tag{4.12}$$

λ_1, λ_2 and λ_3 are the three principal stretch ratios [31] and E is the small strain elastic modulus. We choose this model because it is the simplest hyperelastic material model that captures large deformation features. Also, since Lin and Hui [1] has studied the special case when $S/T = 1$, their results can be used as a validity check to our calculation.

It is well known that neo-Hookean material underestimates the degree of strain hardening. We consider the effect of strain hardening using an exponentially hardening material model proposed by Seitz *et al.* [32]. They performed fracture experiments on an elastic hydrogel made of acrylic triblock copolymers with poly(methyl methacrylate) [PMMA] endblocks and a poly(n-butyl acrylate) [PnBA] midblock. The strain energy density function W given below was found to predict the uniaxial compression test data accurately:

$$W = \frac{EI^*}{6}\left[\exp\left(\frac{I_1 - 3}{I^*}\right) - 1\right] \tag{4.13}$$

where I^* is a material constant which controls the amount of strain hardening. For moderate and large I_1 / I^*, the exponential model exhibits very severe strain hardening behavior. However, if I_1 / I^* is small, which may occur when deformation is small (small I_1) or I^* is large, the exponential model approaches neo-Hookean solid, that is,

$$W\left(\frac{I_1}{I^*} << 1\right) = \frac{EI_1}{6} \tag{4.14}$$

Cristiano *et al.* [23] used equation (4.13) model to fit the uni-axial compression test data of the elastomeric materials used in their experiments. Representative values of I^* were found to be 8.56, 7.03 and 5.09 for the three types of materials used in their experiments. These values are used in our numerical calculations.

4.4 Finite Element Method

We use a commercial FEM software, ABAQUS [33], to compute $\bar{t}$ and $\bar{V}$ for a given remote stresses T and S. The deformed crack profile for a given $\bar{t}$ from ABAQUS is imported to Matlab. The crack volume $\bar{V}$ and energy release rate is then computed in Matlab using (10). Axisymmetry allows us to create a two dimensional FEM model. Only the upper half of the elastic solid is considered because of symmetry. While the neo-Hookean model is already built in ABAQUS, the exponentially hardening material has to be implemented by a user subroutine (UHYPER) written in FORTRAN. The infinite extent of the elastic solid is approximated by choosing an outer boundary with linear dimensions much greater than the crack radius. We have verified that the extent of this boundary has no practical effect on our calculation. All dimensions are normalized by the initial crack radius a. The geometry and boundary conditions in our FEM model are shown in Figure 4.5. We apply load to the FEM model according to the loading path shown in Figure 4.4. The crack tension releasing process (from *b* to *c* in Figure 4.4) is implemented by reducing the crack face tension step by step from T to 0. In most cases, the releasing step size is $\Delta t = 0.01E$ except when T is smaller than $0.1E$. For this case a smaller step size Δt is used. We update the mesh in our calculation using a re-meshing technique to avoid distortion of mesh near the crack tip. Typical meshes which all consists of quadrilateral elements (CAX4RH) are shown in Figure 4.6. Details of the re-meshing technique and a superposition treatment are given in Appendix 4.1.

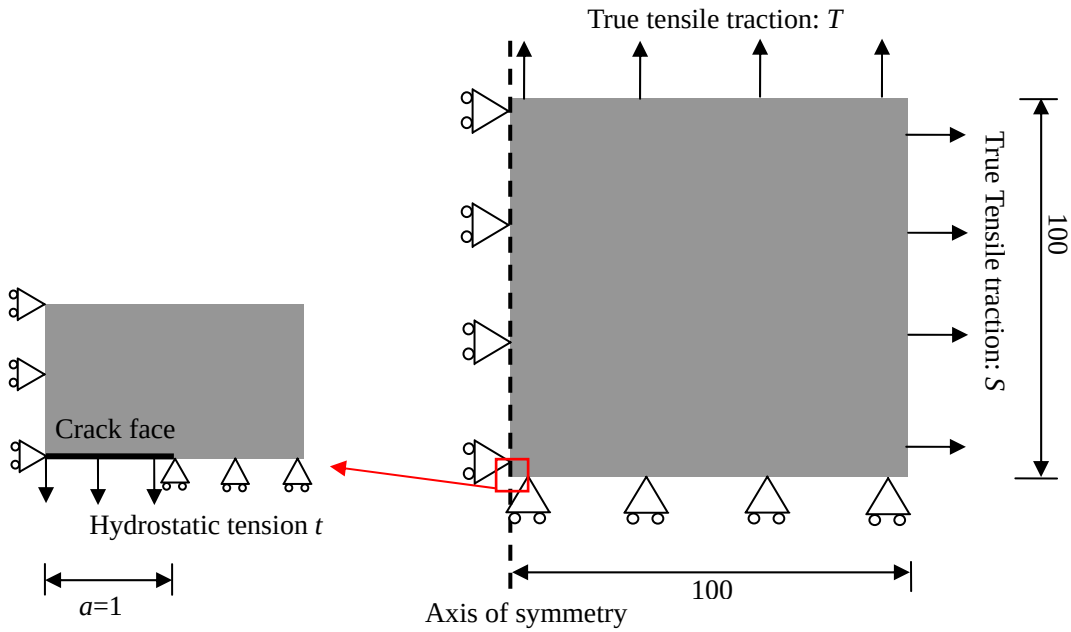

Figure 4.5 Geometry and boundary conditions of the axisymmetric FEM model. True tensile traction T and S are applied to the upper and right boundaries respectively. Symmetry boundary conditions are applied to the left and lower boundaries. The crack face is subjected to hydrostatic tension t $(0 < t < T)$ as we release the crack face tension.

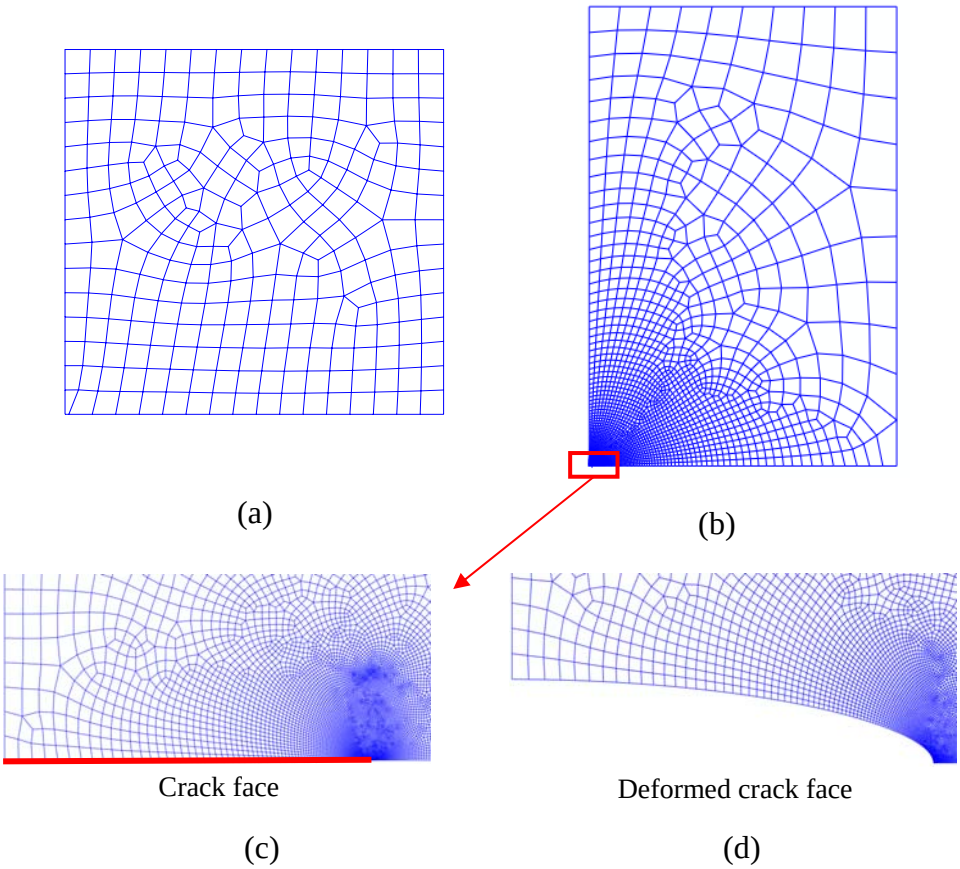

Figure 4.6 Typical meshes in the FEM calculation: (a) Coarse mesh used in the first step of the loading path (*a* in Figure 4.4); (b) Finer mesh at the beginning of releasing crack face tension (b in Figure 4.4); (c) Zoom-in view of the crack face; (d) Deformed crack face during crack face tension releasing.

4.5 Results

The normalized energy release rate $\bar{G}$ is defined by

$$\bar{G} = \frac{G}{Ea} = \frac{3}{2\pi}\int_0^{\bar{V}_0} \bar{t}\left(\bar{V}; \frac{T}{E}, \frac{S}{T}\right) d\bar{V} . \tag{4.15}$$

$\bar{G}$ is proportional to the integral in (4.15) which can be interpreted as the area underneath the $\bar{t} - \bar{V}$ curve. To illustrate the effect of the triaxiality on energy release rates in large deformation, the $\bar{t} - \bar{V}$ curves for a neo-Hookean solid for uniaxial tension ($S/T = 0$) and hydrostatic tension ($S/T = 1$) are shown in Figure 4.7. The far field tension T is equal to $0.6E$ in Figure 4.7. Recall that $\bar{t}$ is the normalized hydrostatic tension applied on the crack face and $\bar{V}$ is the normalized volume enclosed by the crack surface (see (4.8)). The hydrostatic tension tends to bring the upper and lower crack surface together and thus decreases the volume $\bar{V}$, i.e., $\bar{V}$ is a decreasing function of $\bar{t}$. The large difference in areas under the two $\bar{t} - \bar{V}$ curves shows that the energy release rate for hydrostatic tension is much larger than that for uni-axial tension. Very nonlinear behavior of $\bar{t} - \bar{V}$ curve is shown in Figure 4.7, which demonstrates that the linearity approximation employed in Yeoh's work [29] is not appropriate for an axis-symmetric crack.

Figure 4.8 plots the normalized energy release rate versus triaxialitiy $\eta = S/T$ for a neo-Hookean material. Two remote normal tensions T are considered: $T = 0.3E$ and $T = 0.01E$ which correspond to large and small deformation of the crack respectively. To highlight the effect of triaxiality, we consider the following ratio of the normalized energy release rate, defined by

$$\rho = \frac{\bar{G}\left(T/E, S/T\right)}{\bar{G}\left(T/E, S/T = 0\right)} . \tag{4.16}$$

Note that, for the case of $S/T = 0$, $\rho = 1$. Figure 4.8 shows that, for small deformation,

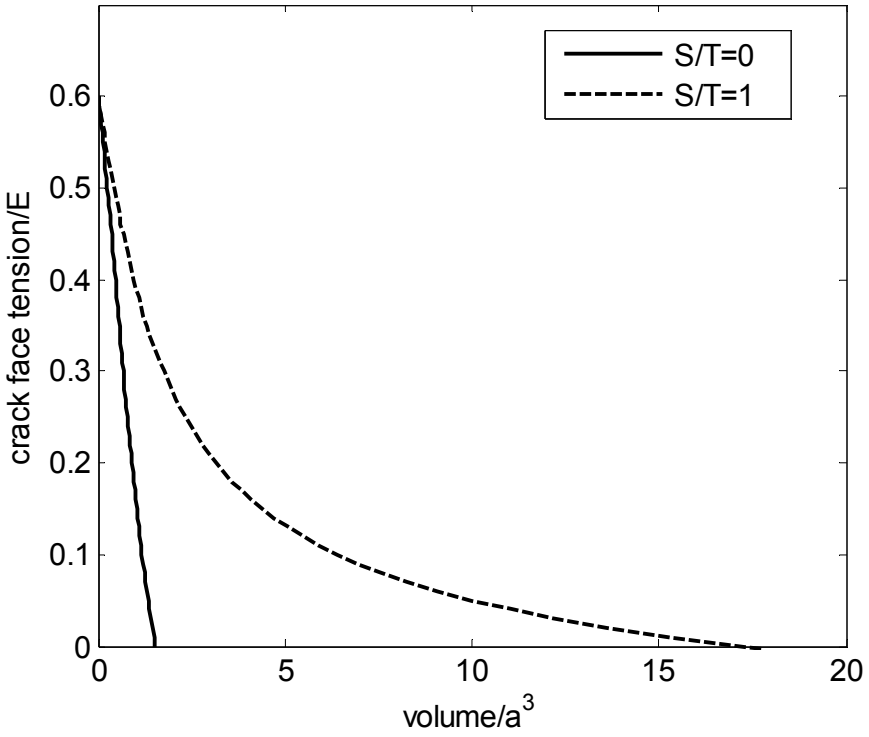

Figure 4.7 Normalized crack face tension $\bar{t}$ versus normalized deformed crack volume $\bar{V}$ when $T = 0.6E$. The solid curve is for uni-axial tension ($S/T = 0$) while the dashed one is for hydrostatic tension ($S/T = 1$).

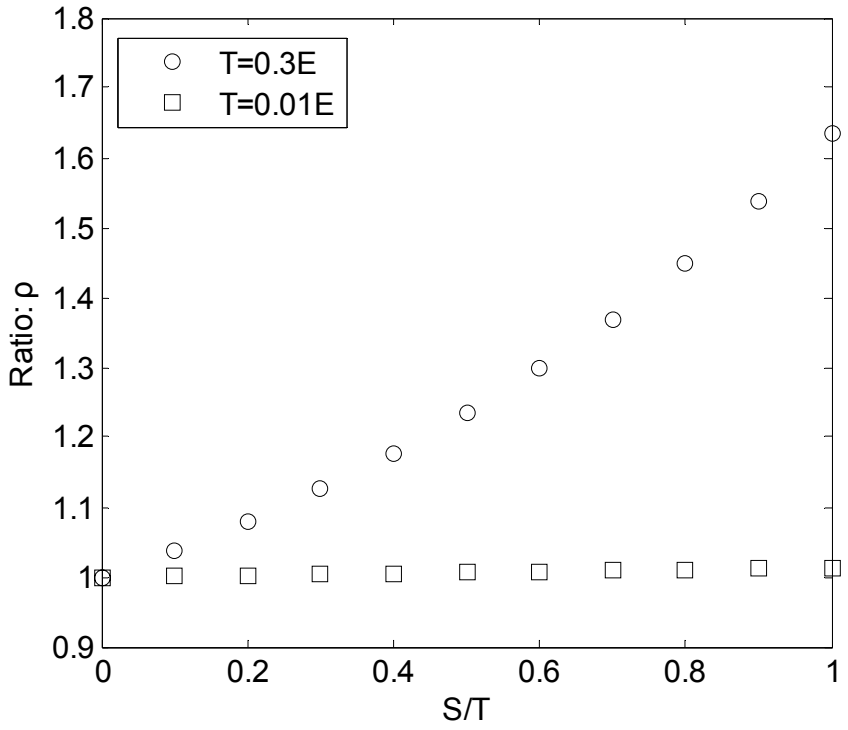

Figure 4.8 Ratio ρ defined in (3.16) versus triaxiality $\eta = S/T$ using neo-Hookean solid when $T = 0.3E$ and $T = 0.01E$.

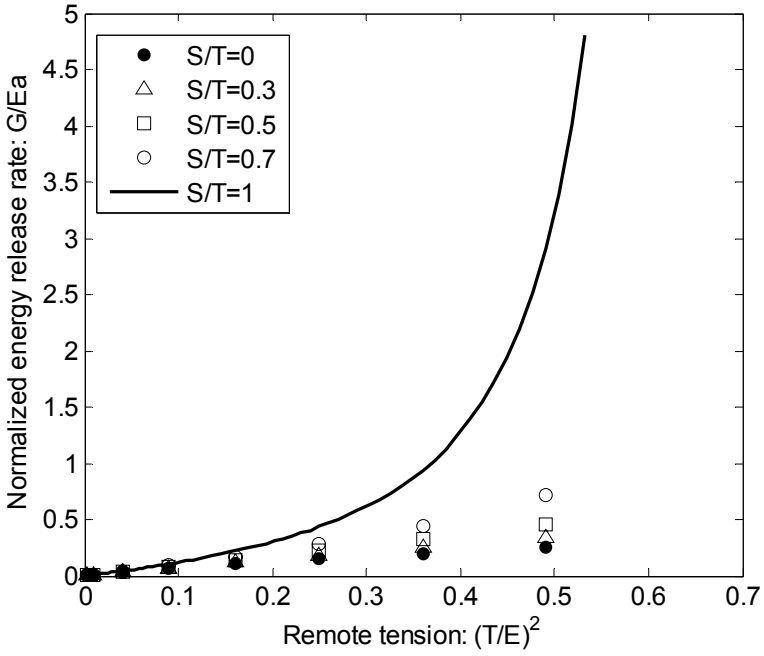

(a)

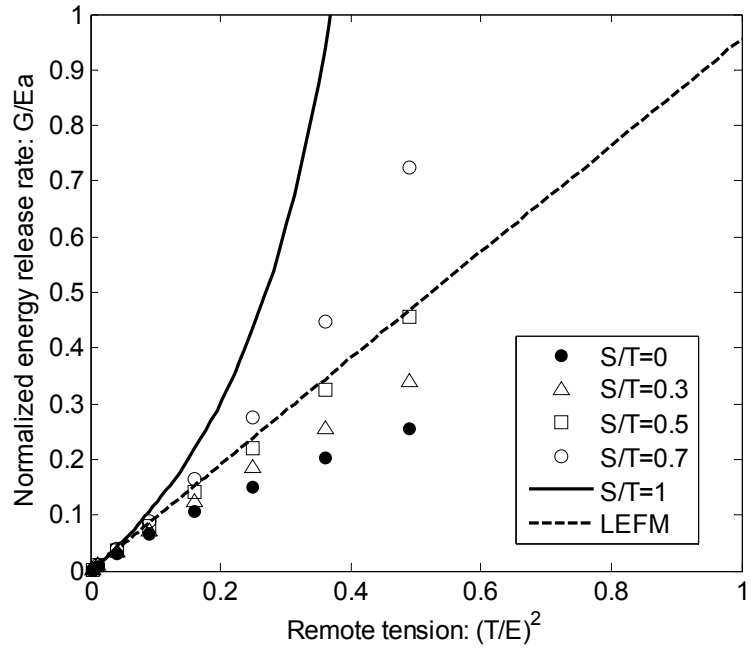

(b)

Figure 4.9 (a) Normalized energy release rate $\bar{G}$ versus $(T/E)^2$ for $S/T = 0$, 0.3, 0.5, 0.7, 1. (neo-Hookean model); (b) Closed up view of (a) for $\bar{G} < 1$. The prediction by LEFM given by (4.1) is added (dashed line).

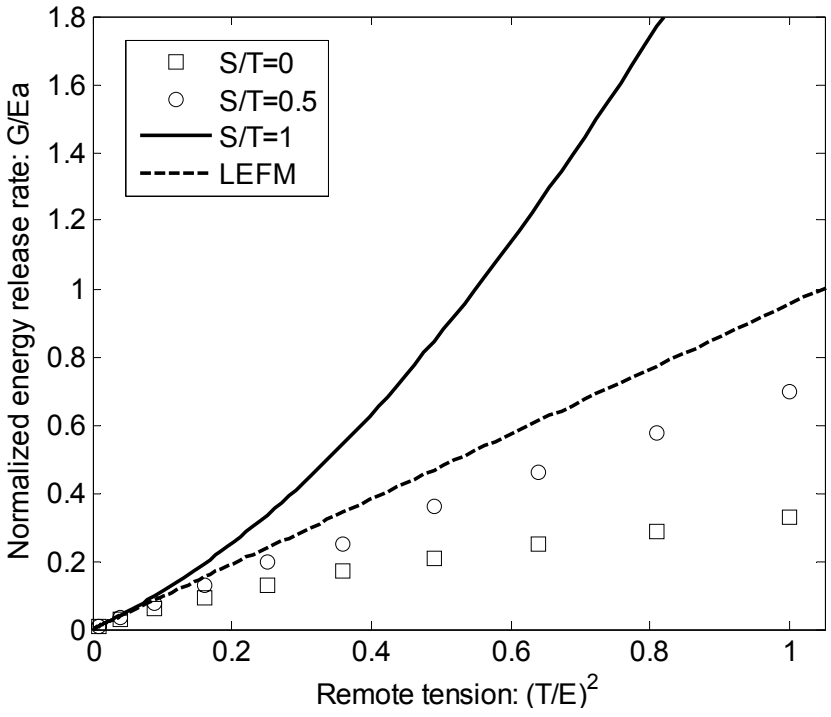

Figure 4.10 Normalized energy release rate $\bar{G}$ versus $(T/E)^2$ for an exponentially hardening model with $I^* = 5.09$. Three different triaxialities, $S/T = 0,\ 0.5,\ 1$, are used. The dashed line is the prediction by LEFM given in (4.1).

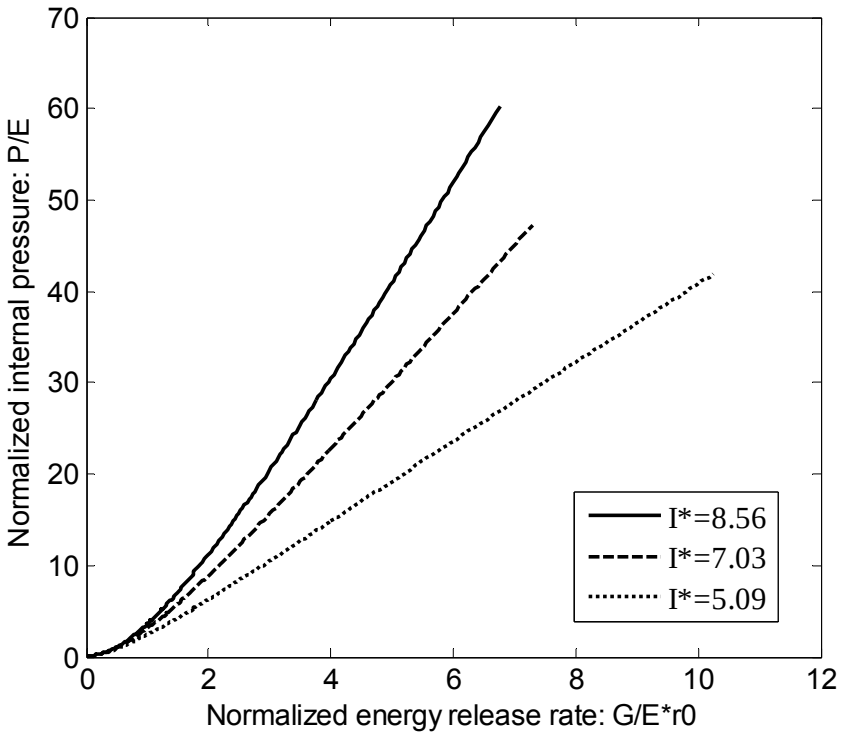

Figure 4.11 Normalized energy release rate $\bar{G}$ versus $(T/E)^2$ using exponentially hardening model with $I^* = 8.59,\ 7.03,\ 5.09$ when $S/T = 1$.

the energy release rate is approximately independent of triaxiality which is consistent with the prediction of LEFM given in (4.1). However, in the large deformation regime, the energy release rate for hydrostatic tension $(S/T=1)$ is about 60% larger than the energy release rate for uni-axial tension ($S/T=0$) for $T=0.3E$.

The dependence on the energy release rate on *T/E* for several different triaxilities for the neo-Hookean and exponentially hardening solids are shown in Figure 4.9 and Figure 4.10 respectively. The material constant I^* in the exponentially hardening model (4.13) is chosen to be 5.09. The two figures both show that energy release rate increases rapidly with triaxiality at large tension T. For $(T/E)^2 < 0.05$, the energy release rate is approximately independent of the triaxiality and agrees with the prediction of LEFM (equation (4.1)).

Figure 4.9a shows that the energy release rate starts to grow very rapidly for a neo-Hookean solid loaded under hydrostatic tension (*S/T* = 1) at $T \approx 0.7E$. This result suggests that the energy release rate for *S/T* = 1 becomes unbounded at $T \approx 0.7E$. However, the energy release rate is bounded for the exponentially hardening solid. We will further address this issue in the discussion section.

Finally, the effect of strain hardening on the energy release rate is shown in Figure 4.11. We use three different values of material constants I^* in the exponentially hardening model in (4.13), that is, $I^* = 8.56,\ 7.03,\ 5.09$. Recall that larger I^* corresponds to less strain hardening. Figure 4.11 clearly shows that strain hardening reduces the energy release rate under the same hydrostatic tension.

4.6 Summary and Discussion

The effect of triaxiality on the energy release rate of a penny-shaped crack in infinite incompressible hyper-elastic materials under different combinations of remote tensile stresses was studied. An energy balance argument allowed us to numerically calculate

the energy release rate based on the deformed crack profile using FEM. Two material models, neo-Hookean solid and an exponentially hardening solid, were used in numerical calculation. Results for both materials models support the conclusion that energy release rate is approximately independent of triaxiality when the strains are small but increases rapidly with triaxiality in large deformation. The fact that this result was found for two materials with very different strain hardening behaviors suggests that that our conclusion is applicable to a wide class of soft elastic materials.

As in Lin *et al.* [1], our numerical results suggested that the energy release rate becomes unbounded at a hydrostatic tension of $T = S \approx 0.7E$ for a neo-Hookean solid. This is not the case for exponentially hardening solids where the energy release rate is bounded for all applied loads. To gain insights into this result, we examine the solution of a spherical cavity under remote hydrostatic tension. Due to incompressibility and isotropy, the three principal stretches are

$$\lambda_\theta = \lambda_\phi = \lambda, \quad \lambda_r = \frac{1}{\lambda^2}, \tag{4.17}$$

where (r, θ, ϕ) are spherical coordinates with origin at the center of the cavity. It was shown in Dollhofer *et al.* [34] that the strain energy density can be written as a function of λ, that is, $W = w(\lambda)$ and

$$T = \int_1^{R/R_0} \frac{w'(\lambda)}{\lambda^3 - 1} d\lambda . \tag{4.18}$$

where T is remote hydrostatic tension, $w'(\lambda) \equiv dw/d\lambda$, R is the deformed cavity radius and R_0 is the initial cavity radius. If $R \to \infty$, that is, the cavity grows without bound, then (4.18) becomes

$$T = \int_1^{\infty} \frac{w'(\lambda)}{\lambda^3 - 1} d\lambda . \tag{4.19}$$

For a neo-Hookean solid,

$$T = \frac{2E}{3}\int_1^{\infty} \frac{\lambda^3 + 1}{\lambda^5} d\lambda = \frac{5E}{6} \quad , \tag{4.20}$$

which means the cavity in neo-Hookean solid will grow without bound at a finite hydrostatic tension $T = 5E/6 \approx 0.8E$. However, for an exponentially hardening solid,

$$T = \frac{2E}{3}\int_1^{\infty} \frac{\lambda^3 + 1}{\lambda^5} \exp\left(\frac{2\lambda^2 + \lambda^{-4} - 3}{I^*}\right) d\lambda . \tag{4.21}$$

The integral in (4.21) is infinite, which means that infinite remote tension is needed to deform the cavity into an infinitely large cavity. A simple analysis shows that a necessary and sufficient condition for a cavity to grow without bounded at a finite hydrostatic tension is

$$\lim_{\lambda \to \infty} \frac{w'(\lambda)}{\lambda^2} = 0 \tag{4.22}$$

Equation (4.22) implies that work functions that harden faster than or equal to λ^3 will not have instability of this type. There are similar instabilities for neo-Hookean materials. For example, a thin neo-Hookean circular membrane subjected to uniform pressure on its surface will grow unstably when the applied pressure exceeds $0.63E$ [35].

Our study shows that triaxality increases energy release rate and hence promotes crack growth. For example, the fracture toughness G_c of elastomers is on the order of $50 J/m^2$ [36]. In an exponentially hardening solid with Young's modulus of 1MPa, a crack with initial radius of $10\mu m$ loaded hydrostatically (*S/T=1)* will grow when the applied tension reaches 1.3MPa. On the other hand, for *S/T*=0.5, the maximum normalized energy release rate $\bar{G}$ reached in our calculation is about 0.7, which is much smaller than the normalized fracture toughness $\bar{G}_c = 5$ or G_c =$50 J/m^2$.

Therefore, our numerical result is unable to determine the critical tension for this case. However, a lower bound of the critical tension needed to grow the crack for this case can be determined by noting that the energy release rate for S/T=0.5 is *smaller* than the prediction of LEFM (see Figure 4.10), implying that the tension corresponding to the same energy releaser rate for S/T = 0.5 should be higher than that predicted by LEFM. Using equation (4.1), the critical tension predicted by LEFM is 2.3MPa which implies that the critical tension for S/T=0.5 is greater than 2.3MPa. This value is considerably greater than the critical tension needed to propagate the same crack loaded under hydrostatic tension. In applications, a growing crack is likely to experience a change of local triaxiality during its growth. Our analysis suggested that a crack that grows from a high triaxility region into a low triaxiality region may be arrested due to a sudden decrease in energy release rate. Of course, whether such arrest will occur or not will depend on the geometry and the applied loads. In such cases, the usage of LEFM to analyze crack growth may mislead one to attribute such crack arrest to a change of fracture mechanism, while in reality it is a purely mechanics phenomenon.

APPENDIX 4.1

DETIALS OF FINITE ELEMENT IMPLEMENTATION

The mesh in our calculation is not fixed but updated throughout the loading path. Very coarse mesh is used in the first step, i.e., from *a* to *b* in Figure 4.4, since the deformation field is uniform. The average characteristic length of element is about 5. However, when we start to release the crack face tension, we use much finer mesh especially near the crack tip. Typically, there are about 120 nodes on the crack face and the smallest element size is approximately10^{-4}. As we release the crack face tension, elements near the crack tip can suffer from severe distortion because of the singularity there. When this situation is encountered, we generate a new mesh for our FEM model; otherwise ABAQUS cannot continue the simulation. The change of mesh is carried out using a re-meshing technique introduced in Krishnan and Hui [22]. Specifically, whenever a change of mesh is necessary, the deformed geometry is extracted from the boundary of the old mesh. A new mesh is applied to the extracted geometry. The nodal values of field variables such as stresses and displacements are transferred from the old mesh to the new mesh using interpolation. We then update the loads on the new mesh and continue the calculation. The whole process of re-meshing is carried out automatically by a PYTHON script on ABAQUS. Convergence test have been carried out to check the accuracy of our results. In some cases, we refine the mesh near the crack face so that the number of nodes on the crack face is about 200 and the smallest element size is on the order of 10^{-5}. The difference in calculated energy release rate is less than 0.5% between the refined mesh and the normal mesh used in our calculation.

Calculations for the special case of $S/T=1$ can be simplified since it is equivalent to the problem where the same crack is subjected to internal hydrostatic pressure on the crack face and zero remote traction. This equivalency can be understood

by superimposing a hydrostatic stress field to the solid. Due to incompressibility of the material, superimposing a pure hydrostatic stress field has no effect on the deformation or strain energy. For the case of $S/T=1$, we do not follow the loading path shown in Figure 4.4 but increase the hydrostatic pressure on crack face step by step with zero remote loads. In this way we only need to do a single series of loading steps instead of releasing the crack face tension step by step for every hydrostatic tension *T*. In other words, once we complete the calculation for the energy release rate at $T=S=T_0$, we can immediately compute the energy release rate for remote hydrostatic tension that is smaller than T_0 using existing data. When $S/T\neq 1$, we have to carry out the loading path in Fig.4 for every set of *T* and *S*. However, we can still manipulate the loading path using superposition to save some computational work or avoid numerical instabilities in ABAQUS. For example, releasing crack face tension from $0.6E$ to 0 with $T=0.6E$ and $S=0.3E$ is equivalent to releasing crack face tension from 0.3E to -0.3E with $T=0.3E$ and $S=0$. The negative sign means hydrostatic pressure to the crack face. As we mentioned earlier, Lin and Hui [1] studied the energy release rate of a penny-shaped crack in infinite incompressible hyper-elastic materials subjected to internal pressure on the crack face. We carefully compared our results of energy release rate for neo-Hookean solid when $S/T=1$ with the existing results of Lin and Hui [1]. Perfect agreement was obtained. In fact, we were able to reproduce Figure 3 in their paper using our results.

REFERENCES

[1] Lin Y.Y., Hui C.Y., 2004, *Int. J. Fract.*, **126**, 205-221.

[2] Gent A.N., Lindley P.B., 1958, *Proc. R. Soc. London, Ser. A*, **249**, 195-205.

[3] Lakrout H., Sergot P., Creton C., 1999, *J. Adhesion*, **69**, 307-359.

[4] Creton C., Lakrout H., 2000, *J. Polym. Sci. Part B: Polym. Phys.*, **38**, 965-979.

[5] Crosby A.J., Shull K.R., Lakrout H., Creton C., 2000, *J. Appl. Phys.*, **88**, 2956-2966.

[6] Brown K.R., Creton C., 2002, *Eur. Phys. J. E.*, **9**, 35-40.

[7] Green A.E., Zerna W., 1954, *Theoretical Elasticity*, Clarendon Press, Oxford.

[8] Ball J.M., *Phil. Trans. R. Soc. A*,1982, **306**, 557-611.

[9] Abeyaratne R., Horgan C.O., 1985, *J. Elasticity*, **15**, 243-256.

[10] Horgan C.O., Abeyaratne R., 1986, *J. Elasticity*, **16**, 189-200.

[11] Abeyaratne R., Hou H.S., 1991, *J. Elasticity*, **26**, 23-42.

[12] Hou H.S., Abeyaratne R., 1992, *J. Mech. Phys. Solids*, **40**, 571-592.

[13] Chang Y.W., Gent A.N., Padovan J., 1993, *Int. J. Fract.*, **60**, 283-291.

[14] Lake G.J., Thomas A.G., 1967, *Proc. R. Soc. London, Ser. A*, **300**, 108-119.

[15] Gent A.N., Lindley P.B., Thomas A.G., 1964, *J. Appl. Polym. Sci.*, **8**, 455-466.

[16] Knowles J.K., Sternberg E., 1973, *J. Elasticity*, **3**, 67-107.

[17] Knowles J.K., Sternberg E., 1983, *J. Elasticity*, **13**, 257-293.

[18] Stephenson R.A., 1982, *J. Elasticity*, **12**, 65-99.

[19] Hermann J.M., 1989, *J. of Elasticity*, **21**, 227-269.

[20] Geubelle P.H., Knauss W.G., 1994, *J. Elasticity*, **35**, 61-98.

[21] Krishnan V.R., Hui C.Y., Long R., 2008, *Langmuir*, **24**, 14245-14253.

[22] Krishnan V.R., Hui C.Y., 2009, *Eur. Phys. J. E.*, **29**, 61-72.

[23] Cristiano A., Marcellan A., Long R., Hui C.Y., Stolk J., Creton C., 2010, *J. Polym. Sci., Part B: Polym. Phys*, **48**, 1409-1422.

[24] Tada H., Paris P.C., Irwin G.R., 2000, *The Stress Analysis of Cracks Handbook*, ASME press, New York.

[25] Rivlin R.S., Thomas A.G., 1953, *J. Polym. Sci.*, **10**, 291-318.

[26] Gent A.N., Wang C., 1991, *J. Mater. Sci.*, **26**, 3392-3395.

[27] Williams M.L., Schapery R.A., 1965, *Int. J. Fract. Mech.*, **1**, 64-71.

[28] Parks D.M., 1977, *Comput. Meth. Appl. Mech. Eng.*, **12**, 353-364.

[29] Yeoh O.H., 2002, *Mech. Mater.*, **34**, 459-474.

[30] Treloar L.R.G., 1943, *Trans. Faraday Soc.*, **39**, 241-246.

[31] Truesdell C., 1981, *A First Course in Rational Continuum Mechanics Vol.1*, (second edition), 1981, Academic Press.

[32] Seitz M.E., Marina D., Baumberger T., Krishnan V.R., Hui C.Y., Shull K.R., 2009, *Soft Matter*, **5**, 447-456.

[33] ABAQUS, Version 6.7, Dassault Systemes Simulia Corp., Providence, RI, USA.

[34] Dollhofer J., Chiche A., Muralidharan V., Creton C., Hui C.Y., 2004, *Int. J. Solids Struct.*, **41**, 6111-6127.

[35] Hassager O., Kristensen S.B., Larsen J.R., Neergaard J., 1999, J. *Non-Newtonian Fluid Mech.*, **88**, 185-204.

[36] Ahagon A., Gent A.N., 1975, *J. Polym. Sci. Part B: Polym. Phys.*, **13**, 1903-1911.

CHAPTER 5

CONCLUSIONS AND FUTURE WORK

In chapter 2, we developed an adhesive contact mechanics theory for an axisymmetric membrane in contact with a rigid substrate. In contrast to previous analyses which assumed infinitesimal deformation, this theory is based on the large deformation mechanics of hypereleastic membranes. Also, two friction conditions were considered: no-slip or frictionless. An expression of the energy release rate that only depends on the local variables at the contact edge is derived for both friction conditions. This result allows one to model adhesion as a local condition at the contact edge, thus eliminating the need to calculate the global energy change when the contact area changes. More importantly, it is not limited to the specific geometry of our system but can be extended to other systems (e.g. plane strain peel test).

Chapter 3 proposed a method to derive the crack tip stress and deformation field for a plane stress crack in incompressible hyperelastic materials. This method was demonstrated for two classes of materials, generalized neo-Hookean (GNH) materials and exponentially hardening materials. We discovered a bifurcation in the crack tip field for GNH materials at $n \approx 1.4$, where n is a material parameter characterizing the degree of strain hardening in GNH materials. This finding resolved a long standing difficulty in a previous work by Geubelle and Knauss [1]. For exponentially hardening materials, the crack tip field was shown to be divided into three angular sectors with different asymptotic behaviors.

In Chapter 4, we calculated the energy release rate for a circular crack in an infinite media of incompressible hyperelastic materials. The energy release rate calculation was based on an energy balance argument and only needed the volume enclosed by the deformed crack surface. Since no information of the crack tip stress field is required in

our method, computational efforts can be greatly reduced. We found that the energy release rate increases rapidly with triaxiality S/T, where T and S are the respective remote true tensile stresses perpendicular and parallel to the undeformed crack surface. Also, the energy release rate can be significantly reduced by increasing the degree of strain hardening.

Further efforts are needed to extend the results of this dissertation. The membrane contact theory developed in Chapter 2 is valid for any hyperelastic material model. However, numerical implementations are required to solve the boundary value problems posed in the theory, which may limit the application of our theory in interpreting experimental data. For this reason, approximate analytical solutions are preferred to describe adhesive membrane contact. For certain material models, in the limit of very large deformation, it is possible to simplify the nonlinear equations governing the membrane deformation. For example, Foster [2] derived the approximate analytical solutions of axisymmetric neo-Hookean membranes under very large deformation. We can extend our membrane contact theory along this line. In Chapter 3, the method we proposed does not apply to realistic material models with finite extensibility such as Gent's model [3] and Arruda-Boyce model [4]. Alternate method needs to be developed to study the effect of finite extensibility on the crack tip stress and deformation field.

There are still many open questions in fracture mechanisms of soft polymeric materials. For example, most soft polymeric materials have rate dependent behaviors such as viscoelasticity and swelling. Such rate dependent behavior can significantly affect the fracture toughness of soft materials. It has been shown that viscoelasticity can cause the fracture toughness of soft materials to increase several orders of magnitude when the loading rate increases [5]. However, this phenomenon remains poorly understood. Further studies needs to be carried out to answer the following questions. How does viscosity help dissipate energy and thus increase fracture toughness? On what

scale does the viscous energy dissipation occur? Another intriguing problem is the effect of interfacial friction on debonding of soft adhesives. Typically one would expect the adhesion strength of an adhesive is determined by the work of adhesion between the adhesive and the substrate. However, a counter-intuitive example has been presented in Newby Zhang *et al.* [6]. They designed two substrate surfaces: one has higher work of adhesion but lower friction; the other has lower work of adhesion but higher friction. They found that it was easier to peel adhesives from the former substrate than from the latter one. This result demonstrates the important role of friction in the strength of adhesives. In future work, this issue can be elucidated by studying the local deformation and stress field near the tip of a bimaterial interface crack.

REFERENCES

[1] Geubelle P.H., Knauss W.G., 1994, *J. Elasticity*, **35**, 61-98.

[2] Foster H.O., 1967, *Int. J. Eng. Sci.*, **5**, 95-117.

[3] Gent A.N., 1996, *Rubber Chem. Tech.*, **69**, 59-61.

[4] Arruda E.M., Boyce M.C., 1993, *J. Mech. Phys. Solids*, **41**, 389-412.

[5] Gent A.N., 1996, *Langmuir*, **12**, 4492-4496.

[6] Newby Zhang B., Chaudhury M.K., Brown H.R., 1995, *Science*, **269**, 1407-1409.